

**Faculty of Science and Engineering
WASM: Minerals, Energy and Chemical Engineering**

**Application of 3D Discrete Element Method in Geomechanics, with
A Focus on Rock Scratch Testing**

Bahman Joodi

This thesis is presented for the Degree of

Doctor of Philosophy

of

Curtin University

December 2018

Declaration

To the best of my knowledge and belief, this thesis contains no material previously published by any other person except where due acknowledgment has been made.

This thesis contains no material, which has been accepted for the award of any other degree or diploma in any university.

Name:

Bahman Joodi

Signature:

Date:

7/12/2018

Abstract

The increasing demand for optimisation in resource and civil projects requires efficient modelling techniques to understand and replicate the processes. While laboratory experiments are often considered as the preferred method of testing, computer simulation can provide a more accessible and less expensive alternative. Continuum-based numerical approaches, while providing a fast and efficient solution, have limitations in modelling the grain-based material, such as sand and rocks. This is an area where discrete methods can be used as an ideal tool. A survey of the available literature, however, proved that there have been limited examples of practical applications, while the number of publications is increasing near-exponentially.

This research was initiated to identify the capabilities of Three-Dimensional Discrete Element Method (3D DEM) in geomechanical applications. I could not find any examples in the literature where all the sensitivities and the recommended practices for building such a model were followed properly. This motivated dedicating a large body of the research to rock property calibration, where I have developed new methods for sample calibration and testing. A systematic approach is proposed to build numerical samples from microscopic and macroscopic data. Comprehensive sensitivity analyses are carried out to cover the whole uncertainty range.

An extensive modelling effort was conducted to simulate Rock Scratch Testing (RST) on the calibrated samples. A complete set of Validation Criteria is established and used to confirm the numerical results. It is shown that only one generation of the samples – with the most accurate calibration – meets all the validation criteria. The research outcome questioned the conclusions of most of the available literature and deduced that the DEM modelling of RST can only be conditionally validated at a specific cutting speed. A practical approach is developed to use RST as a predictive tool to replace the time and resource-demanding UCS simulation.

To further expand the discussions, 3D DEM was used to simulate failure of a thick-walled cylinder, and erosion of a loose sandstone. In both cases, good agreements were obtained between the numerical and experimental results. A novel approach is proposed for erosion modelling, where both the rock and fluid phases are simulated using discrete particles. To the best of my knowledge, this is the first time fluid modelling has been developed by DEM for geomechanical applications. A thorough fluid calibration process has been developed and sensitivities were tested - to find the critical parameters' range.

DEM limitations are discussed throughout the thesis and where applicable, solutions are suggested to overcome the restrictions and increase the practicalities of application.

Acknowledgements

I would like to take this opportunity to express my gratitude to each and every person who inspired, encouraged or supported me throughout completion of this dissertation.

I am fortunate to be guided by three supervisors during the course of this research. I sincerely appreciate Dr Jorge Sampaio for his inspirations, which motivated me to start this journey. I am deeply indebted to Professor Vamegh Rasouli for his contributions and unconditional supports. I would also like to convey my sincere gratitude to Professor Brian Evans for his continuous supports and guidance. Without him, I would not be able to complete this study.

I thank Dr. Paul Choate for the constructive discussions and new ideas he provided in numerical modelling. Special thanks to Dr. Mohammad Sarmadivaleh and Dr. Gary Cavanough for the technical supports, peer reviews and advises throughout the completion of this research.

I wish to thank Mr Massoud Bayati and Mr Soroush Tehrani for the research cooperation, which enabled me to expand my modelling efforts.

To my wife, Ainaz, whose patience and continuous supports made it possible for me to complete this work.

Table of Contents

1	Introduction.....	1
2	Introduction to Discrete Element Method.....	5
3	Literature Review.....	24
3.1)	Application of DEM in Geomechanics.....	24
3.2)	Material Genesis Procedure.....	26
3.2.1	Sample Calibration.....	27
3.3)	Chapter Conclusions.....	44
4	Sample Preparation.....	46
4.1)	Introduction.....	46
4.2)	Laboratory samples.....	46
4.2.1	Natural Bentheimer Samples.....	47
4.2.1	Synthetic Samples.....	52
4.3)	Numerical samples.....	54
4.3.1	Test Procedure.....	54
4.3.2	Early Samples.....	57
4.3.3	Calibration Procedure.....	58
4.4)	Chapter Conclusions.....	68
5	Rock Scratch Testing.....	70
5.1)	Model Set-up.....	70
5.2)	Visual Investigations and Validation Criteria.....	72
5.3)	Exploratory 2D Simulation.....	74
5.4)	3D Simulations.....	76
5.5)	Application of RST in numerical modelling.....	90
5.5.1	UCS Estimation from RST Results.....	91
5.5.2	Young's Modulus.....	93
5.5.3	Poisson's Ratio.....	95
5.6)	Chapter Conclusions.....	99
6	Other Example Applications.....	100

6.1)	Thick-Walled Cylinder Test.....	100
6.1.1	Introduction.....	100
6.1.2	Experimental Set-up.....	101
6.1.3	Numerical Set-up and Results.....	102
6.1.4	Comparison with Experimental and Analytical Methods	106
6.2)	Erosion	106
6.2.1	Introduction.....	106
6.2.2	Experimental set up.....	107
6.2.3	Numerical Modelling	108
6.3)	Chapter Conclusions	116
7	Conclusion and Recommendations.....	117
7.1)	Research Outcomes and Findings	117
7.2)	Recommendations.....	120
	References.....	122
	Appendix-1	128
	Permissions and Co-author Attribution Statements.....	131

List of Figures

Figure 2-1 “Hard Sphere” and “Soft Sphere” approaches to DEM	8
Figure 2-2 Analogy between the physical and numerical samples	10
Figure 2-3 Sequence of calculations in a DEM simulation.....	11
Figure 2-4 Domain, parent and child cells.....	14
Figure 2-5 One dimensional mass spring system.....	15
Figure 2-6 (a) Multiple mass-spring system. (b and c) equivalent systems for the centre mass.....	16
Figure 2-7 Example clump shapes	17
Figure 2-8 Linear bond components	18
Figure 2-9 Left: PBM components; Right: PBM failure envelope	19
Figure 2-10 Analogy between marble grains and a 2D flat-joint model. A partly failed flat-joint contact between two particles.....	20
Figure 2-11 FJM resistance to rotation after contact failure	20
Figure 2-12 FJM components (left) and FJM failure envelope (right)	21
Figure 2-13 Time required to perform 1000 cycles on a sample with 79,000 balls.....	23
Figure 3-1 Number of DEM related papers	24
Figure 3-2 (a) Number of DEM related papers in geomechanics; (b) Number of particles used in DEM simulations	25
Figure 3-3 Material genesis procedure: (a) generated cloud, (b) rearranged particles and (c) final state of particles after scaling	27
Figure 3-4 The calibration methods proposed by Itasca (top) and Wu and Xu (2016) (bottom).....	30
Figure 3-5 Compressive and tensile strength measurements for different rock types versus parallel-bond model	31
Figure 3-6 Explicit porosity matching process	32
Figure 3-7 Using the outer-most particles to apply the confining force instead of rigid walls.....	34
Figure 3-8 Left: The stress distribution and cutting forces for orthogonal rock cutting; Right: The circular plate-type dynamometer	35
Figure 3-9 Ductile (Left) versus brittle (Right) mode of cutting. The corresponding cutting forces are shown below each diagram.	36
Figure 3-10 Tangential force of a sharp cutter versus depth of cut.....	37
Figure 3-11 Cross-plot of ISE vs UCS for 376 rock samples	37
Figure 3-12 Plot of size effect law	39
Figure 3-13 Rojek et al.'s simulation set up and results.....	40
Figure 3-14 Numerical simulations of Su and Akcin (2010).....	40
Figure 3-15 Simulation results of Tan et al. (2008).....	41
Figure 3-16 Simulation results of Tan et al. (2008).....	42

Figure 3-17 RST simulation results of Rizo (2013).....	43
Figure 4-1 Microscopic pictures of Bentheimer sandstone grains. Left: original optical image. Right: binary segmented image.	47
Figure 4-2 (a) 2D slices through the rock and pore space. Sandstone is light grey. (b) and (c): SEM images.	48
Figure 4-3 Grain size distribution of Bentheimer sandstone.	48
Figure 4-4 UCS test set-up. (a) Intact sample with sensors and (b) Failed sample	49
Figure 4-5 Unconfined Compression Test of Bentheimer Sandstone.....	49
Figure 4-6 Brazilian Test Set up and results.	50
Figure 4-7 Multistage Confined Compression Test of Bentheimer Sandstone.....	51
Figure 4-8 Mohr-Coulomb failure criterion generated from UCS and multi-stage test results.	51
Figure 4-9 Particle Size Distribution (PSD) of the numerical synthetic model.....	53
Figure 4-10 UCS test simulation set up.	55
Figure 4-11 Strain measurement methods: Left: Measurement Sphere; Right: Sensor Balls.....	56
Figure 4-12 Direct tension test set-up.	56
Figure 4-13 Generating an outer layer for applying confined stress. Left: Confined test set-up; Right: Cross-section of the model showing the outer layer.	57
Figure 4-14 Top: Int3DClump; Bottom: Int3DBall.....	58
Figure 4-15 Different sample resolutions as a result of different Coarsening Factors.	60
Figure 4-16 Effect of FJM element number on stress-strain curve.....	62
Figure 4-17 Proposed calibration process.....	64
Figure 4-18 Stress-strain curves obtained from experiments versus the simulation results.	64
Figure 4-19 Size sensitivity on FNL samples (Damping Factor 0.7).	65
Figure 4-20 Model scale effect on macro-properties.	66
Figure 4-21 Damping effect on stress-strain curves. Solid lines: Damping Factor of 0.7; Dashed lines: Damping factor of 0.4.....	68
Figure 5-1 Left: Sample size used for UCS and confined tests; Right: Sample size used for RST tests	71
Figure 5-2 Using coarser particles around the cutting area.....	71
Figure 5-3 RST simulation set-up showing a deep cutting	72
Figure 5-4 Graphical representation of deep cutting results in 3D simulations. Left: Full 3D; Right: Cross-section through 3D model.....	73
Figure 5-5 Results of the 2D UCS test simulation.....	74
Figure 5-6 PFC2D cutting simulations. Left: Relatively shallow depth of cut (1mm); Right: Deep depth of cut (4mm)	75
Figure 5-7 PFC2D cutting response for Berea Sandstone	75

Figure 5-8 Average ISE obtained from different cutter speeds. BR angle:15°, DoC:0.44-4mm, Cutter Width:8 mm.	78
Figure 5-9 Colour coding of the cutting results based on the limiting criteria. Sample UCS is 34.2 MPa. Note the Scale of graphs	79
Figure 5-10 Dispersion of UCS data as a result of different random seed in sample generation	80
Figure 5-11 RST simulation results for sample FNL3D-A.....	82
Figure 5-12 RST simulation results for different coarsening factors of Sample FNL3D-A.....	83
Figure 5-13 Normalised RST simulation results for different coarsening factors of Sample FNL3D-A	84
Figure 5-14 Effect of FJM contact geometrical settings on RST response.....	85
Figure 5-15 Effect of damping ratio on RST response	85
Figure 5-16 Effect of cutting velocity on RST response.....	86
Figure 5-17 Effect of pre-existing cracks on RST response	87
Figure 5-18 Cutting Velocity effect on FNL3D-B sample	87
Figure 5-19 Effect of pre-existing cracks and non-uniform bond strength (FNL3D-C) on RST response	88
Figure 5-20 Cutting Velocity effect on FNL3D-C sample	88
Figure 5-21 Cutting response of FNL3D-D.....	89
Figure 5-22 Cutting Velocity effect on FNL3D-D sample	90
Figure 5-23 Cutting response on FNL3D-D at cutter speed of 5m/s	90
Figure 5-24 Cutting response on FNL3D-D sample with different CF	91
Figure 5-25 Normalised cutting response on FNL3D-D sample with different CF.....	92
Figure 5-26 Example rock cutting response for a Bentheimer sample. Cutting speed: 5m/hr, DoC:2mm and BR=15°	93
Figure 5-27 Filtered FNL3D-D cutting response.....	94
Figure 5-28 Strain calculation method.....	94
Figure 5-29 Histogram of the Young's Modulus obtained from Bentheimer cutting data	95
Figure 5-30 Gauge grain set up for strain measurement	96
Figure 5-31 Lateral displacement along sample's length	97
Figure 5-32 Different configurations of Gauge Grains for strain calculation.....	98
Figure 6-1 Left: Sample and sleeve arrangement. Right: TWC experiment set-up.....	102
Figure 6-2 TWC test results versus different analytical models	102
Figure 6-3 Sieve Analysis versus Numerical Sample PSD.....	103
Figure 6-4 Left: Generated membrane around the sample. Red layer exerts the axial stress while the green layer applies the radial stress; Right: a cut-through view of the sample.....	104
Figure 6-5 Measurement spheres	104
Figure 6-6 Camera view inside the internal hole, which was used for detecting the sample failure ..	105

Figure 6-7 Numerical simulation results of TWC test versus experimental observations 106

Figure 6-8 Erosion modelling experimental setup 107

Figure 6-9 Example output during an erosion experiment..... 108

Figure 6-10 Level of particle exposure to fluid flow 110

Figure 6-11 Model set-up for drag measurement in a flat plane..... 111

Figure 6-12 Model setup for measuring the drag on a spherical object. Fluid particles are filtered to make the measurement sphere visible..... 112

Figure 6-13 A typical response from the discrete fluid particles' flow over the spherical object. Green particles are freshly generated in the Ball Assembly Area. Blue particles were generated in previous batches. The green curve shows the recorded force..... 113

Figure 6-14 Model set up for simulation of erosion in a borehole..... 114

Figure 6-15 Left: Intact rock sample; Right: Eroded rock sample. Blue grains were detached from the sample as a result of the fluid particle interaction..... 115

Figure 6-16 An extreme case, where the mass and velocity of the fluid particles were set too high. Left: model at initial state. Right: Rock grains eroded. Notice the eroded and lifted grains inside the fluid particles..... 116

List of Tables

Table 2-1 Itasca's recommended settings for local damping	22
Table 3-1 Specifications of the PC used for the numerical simulations	25
Table 4-1 Results of uni-axial compression test	50
Table 4-2 mechanical properties of the Bentheimer sandstone	52
Table 4-3 Properties of the synthetic sandstone used in TWC tests	53
Table 4-4 Summary of the numerical samples used for RST simulation.....	54
Table 4-5 Coarsening Factor versus the number of particles required for building a standard 1.5" core sample.....	60
Table 4-6 Model scale effect on macro properties.....	65
Table 4-7 Properties of FNL3D-A-1	66
Table 5-1 Mechanical Properties of Berea Sandstone and those obtained from the exploratory PFC2D simulations	74
Table 5-2 Properties of the three INT3D rock samples	77
Table 5-3 Cutting results of Sample B-1	79
Table 5-4 Simulation time required for RST simulation of FNL3D-D, CF=4.	92
Table 6-1 Properties of synthetic rock samples used for TWC tests	101
Table 6-2 Micro properties of the simple model for exploratory TWC modelling.....	103
Table 6-3 Erosion experiment parameters	108
Table 6-4 Numerical rock sample properties	109
Table 6-5 Numerical results for erosion modelling	115

Nomenclature

a	<i>Acceleration</i>
BEM	<i>Boundary Element Method</i>
C	<i>Cohesion</i>
D	<i>Depth</i>
DDA	<i>Discontinuous Deformation Analysis</i>
DEM	<i>Distinct Element Method</i>
DFN	<i>Discrete Fracture Network Method</i>
d_o	<i>Critical Transitional Depth of Cut</i>
DoC	<i>Depth of Cut</i>
E	<i>Young's Modulus</i>
E^*	<i>Effective Elasticity Modulus</i>
E_c	<i>Elasticity Modulus of the Particles</i>
\bar{E}_c	<i>Elasticity Modulus of the Parallel Bonds</i>
E_r	<i>Error</i>
f	<i>Force</i>
FDM	<i>Finite Difference Method</i>
FEM	<i>Finite Element Method</i>
FJM	<i>Flat Joint Model</i>
F_n	<i>Normal Force</i>
F_s	<i>Shear Force</i>
GPa	10^9 Pascals
H	<i>Height</i>
I	<i>Moment of Inertia</i>
ID	<i>Inner Diameter</i>
ISE	<i>Intrinsic Specific Energy</i>
KIC	<i>Fracture Toughness</i>
K_n	<i>Normal Stiffness</i>
K_s	<i>Shear Stiffness</i>
k_{rot}	<i>Rotational Stiffness</i>
k_{tran}	<i>Transitional Stiffness</i>
M	<i>Mass</i>
MPa	10^6 Pascals
N_a	<i>Number of Elements in Circumferential Direction</i>
N_r	<i>Number of Elements in Radial Direction</i>
OD	<i>Outer Diameter</i>

<i>PBM</i>	<i>Parallel-Bond Model</i>
<i>PFC2D</i>	<i>Particle Flow Code in Two Dimensions</i>
<i>PFC3D</i>	<i>Particle Flow Code in Three Dimensions</i>
<i>PSD</i>	<i>Particle Size Distribution</i>
<i>q</i>	<i>Fluid Flow Rate</i>
<i>R</i>	<i>Radius</i>
<i>RST</i>	<i>Rock Scratch Test</i>
<i>T</i>	<i>Tensile Strength</i>
\bar{T}	<i>Period Of Free Oscillation</i>
<i>TWC</i>	<i>Thick-Walled Cylinder</i>
<i>UCS</i>	<i>Unconfined Compressive Strength</i>
<i>v₀</i>	<i>Initial Velocity</i>
<i>W</i>	<i>Width</i>
Δt	<i>Time-step</i>
ζ	<i>Normal to Horizontal Cutting Force Ratio</i>
κ^*	<i>Normal-To-Shear Stiffness Ratio</i>
λ	<i>Radius Multiplier</i>
μ	<i>Friction Coefficient</i>
ν	<i>Poisson's Ratio</i>
ρ_b	<i>Bulk Density</i>
φ	<i>Internal Friction Angle</i>

Publications of this thesis

1. Joodi, B., M. Sarmadivaleh, V. Rasouli & A. Nabipour. 2012. "Simulation Of The Cutting Action Of A Single PDC Cutter Using DEM". *WIT Transactions on Engineering Sciences* 81:143-150.
2. Joodi, B. 2016. "Using Scratch Tests for Rock Strength Determination in Discrete Element Method." Paper presented at *50th U.S. Rock Mechanics/Geomechanics Symposium*, Houston, USA, 26-29 June 2016.
3. Tehrani, S., Joodi, B., Nourifard, N., Sarmadivaleh, M. and Younessi, A. 2017. "Experimental and numerical investigation of the effect of inner and outer boundary dimensions on collapse of the sample in thick-walled cylinder test." Paper presented at *51st U.S. Rock Mechanics/Geomechanics Symposium*, San Francisco, USA 25-28 June 2017.

1 Introduction

The ever-increasing need for optimisation of oil and gas, mining, and civil developments necessitates the ability to model the soil and rock masses under stress. The optimisation often relies on laboratory tests or computer simulations. Due to the complex structure and behaviour of rocks, normally the simulations are performed under simplified or controlled conditions to isolate the critical parameters.

Each of the simulation methods has its own advantages and limitations: Laboratory tests are often considered to be more realistic, because they involve physical simulation of the real-life system. On the other hand, the required simplifications, equipment limitations and failures, lack of access to the representative soil/rock samples and difficulties in monitoring extremely small or large features may limit the usefulness of laboratory tests. Computer modelling, however, is a virtual simulation of the real-life systems, which are governed by constitutive models that approximate the stress-strain relationships. Computer models are often less expensive and if properly set-up, will enable researchers to perform in-depth analysis of the system at the micro-, as well as macro-scale.

This research was initially dedicated to laboratory simulation of the rock-bit interaction under far-field conditions. A one-of-a-kind laboratory-scale drilling rig was designed and built. The early results proved the equipment was capable of being used as a simulation tool to study the cutting action of full faced bits. Regretfully, as a result of several manufacturing issues and safety concerns, the operation of the equipment was halted. Due to the interest gained during the laboratory tests, it was decided to continue in the same research area, however using computer modelling to study the rock-bit interaction.

One of the critical issues observed in reviewing the available literature for comparing the performance of different numerical methods, was the tendency of most of the authors to focus on the advantages of their preferred, or used, numerical method. This was done without clearly stating the limitations they faced during their studies, and was more pronounced in the case of recent simulations using the Discrete Element Method (DEM). While there were numerous references encountered in the literature regarding the application of this method in geomechanics, it was noted that its practical use has been limited, although rapidly expanding. The main reasons for this lack of popularity are the difficulties in setting up the model and huge computational power requirements to run the DEM models.

Because of the initial research topic, special attention was given to the DEM simulation of Rock Scratch Testing (RST). However, to the best of knowledge of the author, no comprehensive study was available

in the literature. The existing studies were either dedicated to addressing a specific problem in generating the numerical samples or investigating specific issues in rock scratch testing. Only few studies were identified as suitable for the purpose of the current research, which will be referred to throughout this study (Rizo, 2013; Huang et al., 2012). Regrettably despite the high quality of those studies, there were numerous limitations on the methods, parameters investigated, or sample scale. Of the existing literature, some only considered two dimensional problems, while others conveniently used high damping ratios and cutter speeds to simulate the cutting process and validate the results. In most of the reviewed papers, the authors have used very coarse models without investigating the scale effect and particle size distribution, or calibrated their models poorly. In many others, only a simple contact model (e.g. parallel-bond contact model) was used, while the authors have admitted its limitations, especially the unrealistic compressional to tensile strength ratio. Due to these reasons, it was decided to dedicate the focus of the current study to DEM simulation of rock scratch testing, in three dimensions.

In the current research, the state-of-the-art methods, summarised from literature, were used to calibrate the numerical rock sample properties to those measured in the laboratory. Where necessary, modifications were made to improve the efficiency of the methods, as exemplified by the proposed calibration process (Chapter 4). In addition to the basic rock mechanical properties (uniaxial compressional strength, Young's Modulus and Poisson's ratio), the failure envelope was calibrated to match the cohesion and internal friction angle of the tested rocks. Instead of assuming a particle size ratio, which was the case in all the RST modelling publications reviewed, the actual particle size distribution was used in the sample generation process. Also, considerable efforts were made on studying the particle size effect. The final simulations were performed on rock samples with real-life grain sizes. This required using millions of particles in the models which took days or weeks to run. The obtained results were useful in addressing the scale effect that was overlooked in many other publications. The confined tests were performed using a new approach by building a "flexible" membrane around the sample, instead of the commonly used rigid walls. Extreme values of damping ratio and cutter speeds were investigated as the sensitivity cases for rock scratch testing. These are two important parameters that severely affect the cutter response, which were also overlooked in the available literature.

In addition to RST modelling, two other simulations are also presented in Chapter 6 to further demonstrate the potential of discrete element method in geomechanical applications. These are Thick-Walled Cylinder (TWC) tests and erosion modelling in loose sandstones. The laboratory tests of these applications were PhD programs in progress at the Petroleum Engineering Department. The numerical modelling of these applications was performed by direct feedback from other researchers and the shared data was used in validation of the numerical results. The erosion problem is particularly unique because all of the system elements, including the fluid, were modelled using discrete particles.

The three examples cover a wide range of applications: In the case of TWC, the loading rate is very low and the only movement is the constant strain rate imposed on the sample. The cutter movement speed in the RST application is much higher than the TWC loading rate and it can be considered a dynamically intermediate case. In the erosion modelling, the fluid is represented as discrete particles moving in random directions, with a given dominant flow direction. This can be considered as the highly dynamic case. While the erosion and TWC applications are only included for further demonstration of DEM capability and are at early stages of development, the three cases show the method is extremely powerful in capturing the unique features of each application. Limitations of the DEM modelling are also explained in different parts of the thesis. Throughout my simulations, practical solutions are given to reduce the run time.

Research Objectives

The objectives of this research are:

1. To review and summarize the available literature related to micro-mechanical calibration of DEM
2. To propose a calibration method to efficiently calibrate the properties of the numerical rock sample to those of the physical sample
3. To conduct a comprehensive sensitivity study on
 - Scale
 - Contact properties
 - Damping ratio
4. To simulate and validate several applications and identify the advantages and limitations of DEM from a geomechanical point of view
5. To reduce the computational time and increase the practicality of the method

Dissertation Layout

This dissertation is organized in seven chapters as follows:

Chapter 1 presents the research overview and objectives.

Chapter 2 presents a summary of the key features of DEM. The intention of including this chapter was to familiarise the reader with the concept of the DEM modelling and the key terms used in this work. Only high-level summaries are presented under each heading and the details are only discussed for the material, which will be used later in the thesis.

Chapter 3 surveys the literature on the advancements of DEM sample generation, calibration methods and rock scratch testing. It also presents a summary of experiments which will be used in the following chapters for the validation of the simulation results.

Chapter 4 summarizes the samples used in this research. Due to the high number of samples, and for clarification purposes, the details of the synthetic, natural and numerical rock samples are explained. The procedure for preparing the synthetic rock sample, and the experimental tests performed to measure the mechanical properties, are explained. The advancements and recommendations of Chapter 3 were applied in preparing the numerical samples. This step is extremely important, because the simulation work of the next chapters will be based on the experimental results and the numerical sample calibration set out in this chapter.

Chapter 5 is dedicated to simulation of rock scratch testing, where samples generated in Chapter 4 will be used to perform the modelling and sensitivities.

Chapter 6 outlines the DEM modelling of additional two geomechanical applications.

Chapter 7 contains the conclusions of the current research and recommendations for future work.

2 Introduction to Discrete Element Method

Scientists, whether an engineer, economist or social science expert, use mathematical modelling to understand and predict system behaviours. The models can be designed for optimizing an orbiting satellite, predicting the effect of a financial decision on GDP growth, or simulating traffic to improve roads. Mathematics is the quantification tool, as the Britannica Encyclopaedia (Folkerts et al. 2018), defines it:

“... the science of structure, order, and relation, ... It deals with logical reasoning and quantitative calculation, and its development has involved an increasing degree of idealization and abstraction of its subject matter. ... mathematics has been an indispensable adjunct to the physical sciences and technology, and in more recent times it has assumed a similar role in the quantitative aspects of the life sciences.”

Geomechanics, as the science of rocks and soil, is also very much dependant on mathematical representation and modelling. Rock and soil bodies are complicated systems of grains, cement, fractures and faults. Each of these components is also subject to variation horizontally along each formation, and vertically, as overburden and pore pressures changes. Due to the highly complex nature of natural soil and rock bodies, modelling often involves simplifications. In their paper, Starfield and Cundall (1988) explain this simplification:

“...we build models because the real world is too complex for our understanding; it does not help if we build models that are also too complex. The art of modeling lies in determining what aspects of the geology are essential for the model. The challenge is to turn that art into a methodology.”

No matter what mathematical method was used for rock or soil modelling, in all of the literature available to date, there has been some degree of simplification. This will be discussed in more detail in the following sections. The suitability of each modelling method is mainly dependant on its underlying assumptions and size scale. As a general rule, a model which is more detailed, will require more powerful computational facilities and will take longer to simulate over a given time period. The detailed models can be used for small lab-scale samples. It is not practical (or even possible) to use a fine model for simulation of a large rock body, even with the most powerful super computers available today.

There have been a large number of publications by numerous researchers on modelling different geomechanical applications. Many mathematical approaches have been tried for this purpose. The methods can be broadly divided into the following categories:

1. Continuum methods
2. Discrete methods
3. Hybrid methods

Each of the above has its own advantages and failures. Continuum methods assume the rock body is made of a uniform material, similar to metals. The finite difference method (FDM), the finite element method (FEM) and the boundary element method (BEM) are classified in this category. These methods are applicable, only if there are a limited number of fractures in the system and the rock mass is not significantly affected by fracture openings and complete block detachments (Jing and Hudson, 2002). Of the other main failures of continuum methods, one can mention their limited capabilities in simulating large deformation cases, which are often encountered in geomechanics. This restriction arises because the continuum models are mesh-based and the large deformations cause distortion of the meshes (Manne and Satyam, 2015). Some authors have addressed this issue by removing the damaged finite elements upon reaching certain failure criteria (Rojek, 2011). However, regardless of the approach, the existing continuum methods have the natural difficulty in characterizing the micro-scale behaviour of rocks (Ding, 2013).

In the discrete methods, the rock is simulated as a system of interconnected discrete particles. This category includes the distinct element method (DEM), discrete fracture network (DFN) method and Discontinuous Deformation Analysis (DDA). The discrete methods are best suitable for situations where the rocks are moderately fractured and the continuum-based models cannot suitably handle the physics because either the fracture number is too large or large-scale displacements of individual blocks are possible (Jing and Hudson, 2002).

One of the main differences between the continuum-based methods and DEM is that in the former the contact patterns between the components are fixed, while DEM allows for continuous change of contact patterns during the deformation process (Jing and Hudson, 2002). It must be emphasized that DEM fundamentally differs from the advanced continuum methods, such as mesh-less or mesh-free approaches which are developed to address shortfalls of the continuum methods. While DEM explicitly models the particles as independent entities, in the mesh-less methods, such as the Smoothed Particles Hydrodynamics (SPH), the particles are interpolation points, rather than physical particles. This makes SPH particles similar to the nodes of a finite element method (O'Sullivan, 2011).

Hybrid continuum/discrete methods use a formulation that is a combination of both of the previous categories, to use the advantages of each of its components, more importantly the simulation speed of continuum models and the capability of handling large deformations in DEM models.

There have been different views on the suitability of the methods, which are mainly dependant on the authors' investigated problems. Rojek et al. (2011), for example, reviewed the methods used for rock scratch modelling and concluded DEM is a better tool compared to continuum methods. Helmons et al. (2016) argued DEM is better suited for rock scratch testing, due to its discrete nature, which allows for crack initiation and propagation. In a general note, Jing and Hudson (2002) argued that none of the methods are absolutely superior over the others, however using the hybrid methods one can avoid some of the disadvantages of the continuum or discrete methods.

As will be discussed in Chapters 4 to 7, the nature of problems investigated in the current research, similar to many other applications in geomechanics, are such that

1. The investigated rock sample is relatively small. The lab experiments mainly are conducted on a standard core size.
2. The problem involves large-scale displacements, as in the case of rock scratch testing.
3. The applications often exceed the suitability range of continuum methods.

The current research will mainly focus on modelling of rock scratch tests. There have been a large number of publications on numerical simulation of the rock-bit interaction using continuum and discrete methods; however, after reviewing the available literature, the author concluded that there is no comprehensive research available on this topic. In some cases (e.g. Mendoza, 2013) the simulations were only performed in two dimensions despite the same authors' admission of its limitations. In others, the purpose was only to model a specific rock behaviour. It was also clear that most of the available literature suffers from a lack of proper rock calibration. It is in this context that the current research will use the discrete element method, in three dimensions, and will incorporate the recommendations of other publications. This is to ensure that the final simulations are performed on a fully calibrated rock sample. Prior to the main research, a brief "exploratory" 2D work was performed to allow me to be familiar with the simulation software and explore the mechanics of rock-bit interactions. This is explained in Chapter 5.

It must be mentioned here that there have also been great efforts by several authors to develop analytical models to describe the RST mechanics. Examples include the 2D models of Evans (1962) and Nishimatsu (1972), both of which are proposed for the brittle cutting mode. In general, the main disadvantage of the analytical models is that they are based on simplified assumptions (Rojek, 2011) and are not capable of fully describing the mechanics of rock cutting. Analytical models will not be covered in this study.

Discrete Element Method

Discrete Element Method (DEM) is a discontinuum-based numerical modelling approach. The unique feature of DEM is that it explicitly models individual particles and their interactions, which makes it ideal for soil and suitable for rock mechanics applications. Even if the simplest form of the DEM is used, it can capture many of the key mechanical responses of soil (O’Sullivan, 2011).

The numerical techniques used in DEM can be divided into two groups: “soft sphere” and “hard sphere” methods (Duran (2000) and Zhu et al. (2007)). The main difference between the two methods is the deformation of particles at the contacts. In hard models, no deformation or penetrations of particles are allowed, while in the soft models the deformation is considered. The hard sphere models are suited for rapid granular flow applications such as avalanches or rapid flows through conduits in manufacturing processes. While computationally cheaper, the hard sphere model fails to capture fine response details (O’Sullivan, 2011).

The soft sphere approach, on the other hand, approximates the physical event of colliding or contacting particles. While the particles in “soft” models are still rigid and no deformation is allowed, they can overlap at the contact points. In this method, friction and elastic restitution can come into effect only when the particles overlap (O’Sullivan, 2011).

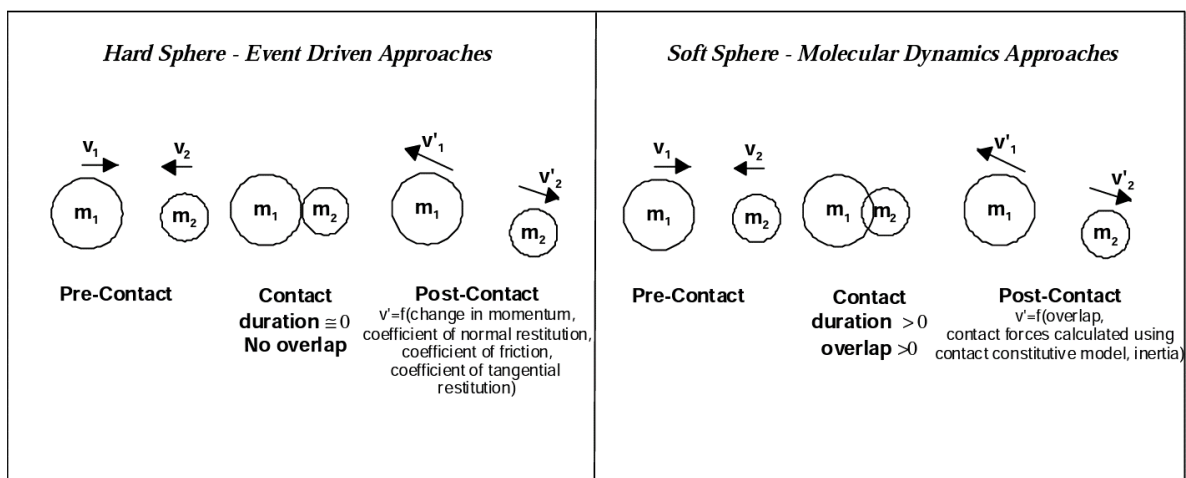


Figure 2-1 “Hard Sphere” and “Soft Sphere” approaches to DEM (O’Sullivan, 2011)

Different algorithms have been developed from the soft sphere concept, however the most commonly used approach is the Distinct Element Method (O’Sullivan, 2011). It is a sub-category of the Discrete Element Method, which was first introduced by Cundall (1971) for rock mechanics analysis and later applied to soil mechanics applications by Cundall and Strack (1979). Due to the dominance of the Cundall and Strack’s approach, the terms “discrete element method” and “distinct element method” are used interchangeably (O’Sullivan, 2011 and Rizo, 2013).

Discrete element model by itself can be divided into two groups: block DEM and particulate DEM. Because both of these are related to the same family of numerical methods, their fundamentals are the same. They both simulate an object by individual bodies (blocks or particles). The bodies can move and rotate and as the system deforms, the existing contacts can break and new contacts can form. The deformations of real bodies (e.g. grains in a rock or soil application) at contacts are considered by allowing for the small overlap at the model contacts. Constitutive models correlate the contact forces to the overlap magnitude. The dynamic equilibrium equations of the system can be solved to calculate the acceleration of each body based on its contact forces and inertia. At each time-step, the accelerations are used to calculate the displacements and this progressively continues until the required criteria for ending the simulation is met. The block and particulate models are different in that blocks are deformable, while the particles are rigid. This makes the block approach more computationally expensive (O’Sullivan, 2011).

Only particulate DEM is used in this research. The base particles are in the form of a circle for 2D and a sphere for 3D models. Where other grain shapes were required, an assembly of these base particles was used to approximate the required geometry. This will be explained in Chapter 4.

DEM Overview

The basic concept of DEM was briefly explained above. This section aims to present a high-level summary of the formulation and the contact models. The materials are summarized from a number of sources including O’Sullivan (2011), Itasca PFC Manual and Potyondy (2014).

In a DEM model, a rock or soil sample is simulated by an assembly of individual particles (disks (2D), balls (3D) or clumps / clusters), often randomly packed next to each other. Figure 2-2 shows an analogy between the physical and numerical samples.

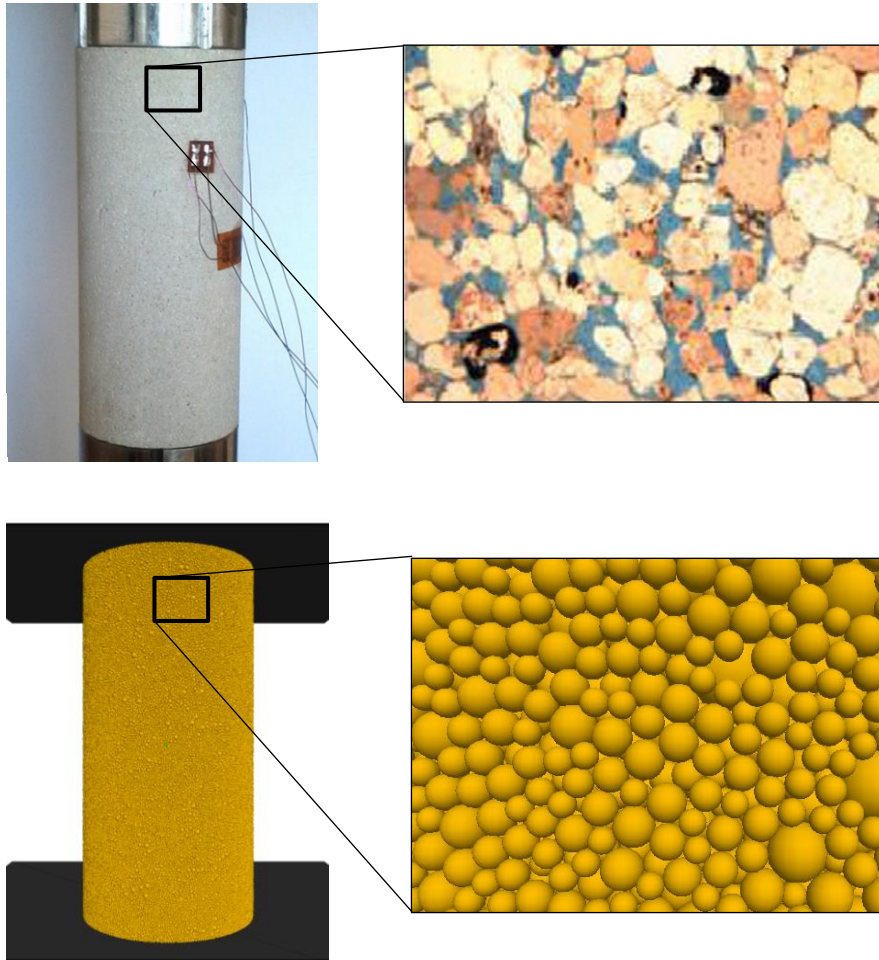


Figure 2-2 Analogy between the physical and numerical samples. Microscopic picture after Peksa et al. (2015)

The above description defines a major difference of continuum-based models and DEM. While in continuum models the mechanical properties (UCS, E , ν , etc.) of the rock samples are direct model inputs, in DEM the model inputs are properties of the individual particles and contacts. These are called micro-properties and include particle size, particle size distribution, elasticity, friction, normal to shear stiffness ratio, contact strengths, etc.

The term “ball properties” can be misleading. While some properties such as density are directly used in the calculations, it must be noted that the balls only interact at contact points. For this reason, the defined elasticity, K_n/K_s ratio in fact refers to the contacts rather than the balls. This explains why the contacts are the most important part of a DEM model and extreme care should be exercised while assigning the contact properties. This process, which is called calibration, will be covered in Chapter 4.

Figure 2-3 shows the typical sequence of the calculations in a DEM simulation. Once the contacts are established and the force at each one identified, the resultant force on the particles are calculated and is used to determine their accelerations, which in turn are integrated to calculate the velocities. Once velocities are known, the displacements are calculated and the particle positions are updated.

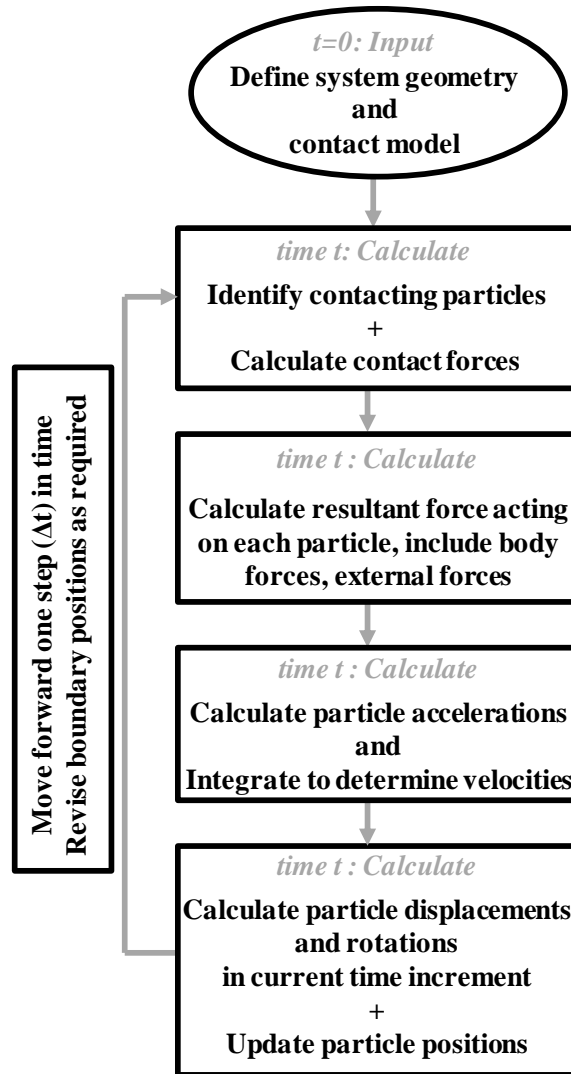


Figure 2-3 Sequence of calculations in a DEM simulation (O'Sullivan, 2011 [with minor editions])

Then, the algorithm shown in Figure 2-3 is used to calculate the particle acceleration, velocities and positions at the next time-step. Ignoring the damping effects, the equilibrium equation can be written as:

$$Ma + K\Delta x = \Delta f \quad (2.1)$$

where M is the mass, a denotes the acceleration, K is the particle stiffness, Δx is the overlapping magnitude and Δf shows the resultant force on the particle. The major difference between the available DEMs is the algorithm used for time integration of Equation 2.1 (O'Sullivan and Bray, 2003) and calculation of the critical time-step.

The integration algorithms can be divided into explicit and implicit. Cundall and Strack (1979) proposed using an explicit central-difference integration method. The advantage of using the explicit method is

the higher efficiency, while its main failure is that it is conditionally stable. In other words, a very small time-step is required in the explicit simulations. Several authors have proposed to use implicit time integration scheme to avoid the stability issues, however due to the huge amount of calculations required, it is not always practical (O’Sullivan and Bray, 2003). The software used in this research uses explicit time integration. The rest of this section will only explain this method.

As stated by Cundall and Strack (1979), the time-step used in explicit integration must be so small that the changes in one particle’s position (disturbance) can only propagate to its nearest neighbours. This imposes the largest restriction on the DEM simulations. Often the time-step required for a stable calculation is so small (10^{-9} seconds) that millions of cycles are required to model a very short period of time. To overcome this, often researchers increase the speed of moving parts (walls in a compression test, cutter in a rock scratch test, etc.), which can result in unreliable results. This will be explained later in Chapter 5.

The time-step calculation is extremely important. A too large time-step will result in solution instability and erroneous results propagating through the future calculations. A too short time-step, on the other hand, will unnecessarily slow down the simulation.

It must be understood that the time-step value is not the only critical parameter affecting the accuracy of the results. In DEM, once the model is set up and the contacts are identified, the current status of the particles is used to predict the state of the system in the next time-step. Then the dynamic parameters and particle locations are updated and the calculation continues until the end of simulations. The numerical methods to perform all these calculations, especially the integration methods, are only approximations and their limitations should be carefully considered.

O’Sullivan (2011) reviewed Sutmann’s work (2002) and summarized the source of errors in DEM from a molecular dynamics perspective. The differential equations used in the model are in fact idealizations of the real physical systems. This limits accurate prediction of the system behaviour. On the other hand, numerical solution of the equations involves specific approximation errors, including round-off and truncation. Truncation errors are often much larger than the round off errors and occur while calculating the incremental displacements based on the obtained accelerations. A reference to Taylor series expansion helps to understand the concept. The application of Taylor’s series in numerical modelling is often related to an approximation of the value of a parameter in the next step by using the values available at the current time. This can be shown as equation 2.2.

$$X_p^{t+\Delta t} = X_p^t + \Delta t \left(\frac{dx_p}{dt} \right)^t + \frac{\Delta t^2}{2!} \left(\frac{d^2x_p}{dt^2} \right)^t + \frac{\Delta t^n}{n!} \left(\frac{d^2x_p}{dt^n} \right)^t + O(\Delta t^{n+1}) \quad (1.2)$$

where $X_p^{t+\Delta t}$ is the position of a particle at the next step, X_p^t is the current position and $O(\Delta t^{n+1})$ is the truncation error. The error is proportional to Δt^{n+1} and introduced because only the first n derivatives of X_p were used in the calculations. Because $\Delta t \ll 1$, the greater the number of the derivatives used in the calculations (n), or the smaller the time-step, the smaller is the error.

The integral method used for calculations must be stable. The stability can be defined as having a linear relationship between the global and local error. If the error introduced at each time-step is denoted by E_r , the integration is stable if the cumulative error after n cycles of calculation becomes $C.n.E_r$, where C is a constant. However if the global error has a value of $C^n.E_r$, the error will grow exponentially, which indicates an unstable method. In a stable integration, the total energy of system will be conserved, while in the unstable systems, there will be a drift in the system energy (O'Sullivan, 2011).

Time-step Calculation

Time-step calculation is a major part of the integration process described above. The integration is required to calculate displacement, hence the position, of a particle once the acceleration of the particle is calculated. While the concept of time-step calculation is explained by many authors, ItascaTM PFC¹'s Manual (2017) presents a practical method for determining a best value and the different constraints that are required for this. The time-step must be optimised to avoid instabilities or long run times.

Before calculating the time-step, the assembly must be formed with the particles packed as required. Then the initial contacts are defined and installed between the particles. This will be covered in more details in the next sections of this chapter. During the run, to update the contacts (form new contacts between two particles which were not touching before, or delete a contact between previously touching particles which are now separated), PFC uses a special searching algorithm. The simulation space, called the model domain, is the box containing all the system components. The domain is divided into smaller boxes called cells. The cell structure enhances the particle search because it limits the search into the region of interest. If more than a pre-defined number of particles are located inside each of these cells, it would in turn be divided into child cells. Figure 2-4 explains the concept.

¹ PFC has two modes, namely PFC2D and PFC3D, for two and three-dimensional modelling respectively.

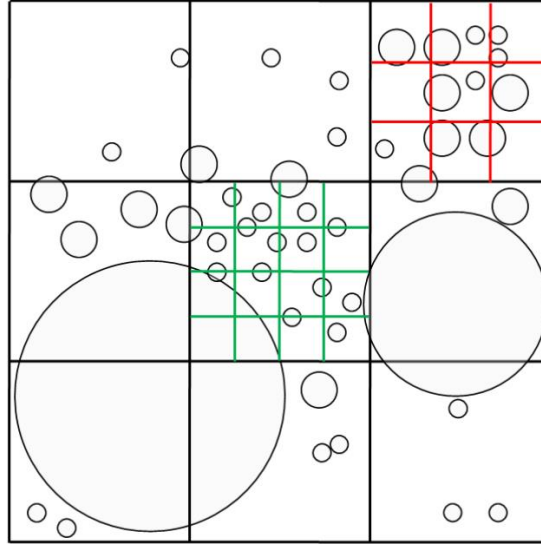


Figure 2-4 Domain, parent and child cells (Itasca PFC Manual, 2017)

PFC also uses an algorithm to detect the particles that are getting close. This is based on marking an area around the particles, which is then mapped into the cell space. As the particles move, the area is re-mapped and possibly shifted from one cell space into the other. If two particles are sufficiently close, a new contact will be formed. Once they are deemed far, with no overlapping, the contact between them will be deleted. The algorithm guarantees having a full assembly of particles with proper set of contacts at each time-step.

The time-step in PFC is defined based on the kinematic and stiffness constraints. The kinematic constraint is mainly introduced to ensure that necessary contacts are created before particles come into contact. For this, each particle can only move less than ϵ , which is called the tolerance factor and is related to the area defined around each particle. The translational acceleration of each particle can be calculated using Equation 2.3.

$$a_i = \frac{(F_i + g_i * m_g + Fa_i)}{m_i}, \quad (2.3)$$

where the subscript i shows i^{th} component, F_i is the contact force, g_i is the gravity force, m_g is the gravitational mass, Fa_i is the applied force and m_i is the inertial mass. A particle with an acceleration of a over a time of duration t will be displaced by x , which can be calculated by Equation 2.4.

$$x = v_0 t + \frac{1}{2} a t^2 \quad (2.4)$$

where v_0 is the initial velocity. The equation can be rearranged to calculate the time.

$$t = \frac{(-v_0 + \sqrt{v_0^2 + 2ax})}{a} \quad (2.5)$$

To honour the assumption that none of the particles move more than ε , it would suffice to use Equation 2.5 with the maximum values of velocity and acceleration. The result will be the kinetic constraint of the time-step that ensures the particle movement is limited to ε .

$$t_{kin} = \frac{(-v_{max} + \sqrt{v_{max}^2 + 2a_{max}\varepsilon})}{a_{max}} \quad (2.6)$$

The next constraint considers the system stiffness. Analogy can be made between touching elastic particles and a one-dimensional mass spring system.

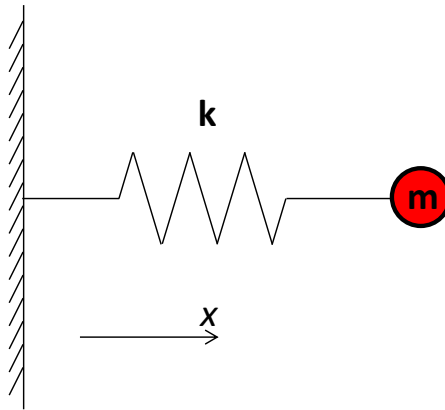


Figure 2-5 One dimensional mass spring system

If the mass is denoted by m and the spring stiffness is k , the system's dynamic equilibrium can be shown as

$$F = -Kx = ma, \quad (2.7)$$

where a is the acceleration of the mass. Assuming a central difference integration, the maximum value of time-step that can be used is $t_{crit} = \bar{T}/\pi$, where $\bar{T} = 2\pi\sqrt{\frac{m}{k}}$, which is the period of free oscillations.

Any values greater than this will make the integration unstable and the results will be unphysical.

In an infinite series of point masses and springs, the smallest period will occur when the masses move in synchronized opposing motion, with no motion at the centre of each spring.

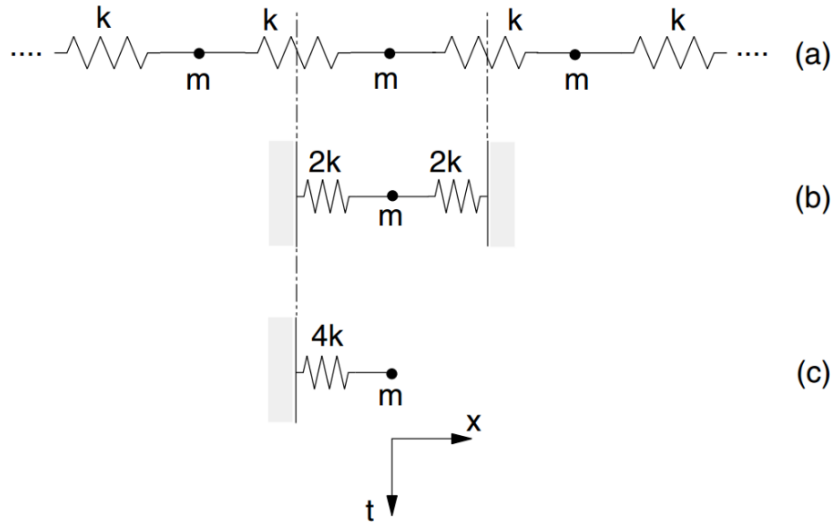


Figure 2-6 (a) Multiple mass-spring system. (b and c) equivalent systems for the centre mass (Itasca, 2017)

Using the same method explained above, the critical time-step for this system is

$$t_{crit} = 2 \sqrt{m/(4k)} = \sqrt{m/k} \quad (2.8)$$

Equation 2.8 shows the critical time-step for transitional motion. The critical time-step of the rotational motion can also be obtained in the same way.

$$t_{crit} = \begin{cases} \sqrt{m/k^{tran}} & (\text{transitional motion}) \\ \sqrt{I/k^{rot}} & (\text{rotational motion}) \end{cases} \quad (2.9)$$

where k^{tran} , k^{rot} and I denote the transitional stiffness, rotational stiffness and moment of inertia, respectively.

DEM considers the simulation model as an assembly of masses and springs. Each body may have a different mass and each spring may have a specific stiffness. A critical time-step is calculated for all degrees-of-freedom of each particle and the minimum of the all is chosen. The final critical time-step is the minimum of the values selected from the kinematic constraint and the stiffness constraint.

An important point that emerges from the discussion is that a few particles, very small or very stiff, can dramatically reduce the critical time-step. This is a point that needs special consideration, specifically when modelling the particle size distribution. The common practice is ignoring the smallest 5% of the particles. Inclusion of this 5% can significantly increase the number of particles in the model and reduce the critical time-step, both of which contribute to the longer simulation runs. This will be discussed in more details in Chapter 4.

Time-step determination requires significant amount of calculations. Disabling the time-step calculation algorithm and fixing the time-step value will improve the efficiency, however great caution must be exercised as using a fixed time-step may result in system instabilities, where particles fly to infinity. This technique, after extensive sensitivity studies, will be used in some of the simulations in Chapters 4 to 7, where no changes in body mass, velocity or acceleration of bodies are anticipated.

Particles in DEM

In DEM, an object is simulated as an assembly of particles. While ideally the individual particles can have any arbitrary shape, for numerical efficiency purposes, circular particles (discs) are commonly used in 2D modelling and spherical particles (balls) are used in 3D simulations. To make calculations more efficient, the particles in PFC are assumed to be rigid, i.e. no deformation is allowed. However, they are considered elastic and can overlap under compressional stresses. Other DEM packages (e.g. UDEC) use blocks instead of circular/spherical particles and allow their deformation, as described earlier in this chapter.

Where a special grain shape is required, clumps can be used, which are collections of circular/spherical particles attached to one another to approximate the shape of interest. Clumps, similar to the constituent discs/balls, are rigid and can translate and rotate with respect to their centre of mass. It should be mentioned here that a model with specific number of clumps takes significantly longer to run compared to a model with the same number of discs/balls, because it has extra number of basic particles.

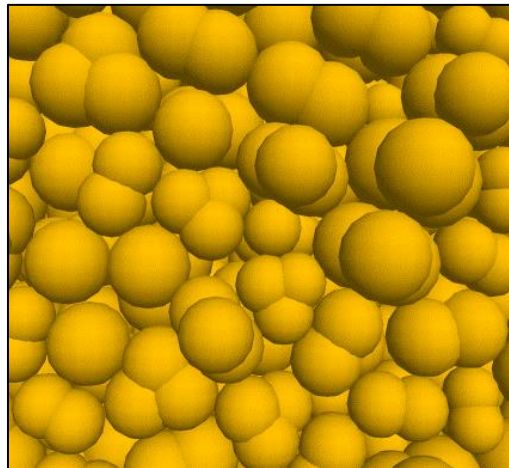


Figure 2-7 Example clump shapes, generated by specifying the relative positioning of the constituting balls

Contacts

The contacts are key components of any DEM modelling. The particles with given size and shape are only required to determine the mass/inertia and calculate the location of the contacts. The magnitude of

the forces and the model behaviour are determined by the underlying “contact constitutive model”, which is the correlation between the contact geometry and the contact forces.

While there are numerous contact models defined in the literature, in this research three approaches will be considered, namely linear, linear parallel bond and flat-joint models. The following is only a summary of key features of each model. More details can be found in the literature (e.g. Potyondy (2014), O’Sullivan (2011) and PFC Manual (2017)).

The **linear model** is the most basic of the three, which occurs at the point of contact. It resembles the behaviour of an infinitesimal interface that cannot resist tension or moment. It is analogous to the contact occurring at the touching points of uncemented discs/spheres.

Figure 2-8 shows the components of a linear bond. Two springs are attached in normal and shear directions with stiffness values of k_n and k_s , respectively. The contact force is divided into linear and dashpot components, with linear component providing linear elastic frictional behaviour and dashpot component providing viscous behaviour. The two dashpots, with normal and shear critical damping ratios of β_n and β_s produce the viscous response and cause energy dissipation. Sliding, as a result of shear stress, is accommodated by introducing the Coulomb friction model. If shear force (F_s) is less than the product of normal force (F_n) and the friction factor ($F_n \times \mu$), no slippage will be allowed. As soon as F_s becomes equal to $F_n \times \mu$, the contact starts to slide.

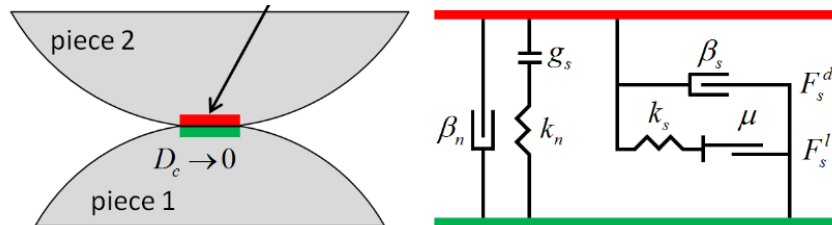


Figure 2-8 Linear bond components (Itasca PFC Manual with minor edits)

The linear model should not be confused with **linear contact bond** model. While the former resembles non-bonded particles, the latter approximates a bonded particle assembly with the bonds forming at the points of contact. Linear contact bond model can resist tensile, however similar to linear model, it is unable to resist moment. The linear contact bond is not suitable for the purpose of the current research and will not be used here. However, in some cases, the linear model will be used to define the unbounded stage of contacts, such as newly formed contacts between the particles, or the contacts between the balls and walls. More information and sensitivities will be provided in Chapters 4 and 5.

Linear parallel bond is a model which resolves the deficiency of the linear contact bonds in moment resistance. This model approximates the behaviour of a finite-sized piece of cement between the grains that can resist moment as well as tension and shear. The assembly of particles connected by linear

parallel bonds is called a Bond-Particle Model (BPM). The parallel bond model is formed by adding a parallel-bond component to the linear component. The bond size is given by λR_{min} , where λ is the radius multiplier and R_{min} is the radius of the smaller ball at the two ends of the contact. Conceptually, the bond size represents the amount of cement. A larger multiplier value shows more cement and a higher degree of bonding, however it does not affect the physical volumes or porosity. There is no direct correlation between the physical cement volume and the multiplier value (O’Sullivan, 2011).

Figure 2-9 shows the components of the Linear Parallel-Bond Model. Of importance is the model’s post-failure behaviour, which reverts back to a point-type linear contact, with no resistance to moment.

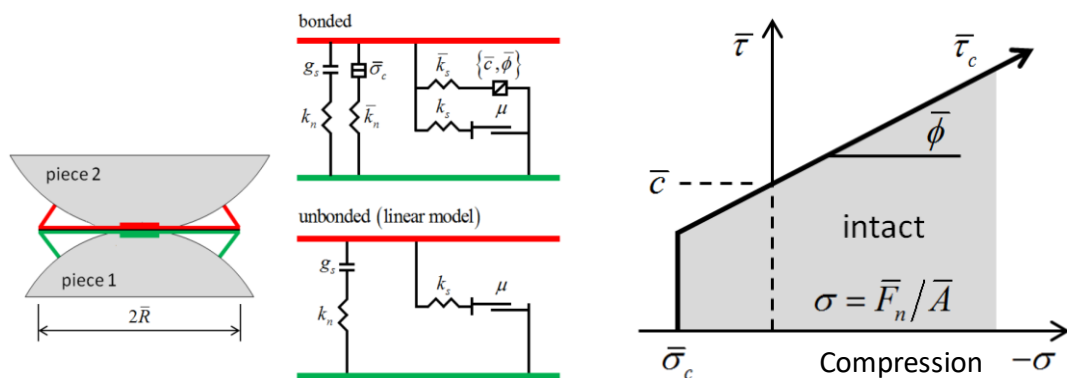


Figure 2-9 Left: PBM components; Right: PBM failure envelope (Itasca PFC Manual with minor edits)

As will be discussed in Chapter 4, one of the main limitations of the linear parallel bond model is its inability to match the ratio of uni-axial stress to tensile stress. Many authors attribute this to a lack of grain inter-locking as a result of the rounded particle shape. Several methods have been proposed to overcome this, including the use of clumps to explicitly simulate the grain shapes, or using alternative constitutive contact models to emulate the interlocking effect. Both methods increase the rotational resistance and facilitate moment transfer to the neighbouring grains.

Flat-Joint Model “synthetically” simulates the behaviour of non-spherical particles. The Flat-Joint bonds can be defined between two rounded particles to change the round contact points to notional flat contact interfaces. Figure 2-10 explains the concept by introducing an analogy between the marble grains with a high degree of interlocking (a) and the flat-joint contacts (b). This type of contact can be used both in 2D and 3D (Figure 2-10b and c, respectively). More importantly, each contact is subdivided into smaller elements which can individually fail while the intact elements still providing resistance to force and moment.

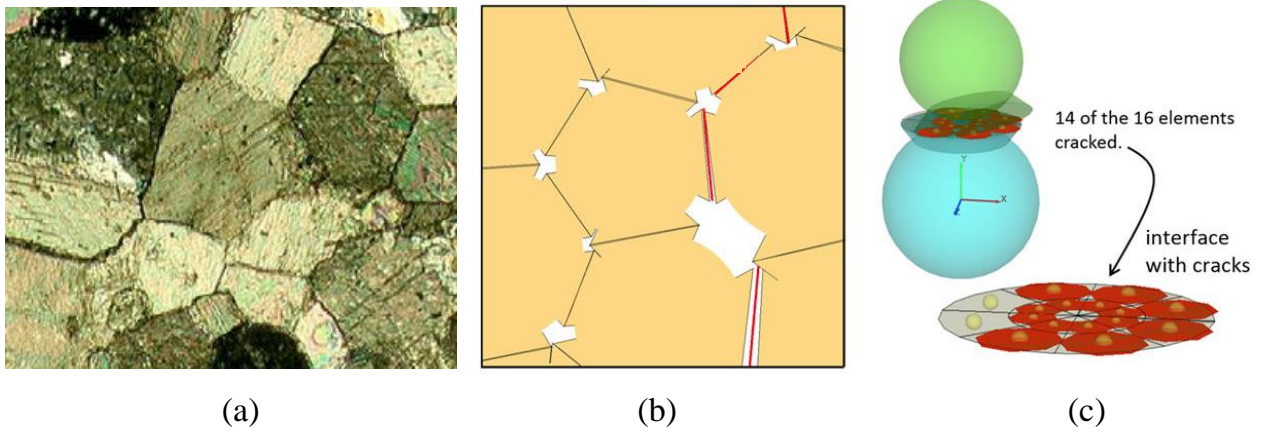


Figure 2-10 Analogy between marble grains (a) [Potyondy, 2015] and a 2D flat-joint model [PFC manual, 2017] (b). A partly failed flat-joint contact between two particles (c) [Potyondy, 2014, with minor modifications].

Itasca refers to the balls of a flat-jointed material as faced grain, each with a core ball and a number of skirted faces (Itasca Manual, 2017). One of the main features of this contact model is that even after the complete contact failure, it is still regarded as a flat interface, capable of resisting moment. This can be compared to the interlocking effect in the granular material, which makes FJM different from PBM. It must be emphasized here that if the balls separate after the failure and the linear model is selected as default (which only affects newly formed contacts), the faces will be removed and the balls will be locally spherical.

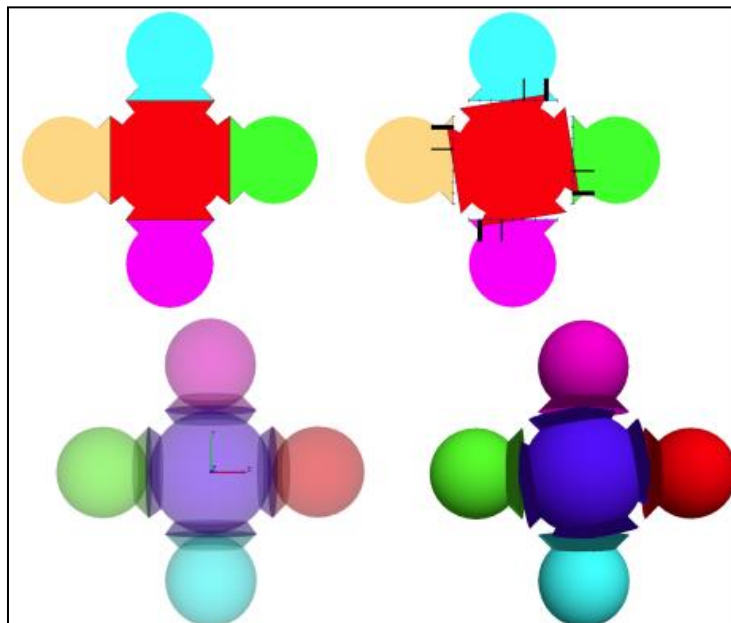


Figure 2-11 FJM resistance to rotation after contact failure (Potyondy, 2014) due to flat interface

The model components are shown in Figure 2-12. A bonded element exhibits a linear elastic behaviour. After the failure, the element becomes unbounded and shows linear elastic and frictional behaviour.

Similar to the previous models, the slip is modelled by imposing a Coulomb limit on the shear force. The flat-joint interface behaviour emerges from the behaviour of its individual elements that evolves from a fully bonded state to a fully unbonded and frictional state (PFC Manual, 2017).

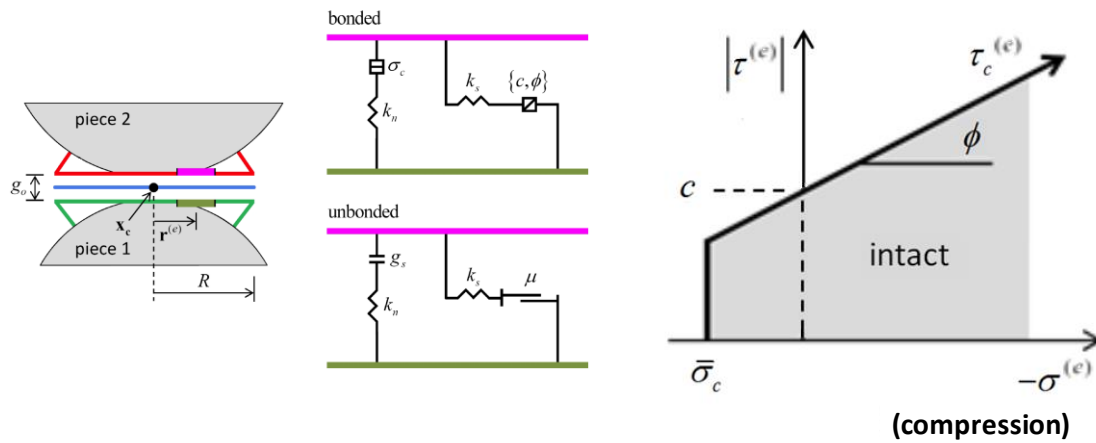


Figure 2-12 FJM components (left) and FJM failure envelope (right) [PFC Manual, 2017, with minor modifications]

The most important properties of a flat-joint contact are the contact cohesion (c), contact tensile strength (σ_c), friction angle (ϕ), friction coefficient (μ), normal stiffness (k_n), shear stiffness (k_s) and the geometrical settings including the number of elements in radial direction (N_r), the number of elements in circumferential direction (N_a), initial surface gap (g_0) and radius multiplier. Itasca uses a method called deformability where the user can specify the contacts' effective modulus (E^*) and the normal-to-shear stiffness ratio (κ^*). Then, the stiffness values are calculated for each contact, based on the particle size as follows.

$$k_n = E^*/L, \quad k_s = k_n/\kappa^* \quad (2.10)$$

where for a ball-ball contact, L is the sum of radii of the balls at two ends of the contact. The same method is also used for parallel bond model.

Three types of flat-joint contacts can be installed between the particles: Bonded contact (type B), that refers to the contacts in which the particles are in touch (gap = 0) and bonded, Slit contact (type S) where the gap is equal to zero but the particles are un-bonded, and Gapped contact (type G) in which the particles are not touching (gap > 0) and are not bonded. Type G resembles an open pore space in a porous rock, type S can be envisaged as a pre-existing crack (Wu and Xu, 2016) and Type B is analogous to a cemented contact.

Damping

The reason for including this section is its importance in DEM modelling and the problems observed in some of the previous studies. The issue with the elastic contact models is that they do not capture the energy dissipation before yielding (rupture of the contact spring). This contradicts the real grain-grain contacts in which plastic yielding and surface damage are observed. The damage dissipates energy. From this point of view, the DEM codes that model the contacts as completely elastic, are unrealistic. The consequence of not considering the energy dissipation will be constant vibration of particles before the bond failure and introduction of the frictional sliding. To resolve this issue, a numerical or artificial damping is introduced to the DEM analysis (O’Sullivan, 2011).

There have been different approaches in introducing this “artificial” damping to the DEM analysis, the most important of which are viscous mass damping and non-viscous local damping. Viscous damping arises from using a viscous dashpot at the contact point and is included in the contact models, however it may not be sufficient to guarantee a steady-state solution in a reasonable number of cycles (PFC Manual, 2017). Mass damping proposed by Cundall and Strack (1979) assumes the magnitude of damping is proportional to a particle’s mass. This approach causes many limitations and was replaced by the local non-viscous damping, proposed by Cundall (1987).

The local non-viscous damping is introduced to the system by adding a damping force to the equations of motion, proportional to the out-of-balance force. The out-of-balance force is defined as the resultant force acting on a particle and causing acceleration. The ratio of damping force to the out-of-balance force is called the damping constant, α . Itasca (PFC manual, 2017) argues that this form of damping has the following advantages.

1. It only damps the accelerating motion. No erroneous forces arise from the steady-state motion.
2. The damping constant is non-dimensional.
3. It is independent of the frequency and equally damps different natural periods using the same damping constant.

The following settings are recommended by Itasca (PFC manual, 2017) for different applications.

Table 2-1 Itasca's recommended settings for local damping

System	Application	Damping constant
Compact Assemblies	To establish equilibrium and conduct quasi-static deformation simulations	> 0
Compact Assemblies	Dynamic Simulation	Contact model based damping strategies are preferred.

		The local damping coefficient should be set to 0.0 or a small value.
Loose Particles	Free flight of particles and/or impacts between particles	Using local damping is inappropriate. Contact model based damping strategies should be used.

Software

PFC™ was selected for the numerical modelling because of its capability in supporting the required contact models, parallel processing and availability at the time of conducting this research. While the main body of the research was performed in 3D, a brief 2D study was carried out at the beginning of the simulations, as will be explained in Chapter 5.

Due to the requirement for very small time-steps in DEM models, large number of simulation steps are required to simulate a short period of time. This necessitates the use of powerful computers. Given the limited nominal clock speed of the available CPUs, the only viable method to reduce the run time is using parallel processing, which is supported in PFC3D (V5.0 onwards). This was tested by running a simple model, made of 79,000 balls, for 1000 cycles. The results, as presented in Figure 2-13, shows significant improvements in the run time by adding more cores, however beyond 6, the improvement was minimal. This demonstrates the limitations of the parallel processing in reducing the simulation time.

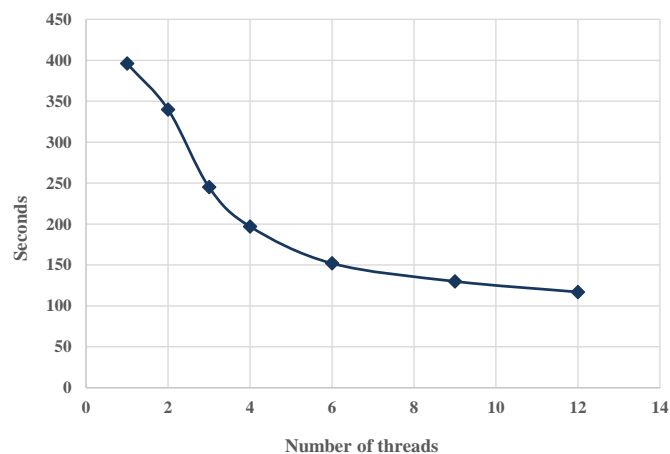


Figure 2-13 Time required to perform 1000 cycles on a sample with 79,000 balls [Joodi, 2015]

The PFC software manual includes several verification examples, where the software is used to model specific problems with known analytical solutions. For the brevity reasons, these will not be repeated here.

3 Literature Review

This chapter presents a summary of the key features of DEM and defines the key terms and issues outlined in the next sections of the thesis. Where possible, the materials are discussed at a high-level. Details are only presented for the topics which will be used in the next chapters.

3.1) Application of DEM in Geomechanics

DEM is one of the fastest growing areas of computational mechanics and has extensive applications in different disciplines including rock mechanics, soil mechanics, structural analysis, granular materials, material processing, fluid mechanics, multi-body systems, robot simulation, and computer animation (Jing and Hudson, 2002). In fact, rock mechanics is one of the disciplines from which the concept of DEM originated (Rojek, 2011). It was first introduced by Cundull and Stark (1979) to model granular assemblies in geotechnical engineering. DEM has the capacity of modelling the material at the microscopic level and capturing all the phenomena that are related to the particulate nature of the granular materials. The solution idea is that by taking a small time-step, disturbances can only spread to the immediate neighbouring discs/spheres (Sallam et al., 2004). This was discussed in more detail in Chapter 2.

Zhu et al. (2007) investigated the number of publications related to DEM by searching the following keywords in the Web of Science: discrete element method/model, distinct element method/model, discrete particle simulation/method/model, and granular dynamic simulation. The results showed that the number of published papers had grown exponentially, demonstrating the increasing popularity and application of DEM in many scientific disciplines. Their work was updated as a part of the literature review for the current study and proved that the trend has continued after 2007. Figure 3-1 shows the updated results.

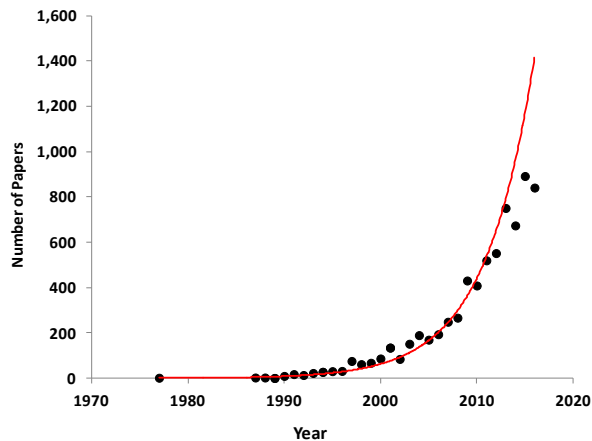


Figure 3-1 Number of DEM related papers (Following O’Sullivan’s (2014) updating method)

O’Sullivan (2014) investigated the DEM-related published papers in geomechanics in selected journals and databases and divided them based on the 2D or 3D applications (Figure 3-2 a). She plotted the number of particles used in the simulations each year (Figure 3-2b). While the general trend appears to be increasing, the rate of increase is not substantial. Another interesting finding was that 67% of the publications in 2010-2013 have used PFC2D or 3D.

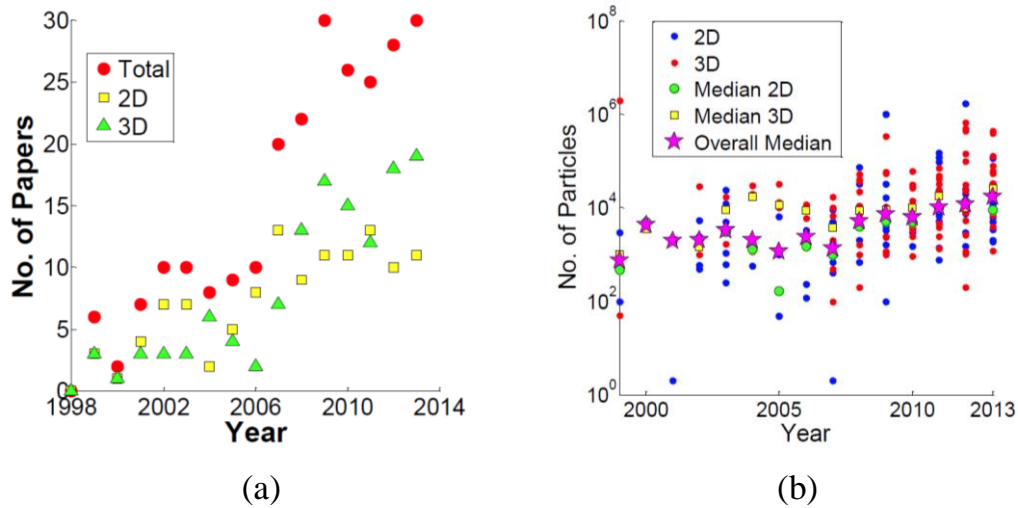


Figure 3-2 (a) Number of DEM related papers in geomechanics; (b) Number of particles used in DEM simulations

One of the main restrictions in the application of DEM in geomechanics is the severe computational expense. Over 2 million particles with an average diameter of 0.35mm (a typical grain size) are required to fill a standard cylindrical core sample (1.5” D × 3” H) with a porosity of 30%. The CPU time required to simulate a UCS test on this sample (UCS ≈34 MPa) is in the order of 1.5 days for a BPM. Flat-joint models, due to presence of multiple elements per contact, require much longer simulation time. It must be emphasized that the test may be repeated several times during the sample calibration phase, as will be discussed in Chapter 4. The PC specifications used for the simulations are listed in Table 3-1. The PC was selected after running a benchmark case (cycling an assembly of 10,000 balls for 100,000 cycles) on different machines and recording the run time.

Table 3-1 Specifications of the PC used for the numerical simulations

CPU	i7-3930k @4400 MHz
RAM	32 GB DDR3
PFC3D version	5.00.23

The purpose of this research, as outlined in the introduction, is to demonstrate the application of 3D DEM in geomechanics. While three applications will be modelled and presented, to avoid confusion and unnecessary details, the literature review will focus only on the material genesis procedure and rock scratch testing. A brief review of the available literature related to other applications (Thick-Walled Cylinder and Erosion) will be included in Chapter 6.

3.2) Material Genesis Procedure

Material Genesis is the first stage of building a DEM sample, in which a compact assembly of particles is generated. The particles are then bonded together with the specified contact model properties. Building representative numerical samples is one of the most challenging parts of DEM modelling. Contrary to the continuum methods, the large-scale material properties (macro-properties) are not direct inputs; instead, they must be matched by tuning the particle and contact properties (micro-properties). The tuning process, also known as “Calibration”, will be discussed later in this chapter.

The material genesis procedure can be subdivided into two phases: packing and finalization. During the packing stage, particles of specified sizes are generated inside a vessel and cycled until they meet an equilibrium condition, which is generally a maximum average unbalanced force. In this research, to achieve a uniform distribution, Itasca’s (Memorandum, Potyondy, 2016) grain scaling procedure was used, as described below and shown in Figure 3-3.

- A cloud of grains with porosity of n_c is generated. During this step, the overlaps are ignored and the generated cloud particles generally have significant overlaps.
- The material’s friction coefficient is set to zero and the particles are allowed to rearrange until they meet the defined equilibrium condition. During this step the large overlaps are eliminated.
- The grain diameters are modified iteratively until the specified confining stress is obtained.

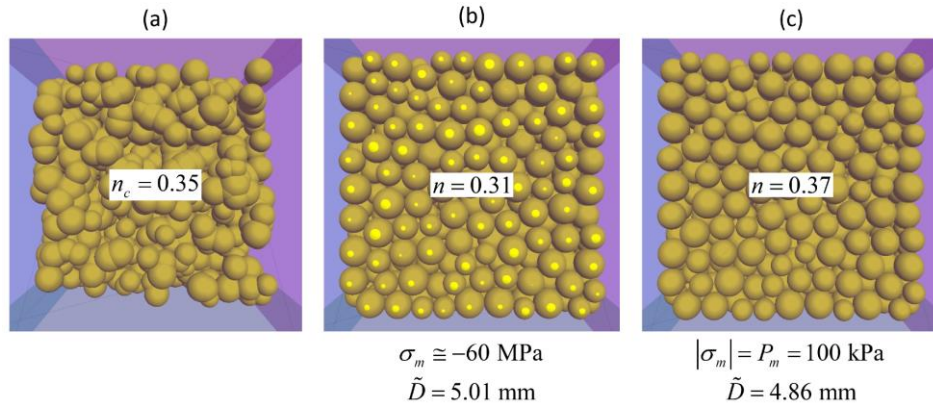


Figure 3-3 Material genesis procedure: (a) generated cloud, (b) rearranged particles and (c) final state of particles after scaling (Potyondy, 2016).

The choice of particle size distribution is an important factor in determining the grain-packing pattern. A uniform particle size ($D_{\max}/D_{\min}=1$) produces a crystalline arrangement, while a ratio greater than one produces more random particle positioning. To get a reasonable response, Potyondy and Cundull (2004) proposed using a D_{\max}/D_{\min} ratio of 1.66 for building hard rock samples.

During the finalization phase, the properties of the current and future contacts are specified. The contacts are installed only between the particles with a gap smaller than the specified value. Selecting proper combinations of micro-properties is challenging and will be discussed in the next section.

3.2.1 Sample Calibration

DEM simulation packages, including Itasca's PFC, work at a basic level as their inputs are the properties of the grains and their interfaces (contacts), which are known as micro-properties. Choosing a suitable set of micro-properties to match the large-scale behaviour of a rock sample (macro-properties) is not straight-forward and requires a significant amount of effort and knowledge.

There have been several attempts to formulate the relation between the micro and macro-properties. Chang and Mirsa (1990) obtained an analytical relation between the balls' stiffness values and the resultant rock sample's Young's modulus and Poisson's ratio. Their analytical solution for an isotropic material simplifies to

$$E = \frac{2r^2N}{15V} (2k_n + 3k_s) \left(\frac{5k_n}{4k_n + k_s} \right) \quad (3.1)$$

$$\nu = \frac{k_n - k_s}{4k_n + k_s},$$

where V is the volume of the packing, r is the particle radius, N is the number of contacts and other parameters are as described in Chapter 2. Clearly, the equation is applicable only if the packing type and the number of contacts per particle (coordination number) are known. On the other hand, if there is a range of different particle sizes or particle shapes available in the model, or if a non-linear contact model is used, the equation is not applicable.

In the absence of a reliable analytical method to adjust the particle and contact properties, the only feasible method is using a systematic trial and error approach. In this method, a standard-size rock sample is generated in the DEM simulator and a set of reasonable micro properties is selected as the first guess. The resulting rock behaviour is assessed by performing a series of simulated mechanical tests, which are normally a replica of the standard laboratory procedures, including the UCS test, confined compressional test, Brazilian test. Iterations often are required to tune the macro-properties to the values measured in the laboratory.

The methodology to perform the test simulations are explained in more detail in Chapter 4. As a quick summary, the UCS test is performed by placing the numerical sample between two parallel plates which are moving towards each other with a specified velocity. The resultant stresses and strains are recorded and processed to calculate the UCS, Young's modulus and Poisson's ratio. The tensile strength can be measured by the Brazilian method or direct tensile test. Different approaches exist for performing a confined test. While Itasca's approach is to use cylindrical walls around the sample to apply the confined stresses, some authors (e.g. Wang and Tonon, 2009) argued that this prevents the sample from deforming naturally. Wang and Tonon (2009) used a specific algorithm to identify the outer-most layer of particles and apply the confining stress directly to the grains. My investigation of the method revealed that applying the confining stress by this method could cause local stress concentration. To resolve this issue, in this thesis an alternative method was used, where a layer of fine particles formed around the cylindrical sample. A proportional radial force is calculated and applied to each particle. The balls in this additional layer are fixed in the z direction (parallel to the axis of the cylinder). The stress measurements showed that this method resulted in a more uniform stress distribution and allowed the rock sample to deform "naturally". More details can be found in Chapter 4.

Many authors have only used the most basic rock mechanical properties, i.e. UCS, Young's modulus (E) and Poisson's ratio (ν), to calibrate the numerical samples, arguing the rock behaviour is mainly governed by these properties. The calibration process for matching these three parameters is relatively straightforward. While almost all micro-properties, including the particle size, affect the large-scale rock behaviour, generally speaking, UCS is mainly governed by the bond strength, E by the contact effective modulus (e_{mod}) and ν by stiffness ratios ($kratio$). It must be emphasized here that these are only the main contributors and as an example, effective modulus has an effect on UCS, or the stiffness ratio affects the sample's Young's modulus.

There have been several attempts (e.g. Fakhimi and Villegas (2006), Yang et al. (2006), Huang (1999) and Rojek et al. (2011)) to use a combination of analytical and trial and error methods to reduce the time required for tuning the properties. In this method, a theoretical non-dimensional analysis is performed based on identifying the important factors affecting a specific macro-property and arranging them as a non-dimensional group. Normally these studies are heavily simplified to reduce the number of parameters and ultimately do not provide an equation. Instead, they are generalized correlations, with some of the micro-properties appearing in more than one macro-property. A good example is the research performed by Yang et al. (2006), where the author, after extensive sensitivity analysis using PFC2D, presented the relationships shown in Equation 3.2.

$$E = E_c \Phi_E \left(\frac{k_n}{k_s}, \frac{L}{R} \right)$$

$$\nu = \Phi_\nu \left(\frac{k_n}{k_s} \right)$$

(3.2)

$$\sigma_c = \begin{cases} \tau_{b,m} \Phi_c \left(\frac{\tau_{b,m}}{\sigma_{b,m}}, \mu \right) & \text{if } 0 < \frac{\tau_{b,m}}{\sigma_{b,m}} < 2 \\ \sigma_{b,m} \Phi_c \left(\frac{\tau_{b,m}}{\sigma_{b,m}}, \mu \right) & \text{if } \frac{\tau_{b,m}}{\sigma_{b,m}} > 2, \end{cases}$$

where $\sigma_{b,m}$ is parallel bond normal strength, $\tau_{b,m}$ is parallel bond shear strength and n is the porosity. The rest of the parameters are as described in the previous chapter. The correlations were used to generate cross-plots of macro vs micro properties and find the line of best fit. Rojek (2011) performed a similar non-dimensional analysis for 2D and converted the results to 3D by replacing the geometrical settings of a 2D model with those of a 3D case.

The non-dimensional analysis described above, while providing some insight into the underlying parameters, has limited practical application in finding the proper set of micro-properties. This is mainly due to the excessive simplifications, which often makes them limited to a small number of parameters. Correlations of this kind, however, can form a good starting point for selecting the important micro properties for tuning a specific macro-property.

Whatever the method, a series of iterations to reach the final model calibration and obtain the required rock behaviour appears to be a necessity. Itasca (PFC manual, 2017) explains that there are two approaches for calibration of the micro-properties. In “direct modelling”, the properties and geometry of the micro-components are known and used directly as input to the simulator. Modelling an assembly

of glass beads bonded together using a glue with known properties can fall into this category. Regretfully the micro-properties of a rock sample cannot be measured directly using the conventional laboratory tests (Vallejos et al, 2016). In the “inverse modelling”, the macro-properties of the rock sample are known. To make a representative numerical sample, the properties of the microscopic constituents are adjusted so that the results of the simulated tests match the known macro-properties.

Castro-Filgueira et al. (2016) used PFC3D to match the stress-strain behaviour of Blanco Mera granite. They found it is not possible to match the post-failure response of the rock sample using the parallel-bond model. The match quality was improved by using the flat-joint model. In a more recent research, Castro-Filgueira et al. (2017) matched the properties of Blanco Mera granite using a flat-joint model. The authors presented two calibration procedures proposed by Itasca and Wu and Xu (2016). Both procedures, as shown in Figure 3-4, are in fact iterative methods, structured to minimize the number of iterations required to achieve the calibration.

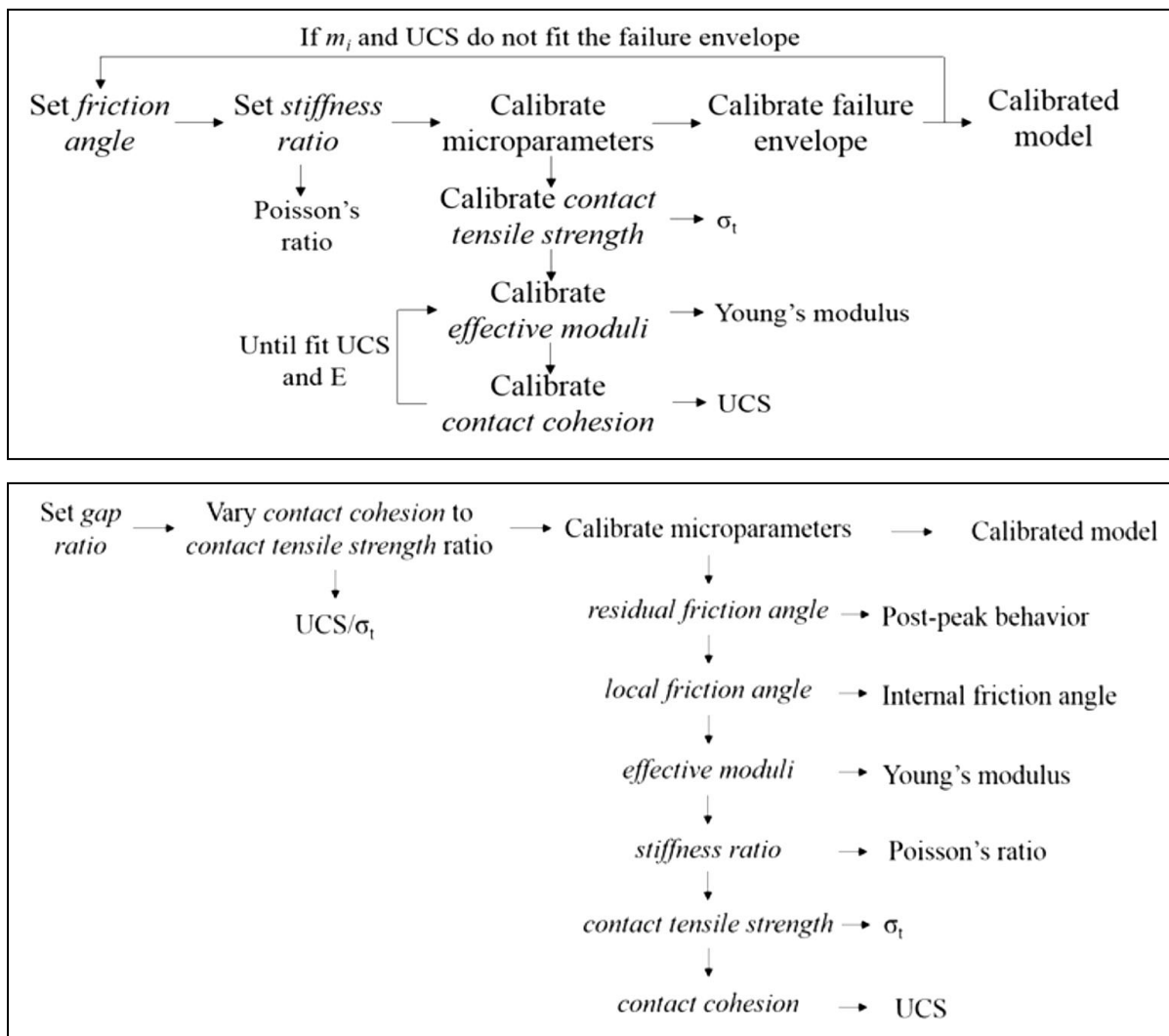


Figure 3-4 The calibration methods proposed by Itasca (top) and Wu and Xu (2016) (bottom) [after Castro-Filgueira et al., 2017]

Ding (2013) pointed out the unrealistically high UCS/T ratios in most of the publications, which is generally a result of using the parallel-bond model. An unrealistic UCS/T ratio can lead to false prediction of crack initiation and propagation. Vallejos et al. (2016) compared the compressive and tensile strengths measured for different rock types versus the values achievable through DEM using a parallel-bond model (Figure 3-5).

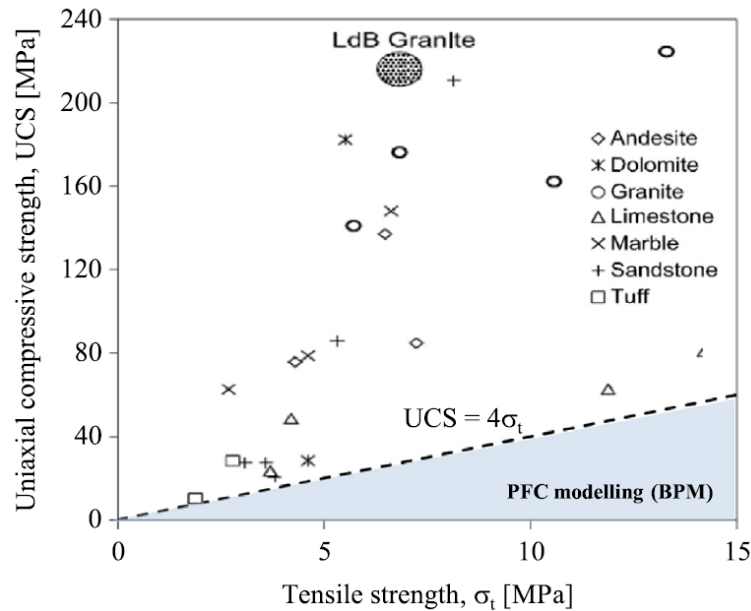


Figure 3-5 Compressive and tensile strength measurements for different rock types versus parallel-bond model (Vallejos et al., 2016)

Ding (2013) noted the recurring issue with most of the available literature, in that the authors often ignored the scale effect without performing any sensitivity on the particle or model size. The model scale normally expressed by L/D ratio, where L is the smallest characteristic model length, such as the width of a parallelepiped sample or diameter of a cylindrical sample, and d is the average diameter of particles. A finer model has a higher L/d ratio. To investigate the scaling factor issue, Ding (2013) summarized the geometrical settings of a number of publications. The summary showed that while for 2D simulations the L/d was in the order of 60-200, 3D simulations were much coarser, with most researches around 20-30. This was in part due to the fact that 3D models contain significantly more particles (and a higher degree of freedom) as compared to the 2D counterparts. A low L/d ratio generally results in the system being too sensitive to the particle size, while once the model is refined to a certain degree, further refinement does not significantly affect the results. The recommended L/d in 2D simulations, for reaching stable results, varies in the literature from 11 (Potyondy and Cundall, 2004) to 50 (Koyama and Jing, 2007). Ding's (2013) own results, for reaching a stable condition, showed a ratio of 25. His results, as confirmed by other researchers (e.g. Potyondy and Cundall, 2004; and Zhang et

al, 2011) also showed that even at higher L/d ratios, there are still some variations to the UCS as the model gets finer.

The effect of porosity on the mechanical properties is one of the items that has not been investigated by many authors. Ding (2013) noted the porosity variation with varying L/d ratio. The porosity value has a more pronounced effect on the rock mechanical properties, as compared to the grain and sample size. Ding (2013) modified the samples with different L/d ratios to get the same porosity and observed that the UCS coefficient of variance reduced from ~41% to ~11%. Rizo (2013) argued that porosity is an important factor in calibrating the rock response and identified two methods for matching the sample porosity. The implicit method is based on the hypothesis that if the macro properties of a rock sample are matched, there is no need to calibrate the sample porosity. In the explicit method, however, the numerical sample's porosity is adjusted to that of the physical rock sample. Rizo (2013) used an algorithm to find the gaps in the generated DEM sample and fill them with smaller particles (Figure 3-6). As discussed in the previous chapter, introducing fine particles to the system is not efficient and will increase the computational costs. This is due to the increased number of particles and a reduced time-step.

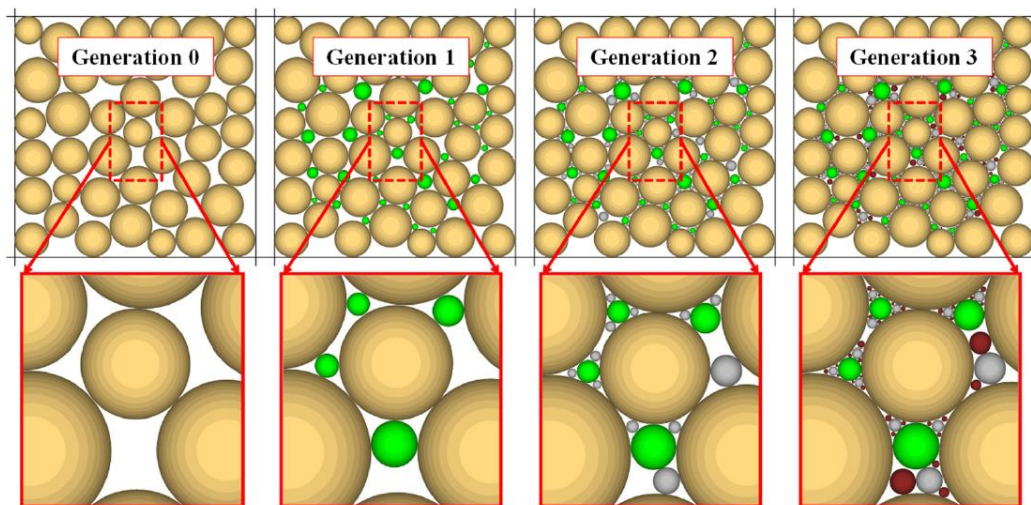


Figure 3-6 Explicit porosity matching process (Rizo, 2013), where additional finer particles are introduced to the synthetic sample in each generation

The other point that is worth mentioning is the choice of the micro-properties representing the balls and contacts. As an example, in a parallel bond model, there are two groups of micro-properties: the parallel bond group which represents the cement properties while the linear group which defines the contact behaviour after the cement failure. The latter can be attributed to the properties of the particle bodies. For this reason, for a parallel bond, or for that matter any other contact type such as flat-joint model, there are two values of effective modulus and stiffness ratios. Theoretically, these values are

independent and can be different. However, to reduce the efforts required to adjust the micro-properties, many authors assumed the same value (average or effective) for both the cement and grains (Potyondy and Cundall, 2004; Yang and Lei, 2004; Wu and Xu, 2016; and Lazzari, 2013).

Wu and Xu (2016) compared the performance of the standard BPM and FJM and summarized the shortfalls of BPM to have (1) unrealistically low UCS/T, (2) very low internal friction angle and (3) linear strength envelope (low Hoek-Brown strength parameter). The authors reviewed the available literature and concluded that these shortfalls occur due to the following reasons:

- Insufficient interlocking in spherical particles.
- Lack of proper rotational resistance.
- Parallel bond shear strength is independent of its normal stress.
- Pre-existing cracks are not included in the model.

Wu and Xu (2016) then argued that the FJM resolves the above-mentioned problems. The pre-existing cracks can be modelled by introducing slit contacts, which occurs between particles that are in contact, but not bonded. Based on their findings, the authors also argued that the normal / shear strength ratio of the FJ bonds should be larger than 1.0 to make the Hoek-Brown strength parameter of the model closer to the realistic values (~2).

Lazzari (2013) only calibrated the UCS, E and ν of the samples using a simplistic model and assumed similar values for the tensile and normal strengths of the parallel bonds. The resultant rock's tensile strength was not measured in her work; however, it is clear that this setting is likely to result in an unrealistically high tensile strength.

Rizo (2013) performed research on DEM modelling of a rock scratch test in 2D. For sample generation, instead of matching the rock samples to specific rock types, he rather simplistically generated several rock types with known UCS values. The author used parallel bonds and only measured UCS, E and ν of the samples. He assumed the Young's modulus of each rock type was 50% of its UCS value.

Vallejos et al. (2016) used an enhanced parallel bond model to simulate 2D veined core-size samples. They noticed that most of the studies on calibration methods were limited to 2D simulations because of its simplicity; however, 3D modelling was limited in the literature. The authors used a relatively simple method to calibrate the intact rock properties as summarized below:

- Match deformability parameters
 - Poisson's ratio by varying $\frac{k_n}{k_s}$. Similar properties were assumed for the particles and parallel bonds.

The authors noticed that by using the enhanced BPM, it is not possible to achieve a brittle behaviour and a consistent Poisson's ratio simultaneously. They used a fixed stiffness ratio that resulted in a Poisson's ratio smaller than the lab measurements.

- Young's modulus by varying the parallel bond elasticity module and stiffness ratio. To produce a brittle behaviour, the authors assumed the elasticity modulus of the particles is 1.5 times the elasticity modulus of the parallel bonds ($E_c = 1.5\bar{E}_c$).
- Match strength parameters
 - Tensile strength by matching the parallel bond tensile strength ($\bar{\sigma}_c$)
 - UCS by matching parallel bond cohesion

The standard deviation of both strength parameters are set to 20%.

The authors (Vallejos et al.,2016) only matched the limited parameters described above. Furthermore, the friction angle was set to 0° to get a brittle behaviour.

Wang and Tonon (2009) generated a DEM code and defined their own contacts. They used a MATLAB optimisation package to reduce the number of required iterations to calibrate the micro-properties. Both unconfined and confined rock responses were modelled in their work. The authors argued that using rigid boundaries (walls) for confined tests may overly constrain the deformation and the results may not be fully representative of the actual test conditions. Instead, they applied the force to the outer-most layer of the sample. This approach allowed a more natural deformation of the rock sample under testing (Figure 3-7).

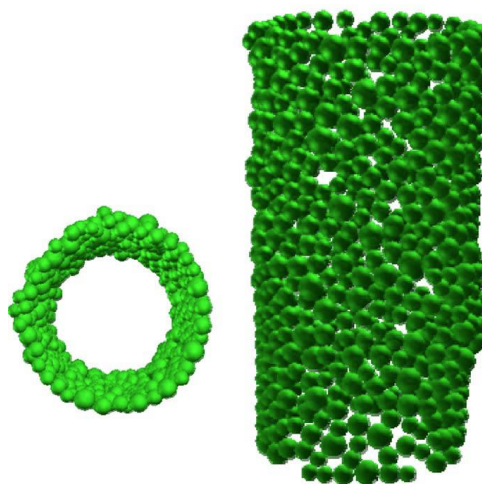


Figure 3-7 Using the outer-most particles to apply the confining force instead of rigid walls (Wang and Tonon, 2009)

Rock Scratch Test

Rock scratch testing (RST) has been a focus of research for many years, mainly due to the fact that it is the simplest form of modelling the rock-bit interaction. It resembles the cutting action of bit cutters while drilling formations underground, however in a controlled laboratory environment. The rationale is to isolate all the affecting parameters (rock non-homogeneities, stresses, pre-existing features, drilling fluid effects etc) and focus on the cutting action of a single cutter on a homogenous intact rock.

The test is performed by moving the cutter relative to the rock sample with a controlled velocity and depth of cut. The response (normal and tangential forces) as well as the cutter's size and shape, are recorded and analysed. Interpretation of the rock cutting phenomenon, even at the simplest form, involves advanced rock mechanics and can be extremely complicated.

One of the earliest theories on the mechanics of rock cutting was proposed by Evans (1962), which in fact was developed for Coal Ploughing. The theory was developed based on the assumption that the failure takes place under tensile stress. Nishimatsu (1972) developed a new theory which considered compressional effects and verified it with the experiments he performed with an orthogonal cutting tool (Figure 3-8). The experiments were performed in a deep cutting mode (2-16 mm), where large chips were formed. He stated that there was no plastic deformation of cutting chips and the observed mode of failure was brittle. Using Mohr's failure criteria, Nishimatsu developed Equation 3.2 for the resultant cutting force:

$$F = \frac{2}{n+1} \cdot S_s \cdot t \cdot \frac{\cos k}{1 - \sin(k - a + \phi)} \quad 3.3$$

where a is the back-rake angle, n is the stress distribution factor (estimated as $12 - (a/5)$), S_s is the shear strength of the rock sample, and k is the internal friction angle. The remaining parameters are shown in Figure 3-8.

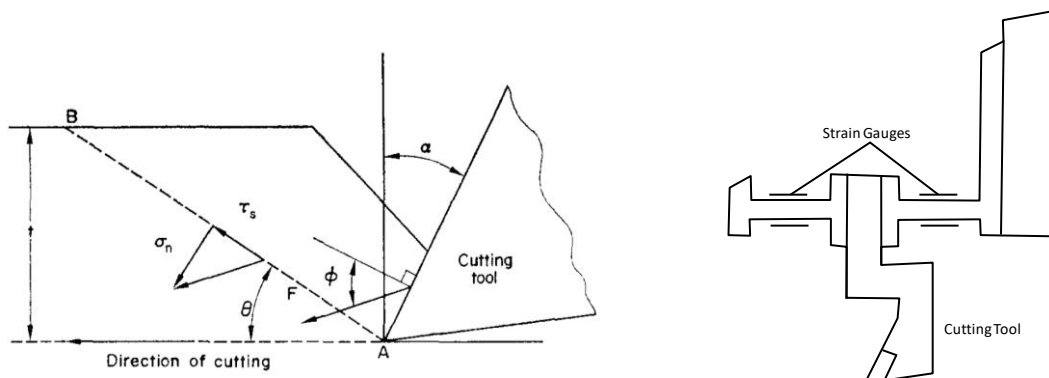


Figure 3-8 Left: The stress distribution and cutting forces for orthogonal rock cutting; Right: The circular plate-type dynamometer (Nishimatsu, 1972; with minor modifications)

One of the greatest steps in modern rock scratch test studies was taken by Detournay et al. (1997) at the University of Minnesota (UMN), where a single-cutter equipment was built to study the effects of rock mechanical properties, particularly the UCS, on the cutting force. Using the same equipment, Richard et al. (1998) conducted scratch tests and concluded that at a shallow depth of cut of 1mm or less, a plastic failure mechanism takes place. He demonstrated the theory which dominates the current view on PDC cutters' interaction with rocks, as follows.

For a sufficiently small Depth of Cut (DoC), the cutting is performed in the ductile regime, which is characterized by severe shearing ahead of the cutter. In larger depths of cut, however, brittle cutting is dominant, which can be distinguished from ductile cutting by the macroscopic fractures initiated from the cutter tip that propagate ahead of the cutter. For a specific rock sample, the depth of cut is known to determine the cutting mode. The cutting force magnitude in the ductile mode depends heavily on the UCS of the rock sample, while in the brittle regime the fracture toughness (K_{IC}) determines the cutting force (Richard et al, 1998). Schematics of the two cutting modes and the corresponding responses are shown in Figure 3-9. The depth beyond which the cutting mode changes from ductile to brittle is called the critical failure mode transition depth (or critical depth of cut). Understanding the critical depth of cut is extremely important due to its influence on the cutting response. Most of the available studies failed to identify the critical depth before interpretation of the scratch data (He et al, 2017).

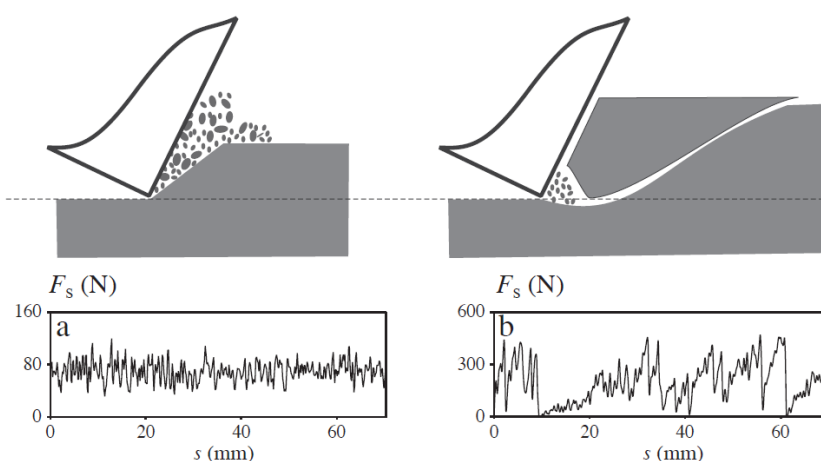


Figure 3-9 Ductile (Left) versus brittle (Right) mode of cutting. The corresponding tangential cutting forces (denoted as F_s) are shown below each diagram. (Richard et al., 2012)

The available test data in the literature shows in shallow depths of cut, a strong linear correlation exists between the horizontal cutting force and the cross-sectional area of the cutting groove. This implies that for a constant cutter width, the horizontal cutting force is proportional to the depth of cut. Figure 3-10 depicts the cutting responses of six rock types plotted versus the depth of cut (Richard et al, 2012).

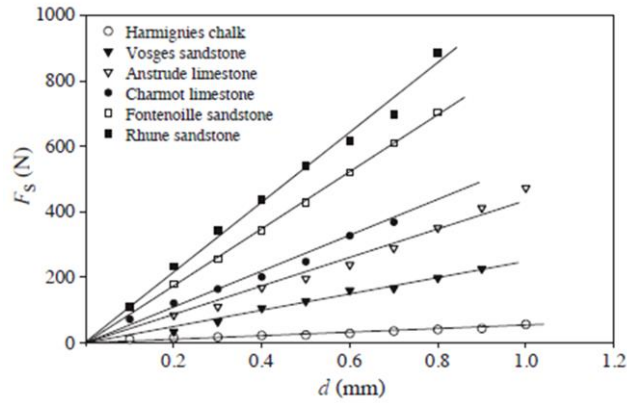


Figure 3-10 Tangential force of a sharp cutter versus depth of cut (Richard et al, 2012)

The tangential and normal components of the cutting force, F_t and F_n , can be expressed by Equations 3.4 and 3.5, respectively.

$$F_t = \varepsilon A = \varepsilon wd \quad (3.4)$$

$$F_n = \zeta \varepsilon A = \zeta \varepsilon wd \quad (3.5)$$

The coefficient of proportionality, ε , in Equation 3.4 is defined as the Intrinsic Specific Energy (ISE). ζ is the ratio of the normal to horizontal cutting force. The word “intrinsic” emphasizes that the energy is solely used for cutting the rock and does not include the frictional energy dissipation through a wear surface. The general term Specific Energy (SE) includes both intrinsic energy (rock cutting) and frictional energy dissipation. It is clear that in the case of a sharp cutter, the frictional forces will be minimal and SE will be equal to ISE. Richard et. al. (2012) cross-plotted the ISE and UCS measurements for 376 rock samples (Figure 3-11) and obtained a clear one-to-one correlation between the rock’s uni-axial compressive strength and the energy required for cutting a unit rock volume.

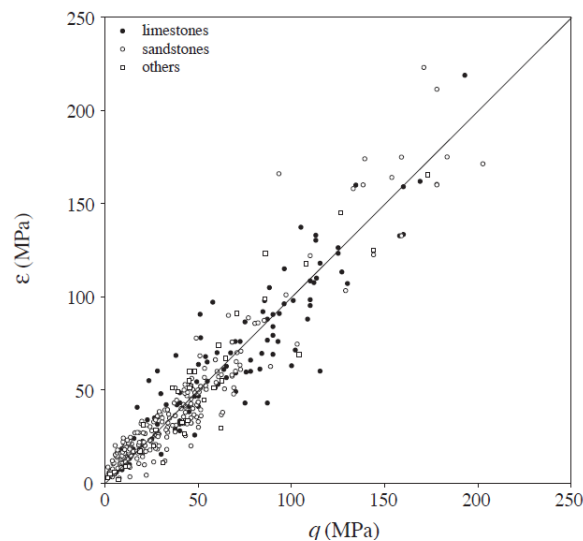


Figure 3-11 Cross-plot of ISE vs UCS for 376 rock samples (Richard et al, 2012)

Richard et. al.'s (2012) study showed that the RST is highly repeatable and the dispersion among the compression test results is one order of magnitude larger than the scratch tests. The calculated coefficient of variation (standard deviation to mean) for the scratch tests was 1.3%, compared to 13% for the uni-axial compressive tests. Due to these reasons, RST can be used as an alternative method for determining the uni-axial compressive strength with several advantages over the conventional compressive test:

- Higher resolution: RST can be performed on a rock sample and identify the changes in the rock strength within millimeters, rather than the larger coring intervals.
- Minimal sample preparation: It does not require the expensive and time-consuming sample preparation necessary for a conventional compressive test.
- RST requires smaller samples and can be considered as semi-destructive, because it only scratches few millimeters of the sample's outer surface.

Given the empirical correlation between UCS and ISE only exists in the ductile cutting mode, determination of the critical cutting depth has been subject to numerous studies. Lin and Zhou (2013) modified the size effect law that was initially proposed by Bazant (1984) for analysing blunt fracture behaviour and proposed a new correlation for predicting the required cutting stress.

$$\sigma_N = \frac{C\sigma_c}{\sqrt{1 + d/d_o}}, \quad (3.6)$$

where C is a scaling factor, d_o is the critical transitional depth of cut, σ_c is the UCS and σ_N is the nominal cutting stress defined as the ratio of the average tangential cutting force to the projected contact area. He et al. (2017) argued that apart from the tangential force, the normal force is also contributing to the cutting. They modified the definition of σ_N term as follows:

$$\sigma_N = \frac{\sqrt{F_t^2 + F_n^2}}{A_b}, \quad (3.7)$$

where A_b is the contact area between the cutter and the rock, i.e.

$$A_b = wd/\text{Cos (Back Rake Angle)} \quad (3.8)$$

The value of C and d_o is obtained by the least-square fitting method. A typical plot of Equation 3.6 is shown in Figure 3-12, which demonstrates the strength and linear-elastic fracture asymptotes for ductile and brittle regions, respectively. The intersection point of the two asymptotes is the critical depth.

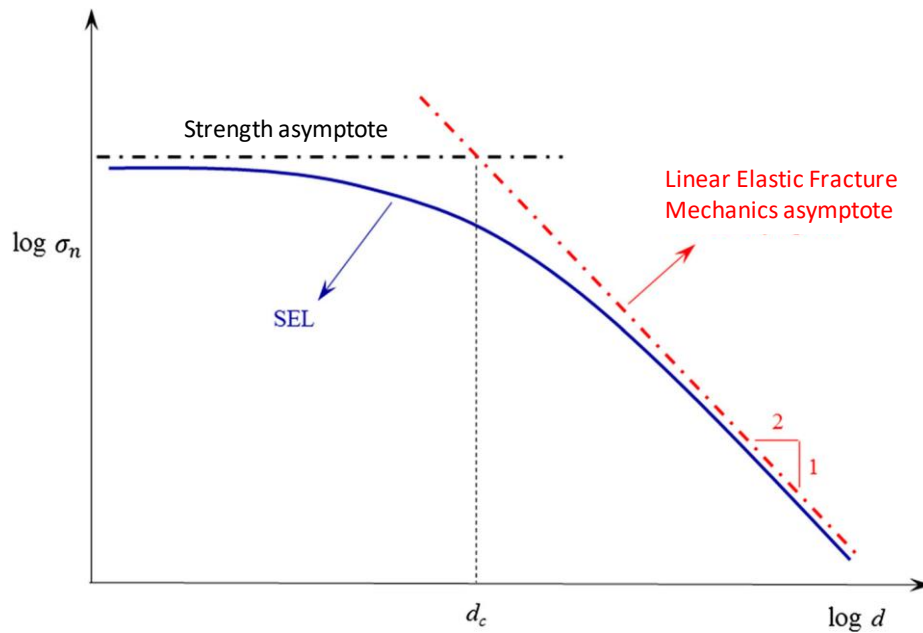


Figure 3-12 Plot of size effect law (He et al. (2017) with minor modifications)

In addition to the experimental approaches, there have also been numerous simulation efforts to better understand the cutting process. While a significant portion of the available literature has been conducted using the continuum methods (e.g. Jonak et al., 2011; Kou et al., 1999; and Korinets et al., 1996), the literature review of the current study will only focus on the DEM simulations to pave the road towards Chapters 4, 5 and 6. A recent example of the DEM studies is the work conducted by Rojek et al. (2011), who used 2D and 3D discrete element models to simulate the rock cutting. Although the cutter used in their study had a different geometry compared to what is being studied in the current research, the results are applicable. The average particle size in Rojek et al's (2011) work was 0.4mm and 2.04mm for the 2D and 3D simulations, respectively. Their goal was to model the lab tests which were predominantly performed in the brittle domain, with a typical depth of cut of 10mm and a high cutting velocity of 1.4 m/s. After performing a dimensional analysis, the parameters were set to match the measured values of Young's modulus, Poisson's ratio and tensile strength. The UCS of the numerical model was not reported. The authors stated the method was unable to match the tensile and compressive strengths simultaneously. As discussed earlier in this chapter, this can be attributed to the relatively simplistic contact model used in their study, which generally suffer from a poor calibration of UCS/Tensile ratio. The 3D model's prediction of the cutting force (Figure 3-13) was ~50% higher than those obtained in the laboratory. The 2D model had a closer prediction of the cutting force, but a much worse prediction of the normal force. Both 2D and 3D models were able to sufficiently match the observed forces' frequency and amplitude.

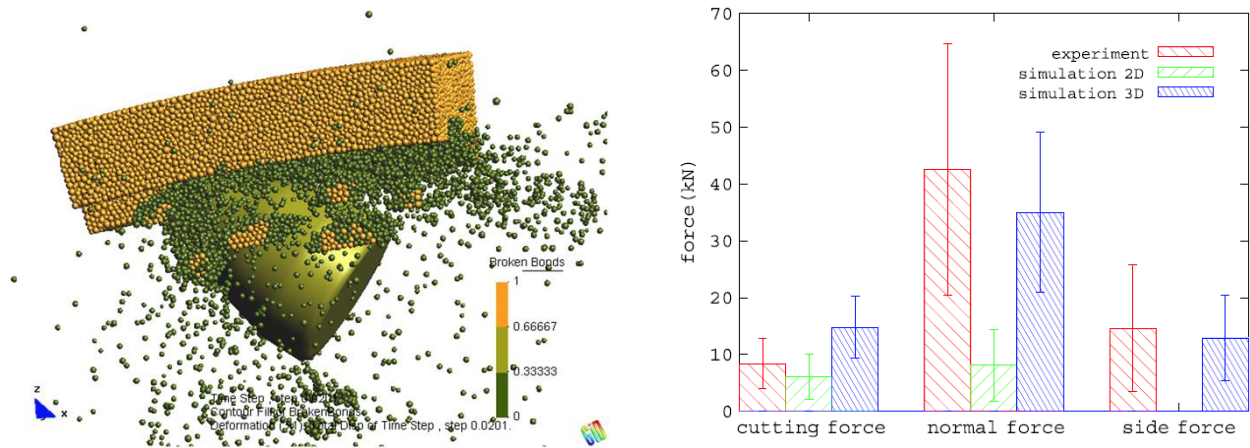


Figure 3-13 Rojek et al.'s simulation set up and results (Rojek et al., 2011)

A similar application was modelled by Su and Akin (2011), where PFC3D was used to model the cutting action of a point-attack pick. To reduce the simulation time, the authors used finer particles immediately around the pick, while the particles progressively coarsened away. The finest particle size was 0.5-0.6mm. They used a parallel-bond model to calibrate only the stress-strain curve obtained in the laboratory. No other properties were matched. When deeper cuts were required, a bigger sample was built with larger particles, without performing a sensitivity analysis on the size effect of the cutting response. Only deep depth of cuts were investigated (DoC=3-9 mm) with a cutting speed of 0.3 m/s, which suggests the cutting mode should be in the brittle region. As shown in Figure 3-14, the simulation results differ from the laboratory measurements, however there is strong linear relationship between the two sets of data.

v

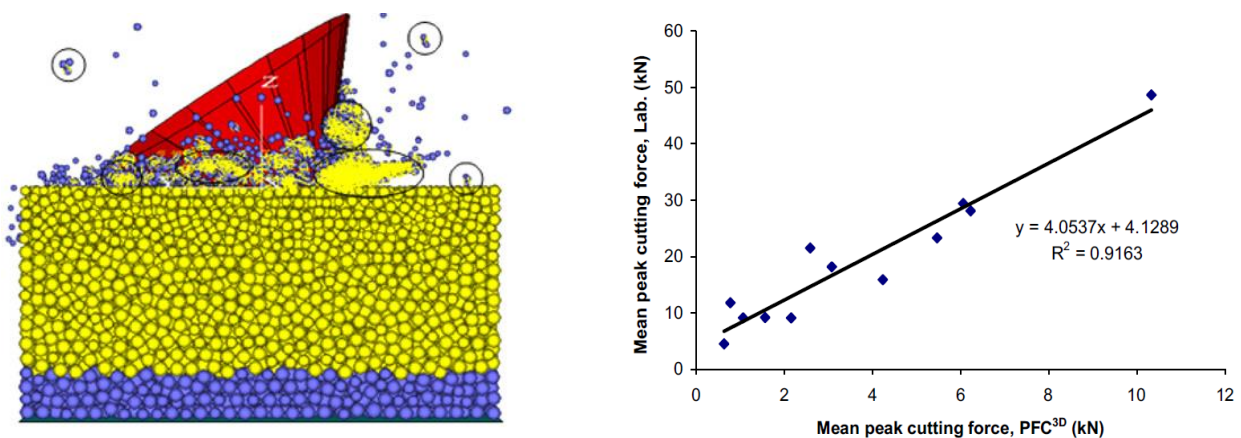


Figure 3-14 Numerical simulations of Su and Akin (2011)

Tan et al. (2008) conducted a research on the microscopic machining process of ceramics using a 2D DEM model. The motive behind their work was the growing demand for a better surface quality after machining. Even at a very shallow cut, micro-cracks may happen due to the friction between the tool and work piece. The authors used extremely fine particles (2.2-3.3 μm). A very small sample (0.8mm \times 0.4mm) was used for testing the UCS strength with the conventional compressive method. The particles were bonded by the Parallel-Bond model and the properties calibrated to match the measured UCS, E , ν , bending strength and fracture toughness. As expected, an unrealistically high value was obtained for the tensile strength due to the intrinsic limitation of the PBM. To model the scratch test, the cutter-sample friction and the cutting speed were set to be 0.17 and 0.05 m/s, respectively. A cutting depth of 5 μm ($2\times$ particle size) was investigated. It is important to note that the simulation speed which was used for validation (0.05m/s) was much greater than the speed used in the laboratory (1mm/min). A plot of cutting force and crack number versus the scratching displacement was generated to identify the initiation of new cracks. This is shown in Figure 3-15.

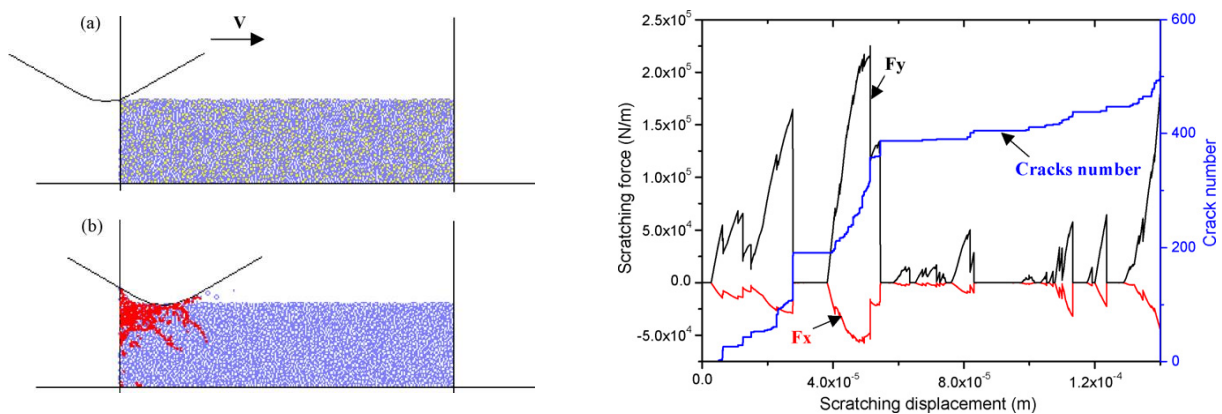


Figure 3-15 Simulation results of Tan et al. (2008)

After validating the crack generation in the DEM model, Tan et al. (2008) used higher cutting speeds of 5, 10 and 15 m/s and concluded that a faster cutter movement results in more cracks beneath the finished surface. Based on the accumulated crack numbers under the cutter, they identified three zones, as depicted in Figure 3-16: an inelastic zone which is dominated by the micro-cracks (OA), a transient zone (AB) and an elastic zone (BE), where there are no micro-cracks.

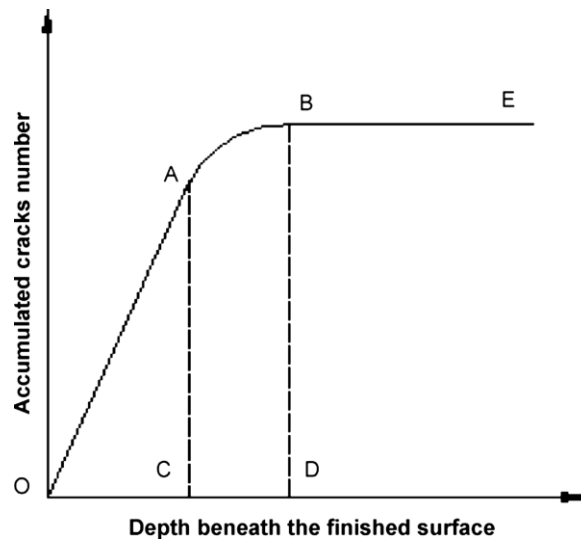


Figure 3-16 Simulation results of Tan et al. (2008)

Wyk et al. (2013) simulated the cutting action of chisel and button-shaped tools on samples made of Paarl granite and a high-strength sandstone. They modelled the high-strength rocks using particle sizes in the range of 0.3-0.5mm, bonded together with PBM. Again, as expected, their model failed to match the compressive to tensile ratio. While the real rock sample's UCS/T is 19.7, the calibrated numerical sample showed a value of 5.3. The authors assumed that matching the uniaxial and triaxial compressive strengths was sufficient for the simulation purposes. No information was reported on the failure envelope of the generated samples. A 12.5mm chisel shaped cutter was used to cut the rock with a speed of 5m/s, which took 1-5 days to run the simulation to move the cutter 20mm. Two depths of cut were investigated: 0.5 and 5mm. The simulated cutting forces were too large, while the simulated normal forces were too small compared to the laboratory measurements. The authors attributed this difference to the cutting conditions, including temperature and distribution of lock-in stresses in the particle assembly. The results of sandstone cutting were relatively complex, with a brief interval showing an average cutting force close to those measured in the laboratory. The recorded normal forces were one order of magnitude smaller than the lab data. After investigating the measured forces and the crack patterns, the authors concluded that DEM was capable of simulating RST process with different cutting tools and the results were verifiable with experimental data.

One of the best available studies on the DEM simulation of rock-bit interaction was done by Rizo (2008 and 2013) as part of his dissertations for Masters and PhD degrees. The studies were done mainly in 2D, with a brief exploratory 3D effort, and covered many sensitivities which were missing in the previous studies.

Rizo (2013) used a specific algorithm to explicitly model the rock porosity in the 2D simulations. Instead of calibrating the samples to match properties of specific rock types, a generic approach was

used in which numerical samples with different UCS and Young's modulus were generated. No other measurements or calibration were performed on the samples. The particle sizes were 0.1 to 0.4mm, bonded using parallel-bond model. A fixed back rake angle of 15° was selected for simulations. The simulation results (Figure 3-17) showed the cutting force linearly increased with cutting depth. This contradicts the experimental observation that beyond a critical depth of cut, the linear trend is lost.

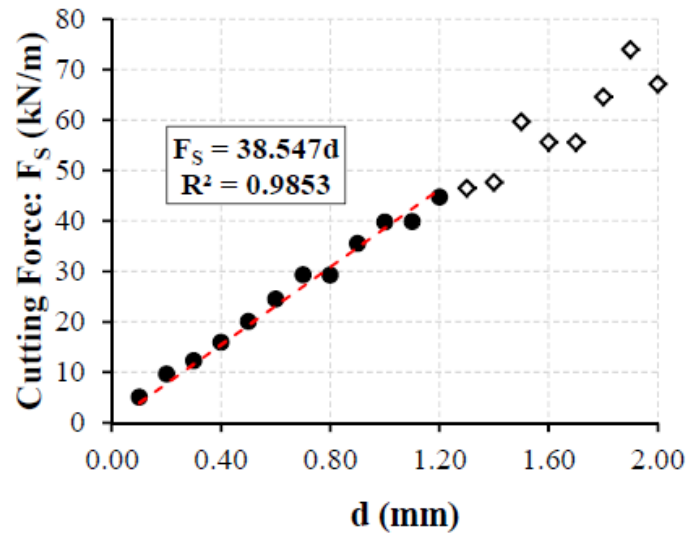


Figure 3-17 RST simulation results of Rizo (2013)

Rizo (2013) argued that the damping coefficient of particles and the cutter speed are two intertwined factors with a significant role in the resultant fragmentation process and cutting forces. Based on the observation, the author concluded that a low damping coefficient would lead to substantial chipping. This, in turn, causes the cutter to lose contact with the rock and a low average cutting force. At higher damping coefficients, the contact between the rock and the cutter was better and the failure was mostly through grinding. A similar conclusion was given for the cutter speed, where a low speed resulted in chipping and a high speed caused grinding. Based on the sensitivity studies, the author used a value of 0.7 for damping coefficient and 2m/s for cutting speed. However, the simulation results showed that these parameters failed to model the deeper cuts, where a lower damping coefficient could be required to match the observed failure mechanism. For consistency, the same values were used throughout the study.

Rizo (2013) tested several parameters in an attempt to calibrate the RST specific energy to the UCS. He tested R_{max} to R_{min} and noted a value of 3.5 resulted in the best match. He then changed the particle size, keeping the particle ratio constant. A higher cutting force was recorded for the finer particles. Assuming the UCS values are independent of the particle size, Rizo (2013) concluded that the use of finer particles improved the agreement between the RST specific energy and the UCS. It must be noted,

however, that particle size also affects the samples' UCS. Reducing the particle size increases the sample UCS, which makes Rizo's conclusion invalid. It is interesting to note that in an earlier chapter of his dissertation, Rizo (2013) had performed a sensitivity analysis on particle size and concluded that "The effect of the particle size on compressive strength is more pronounced for rocks with a strength higher than 60MPa". It should also be mentioned that his calibration, even if it was valid, would only be applicable for this specific set of damping ratio and cutter speed.

Huang et al. (2012) generated their numerical samples with particle sizes of 1.25mm ($R_{dev}/R=0.2$) and parallel bonded model, which failed to model the tensile strength. The authors introduced the characteristic length concept for detecting the transition zone between the brittle and ductile cutting zones. An equation was derived by equating the correlations of ductile and brittle modes to quantitatively calculate the transition depth. They stated using a low velocity value to ensure quasi-static conditions, however the velocity value was not explicitly reported. Instead, it was given as a non-dimensional group of $(V/\sqrt{K_n/\rho})$. Assuming a value of 2,500 kg/m³ for grain density, the velocity used in Haung et al.'s work (2012) was 2 m/s (similar to Rizo, 2013). The resulting specific energy values were 0.6 to 1.1 of the UCS values. While the plot of ISE versus depth of cut was not reported, the trend between the normalized cutting forces and normalized cutting depth deviated beyond a certain depth of cut (transition depth). This was in agreement with the laboratory observations.

3.3) Chapter Conclusions

The chapter reviewed previous attempts on sample calibration and RST modelling. Investigation of the calibration methods and the obtained results showed that sample preparation is a critical part of DEM modelling. A properly calibrated sample is required for any numerical simulation. The best practices for contact models (FJM), performing the confined tests (Tonon et al., 2009), calibration process (Wu and Xu, 2016), increasing efficiency of the RST simulation by coarsening the particles away from the cutting groove (Su and Akcin,2010) and typical cutting speed were identified to be incorporated into the numerical modelling of the current study. The well-established correlations (ISE vs DoC trend and presence of a Critical depth of cut ~1mm) was found to be suitable validation criteria of the RST simulations. Furthermore, the chapter showed the limitations of the available literature:

- Very limited 3D studies.
- Most of the studies have used much larger particles compared to the rock grain size.
- Not all the RST modellers properly calibrated the rock sample. In most of the studies, the calibration was limited only to UCS and E , using parallel-bond model.

- Limited literature was available on the effect of damping factor and cutting speed. Many authors have conveniently used 0.7 and 2-20 m/s for these parameters, respectively.

4 Sample Preparation

4.1) Introduction

Large-scale rock bodies generally exhibit non-homogenous properties, i.e. their properties vary from one place to another. Even if the composition remains the same, the mechanical properties are likely to change due to the variations in the depositional and compaction conditions of sedimentary rocks, the metamorphism environment of the metamorphic rocks and the cooling rate of the igneous rocks. Any of these parameters are location dependant, which causes different properties at different areas. After formation, a rock body may go under further deformations as a result of tectonic stresses which can induce fractures and faults. Representative samples are required to quantify and report the average properties.

The laboratory experiments of natural rocks are generally performed on samples taken from the most uniform parts of the rock masses to avoid the non-representing imperfections such as cracks and veins. These samples are tested using the standard methods to determine the average intact rock behaviour, and the measured properties are used in the calculations or simulations. In DEM modelling, the large-scale average rock properties are called the macro-properties, as opposed to the micro-properties, which refer to the grain-scale characteristics.

3D DEM numerical rock samples are generated by simulating the grains by spheres or clumps, cemented together by contact bonds. The constitutional models govern the way the bonds behave. The ultimate goal of building a numerical rock sample is to re-generate the laboratory results under simulated test conditions.

The analysis and conclusions presented in the following sections are based on laboratory experiments on physical specimens and simulated experiments on the numerical samples.

4.2) Laboratory samples

To perform the laboratory tests, suitable samples should be selected or built to exhibit the required behaviour. The criteria for choosing the proper sample vary depending on the tests. Homogenous samples are preferred when the purpose is to test the behaviour of intact rocks. When the intent is to test features like fractures or veins, the selected sample should sufficiently represent the average features.

The tests conducted in this research required intact rocks to simplify the failure mechanism and assist in interpreting the results. For this reason, the rock scratch tests (Chapter 5) were performed on

Bentheimer sandstone and the erosion and TWC tests (Chapter 6) were conducted on synthetic rock samples.

4.2.1 Natural Bentheimer Samples

Bentheimer sandstone was selected for undertaking the Rock Scratch Tests, mainly because of its homogeneity and availability. Bentheimer is a fine to medium grained, relatively homogeneous sandstone deposited in the early Cretaceous. It is mainly composed of quartz (95-97%) with a porosity of 20-30% and a grain size of 18 to 500 μm . It is subdivided into “Gildehaus” and “Bentheim” varieties, which are different members of the same formation. While Bentheim is less porous and permeable than Gildehaus, both varieties have similar mineralogy (Traska, 2014). The Gildehaus type was used in this research and in the remainder of this dissertation it will be referred to as Bentheimer or Bentheimer sandstone.

Peska et al. (2015) performed a comprehensive study on Bentheimer sandstone and reported the general characteristics, basic mechanical properties and grain size. Figure 4-1 shows a microscopic view taken from their studies. Of importance is the degree of interlocking between the grains. The grain shape is categorized as rounded to sub-rounded.

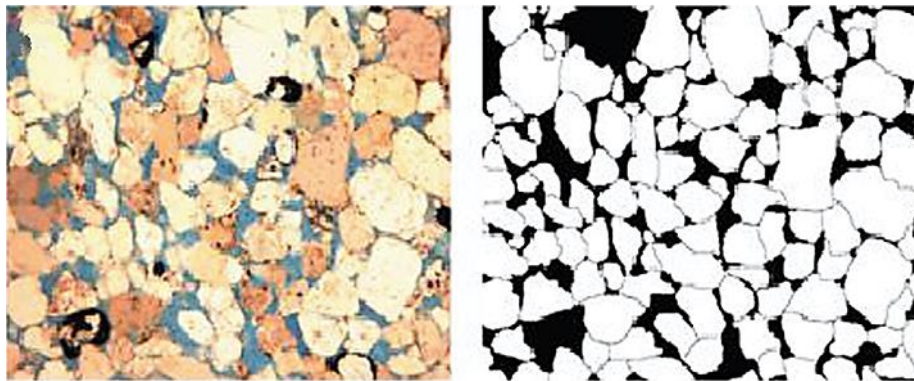


Figure 4-1 Microscopic pictures of Bentheimer sandstone grains. Left: original optical image. Right: binary segmented image. (Peska et al., 2015)

Al-Yaseri et al. (2014) performed micro CT Scan and NMR tests on small Bentheimer samples and reported the pore size distribution, typical grain size, porosity and also several microscopic pictures of the interlocking grains. The porosity of the tested samples was in the range of 21 to 23%. The samples, as measured by X-ray diffraction, were composed of 99.0% Quartz, 0.7% Kaolinite and 0.3% Rulite, which indicates the sandstone consists predominantly of quartz and is quite clean. This is also clearly visible in the microscopic pictures of Figure 4-2, which shows very small deposits of clay on the interlocking sand grains. Note the typical grain size that is in the order of 0.3mm. The importance of Al-Yaseri’s work is that their samples were from the same batch as the specimens used in this research.

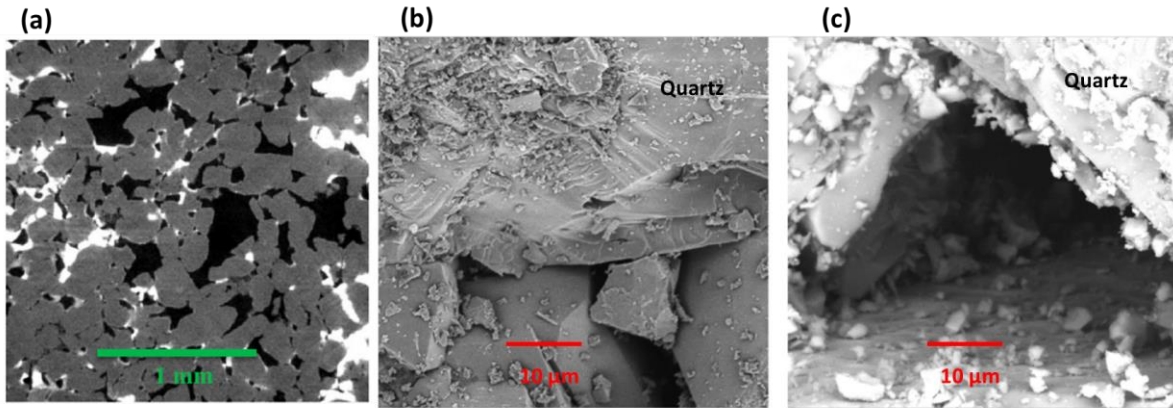


Figure 4-2 (a) 2D slices through the rock and pore space. Sandstone is light grey. (b) and (c): SEM images (after -Yaseri et al. (2014) with minor modifications on the annotations).

The particle size distribution of the Bentheimer sandstone is reported in several publications. Peska et al. (2015) summarized the available data and compared it with their own analysis. All the data sources were in good agreement. The dotted lines in Figure 4-3 were digitized from Peska et al. (2015). To generate a representative particle size distribution for the DEM modelling of the current study, a qualitative average line was generated (solid black line in Figure 4-3) and imported to the PFC3D simulator.

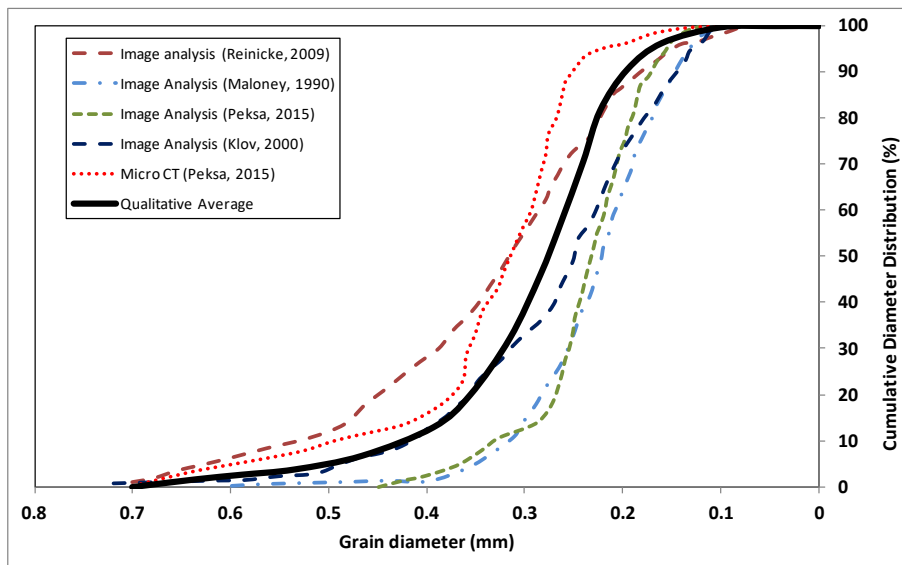


Figure 4-3 Grain size distribution of Bentheimer sandstone. Dotted lines digitized and re-plotted from Peska et al. (2015).

Mechanical Properties

Only the basic elastic properties of the Bentheimer sandstone were found in the literature. To the best of the author’s knowledge, no information was available regarding its confined strength and failure

envelope. To confirm that the samples used in this research have the same properties as described in the literature (e.g. Peksa (2015)), and also measure the confined properties, the author performed several tests in the Geomechanics Laboratory of the WA School of Mines. Figure 4-4 shows the UCS test set-up, both before and after failure.

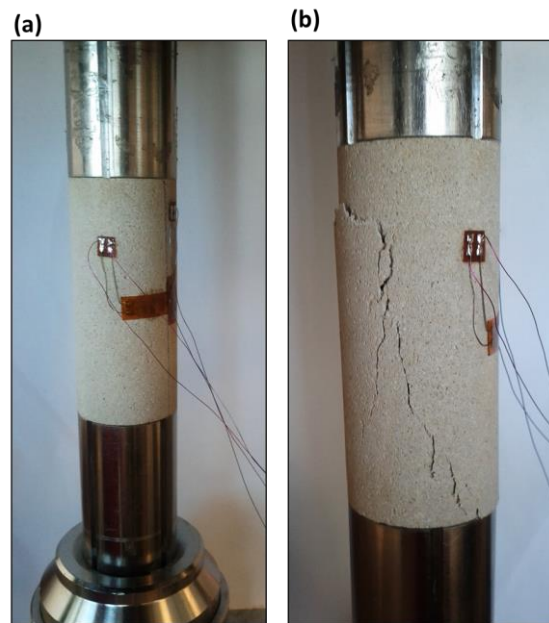


Figure 4-4 UCS test set-up. (a) Intact sample with sensors and (b) Failed sample

Of the five UCS tests performed, two failed due to (1) using an unsuitable glue for fixing the sensors and (2) misalignments in the steel plates above the sample. The remaining tests are shown in Figure 4-5. Due to the equipment restrictions (load rather than strain control), it was not possible to capture the post failure behaviour.

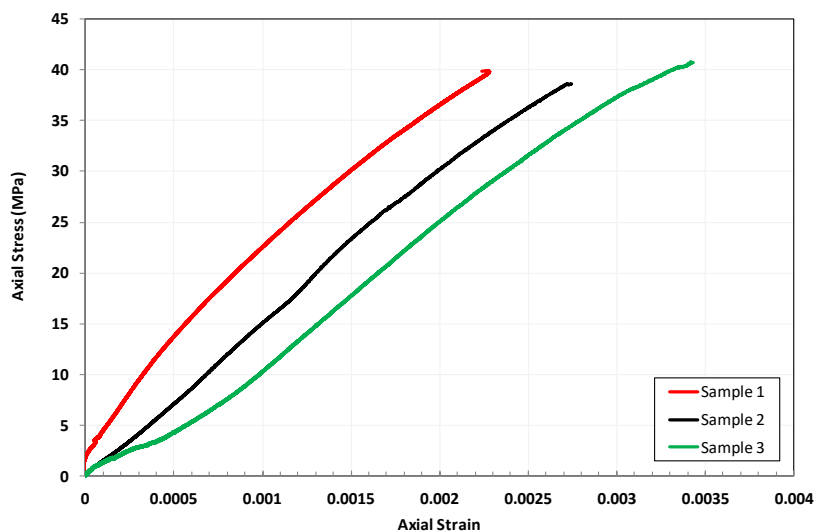


Figure 4-5 Unconfined Compression Test of Bentheimer Sandstone.

The test results are summarized in Table 4-1. The calculated average properties show good agreement with the values quoted by Peska et al. (2015). The results of the current study were used for the purpose of numerical simulations.

Table 4-1 Results of uni-axial compression test

	Peska et al. (2015)	This study
UCS (MPa)	38.93	39.7
Young's modulus (GPa)	14.69	14.85
Poisson's ratio	0.25	0.24

The tensile strength was measured by performing a Brazilian test on a disk cut from the same sample batch. The disk was put under compressional stress in a radial direction and the peak force was recorded. Figure 4-6 shows the experimental set up and the results of the Brazilian tensile test.

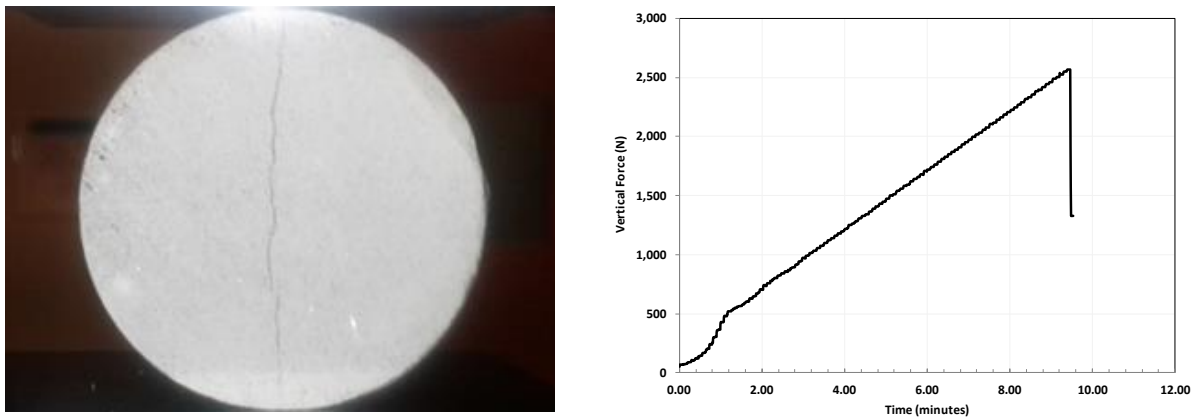


Figure 4-6 Brazilian Test Set up and results.

The tensile strength was then calculated using:

$$\sigma_t = \frac{2P}{\pi DL} \quad (4.1)$$

A value of 2.37 MPa was calculated for the tensile strength, which results in a σ_c/σ_t ratio of 16.8.

A multistage confined test was performed to measure the rock compressional strength at different confining stresses to obtain the Mohr-Coulomb failure envelope and calculate the cohesion and internal friction angle of the samples. The test results are presented in Figure 4-7. The horizontal lines show the confining pressure during each stage.

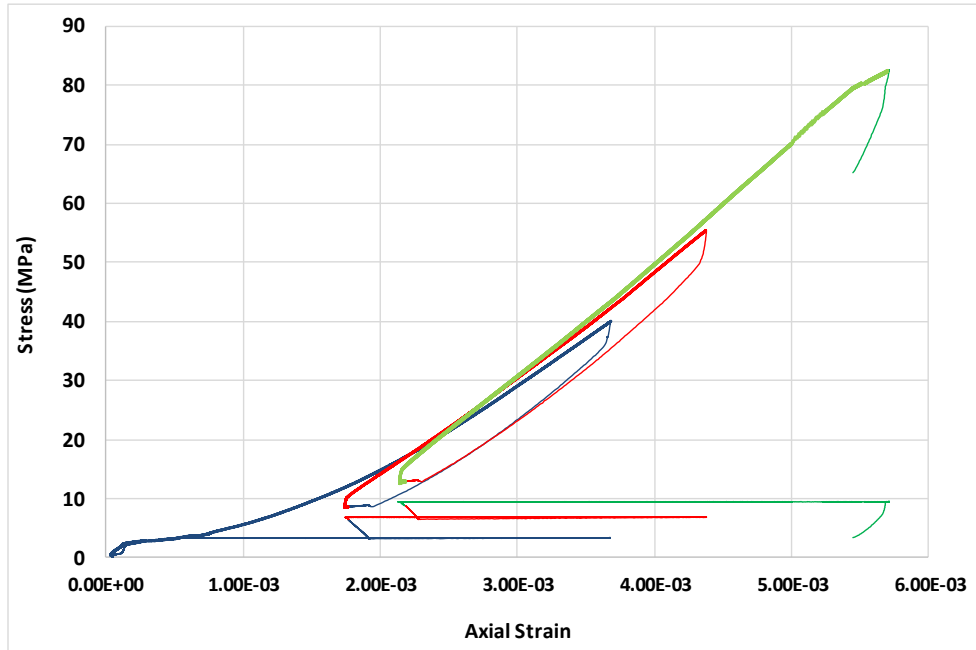


Figure 4-7 Multistage Confined Compression Test of Bentheimer Sandstone

It must be emphasized that the key factor in performing a multi-stage confined test is the unloading point of each stage. Investigation of the loading cycles in Figure 4-7 and their plot in Figure 4-8 revealed that the first and second stages of the test terminated prematurely. For this reason, the compression test was repeated at a confining stress of 6.8 MPa. Only the tests performed under confining stresses of 0, 6.8 and 9.3 MPa were used to define the Mohr-Coulomb envelope. The dotted circles represent the premature confined tests which were excluded from the analysis.

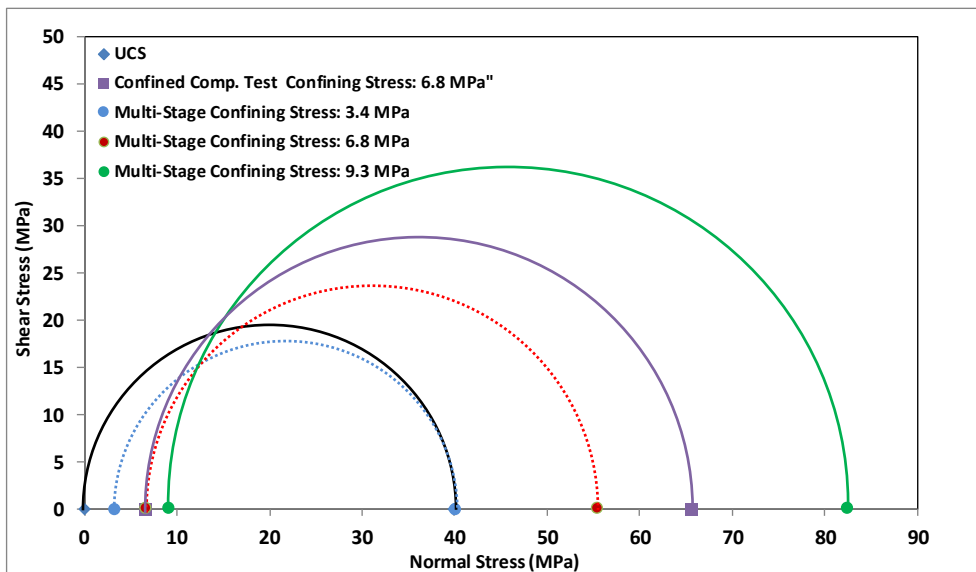


Figure 4-8 Mohr-Coulomb failure criterion generated from UCS and multi-stage test results.

The mechanical properties of the Bentheimer sandstone, based on these laboratory tests, are summarized in Table 4-1.

Table 4-2 mechanical properties of the Bentheimer sandstone

Uniaxial Compressive Strength (UCS)	39.7 Mpa
Young's modulus (E)	14.85 GPa
Poisson's ratio (ν)	0.24
Cohesion	9.24 MPa
Tensile Strength (T)	2.37 MPa
UCS/ T	16.8
Internal Friction Angle	39.2 °
E @ 3.4 MPa conf. stress	16.5 GPa
E @ 6.8 MPa conf. stress	18.4 GPa
E @ 9.3 MPa conf. stress	20.7 GPa

Regretfully the post failure behaviour of the samples could not be measured using the available laboratory equipment. The most relevant data was found to be related to the confined curves of the Bentheim variety (Klein et al, 2000), which shows strain softening at 10MPa confined stress.

4.2.1 Synthetic Samples

Two geomechanical applications will be presented in Chapter 6, where DEM is used to model Thick-Walled Cylinders (TWC) under compressional stress and loose sands exposed to fluid erosion. The models were validated using synthetic rock samples, which were built as a result ongoing PhD programs at the Petroleum Engineering Department. The use of synthetic samples in the laboratory experiments of these applications is deemed more suitable because:

- the sample composition is known,
- it is possible to generate more uniform samples, and
- it provides the flexibility to generate rock samples with the required properties.

The synthetic unconsolidated sandstone samples used in TWC tests were prepared by the method proposed by Younessi et al. (2012), however we made several modifications in the curing process (Tehrani, et al., 2017), arguing that curing the samples in water causes cement wash out. An alternative method was proposed to cure the samples in sealed containers. This ensures consistency of different batches. The mechanical properties of the sample used for the TWC experiments are shown in the table below.

Table 4-3 Properties of the synthetic sandstone used in TWC tests (Tehrani, Joodi et al. 2017)

Physical properties	
Bulk density	1185 kg/m ³
Porosity	26 %
Elastic Properties	
Uniaxial compressive strength	17.92 MPa
Young's modulus	5.9 GPa
Poisson's ratio	0.25

The particle size distribution of the sand used for building the synthetic sample was measured by sieve analysis. This is shown in Figure 4-9 and was directly used in the numerical modelling.

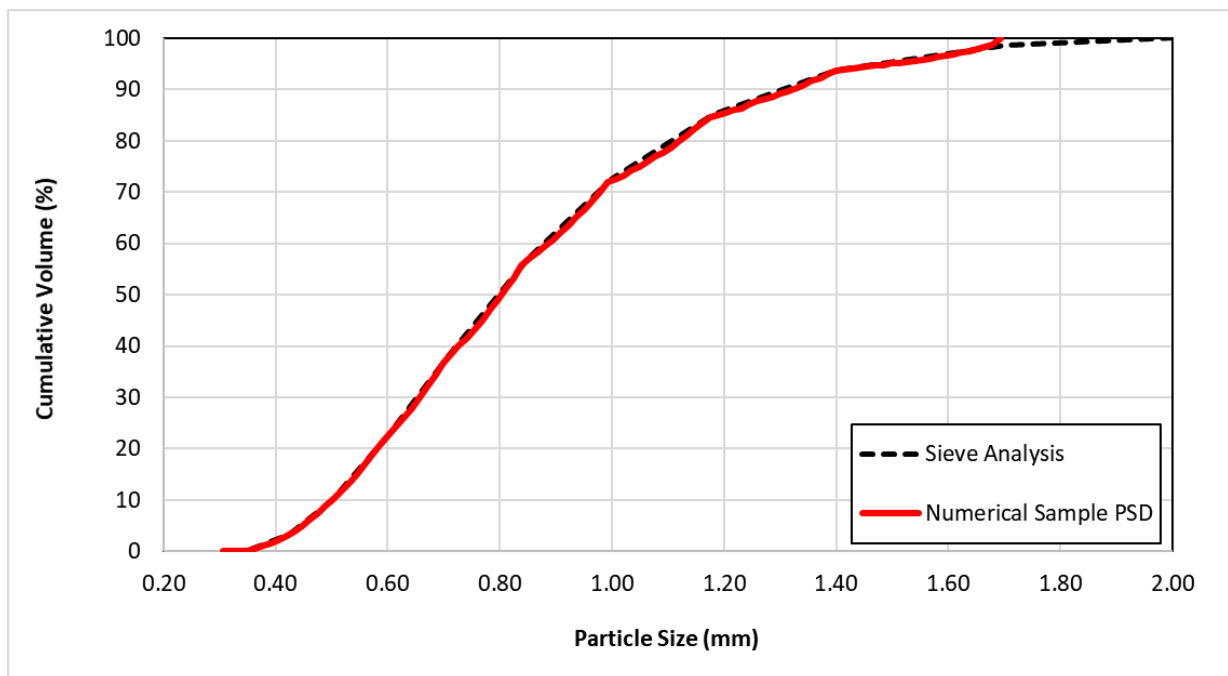


Figure 4-9 Particle Size Distribution (PSD) of the numerical synthetic model

For the erosion tests, very soft synthetic samples were required that were created by using a low cement to sand ratio. Only one set of Rock Scratch Tests were conducted on these samples, which showed their uni-axial compressive strength was 1.5 MPa (Bayati, 2018).

4.3) Numerical samples

The first step of a DEM numerical modelling is to create a representative numerical sample that honours the observations at the micro-level and matches the measured macro-properties. It starts with generating a packed assembly of particles, with a given particle size distribution and contact type.

During the course of this research, multiple versions of numerical rock samples were generated for rock scratch testing. All the samples were based on natural sandstones. The simulations of the preliminary 2D study, as will be explained in Chapter 5, were based on Berea sandstone. All the remaining simulations were performed on numerical samples based on Bentheimer properties.

In the early stages of this research, only a simple calibration process was followed to match the stress-strain curves. This is the technique that is used by many authors in RST simulation, as covered in Chapter 3. The final calibration, however, was more comprehensive and included matching the tensile strength and failure envelope. While the micro-properties of each sample will be listed, only the final calibrated properties and sensitivities will be provided to avoid repetition. These rock modelling efforts led to a new calibration method that reduces the number of trial and errors in achieving the desired properties. This will be explained in the following sections. A summary of different generations of numerical samples, prepared for RST simulation, is listed in Table 4-4. A code is assigned to each sample for referencing purposes.

Table 4-4 Summary of the numerical samples used for RST simulation

Code	Description	Sandstone type	Grain Size	Contact Model	Properties matched
EXP2D	Exploratory 2D	Berea	0.4-0.64mm	PBM	UCS, E and ν
Int3DBall	Intermediate 3D (ball)	Bentheimer	0.31-0.47mm	PBM	UCS, E and ν
Int3DClump	Intermediate 3D (Clump)	Bentheimer	0.31-0.47mm	PBM	UCS, E and ν
FNL3D	Final 3D	Bentheimer	PSD Matched	FJM	UCS, E , ν , Tensile Strength, C and ϕ

4.3.1 Test Procedure

The macro-properties of a numerical sample are measured by simulating the physical tests and recording the rock response under the applied stresses. The techniques for simulating these tests and measuring the responses are extremely important. Poor test modelling, or a poor measurement method, will cause an error in the calibration process. The following is a brief explanation of the test procedures, which are used for measuring the rock properties.

The UCS test was simulated on a cylindrical core sample with the same dimensions as those used in the laboratory tests: 1.5” in diameter and 3” in height. Two rigid walls were created at two ends of the sample, initially just touching the sample, without applying any axial stress. This was done by identifying the farthest balls at the top and bottom of the sample and setting the wall positions to be tangent to these balls. This causes a small gap between the walls and the main surface of the sample. The model set up is shown in Figure 4-10.

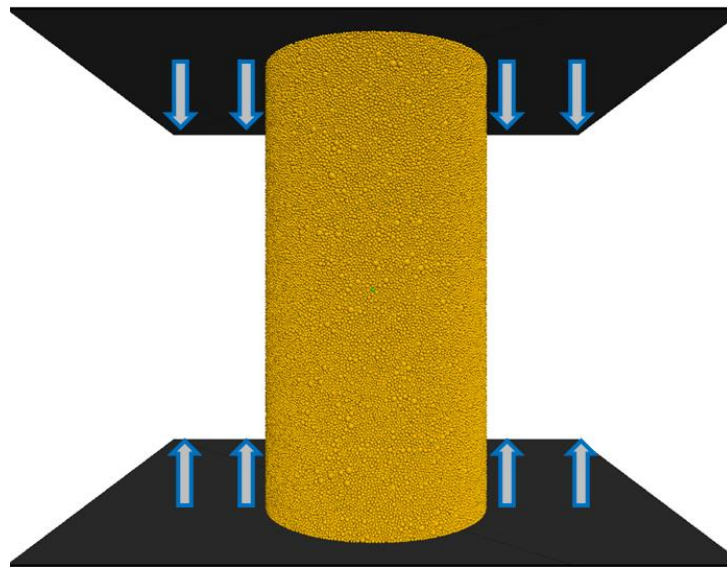


Figure 4-10 UCS test simulation set up.

The stress was applied by moving the servo walls with a constant strain rate and recording the resultant forces. The axial stress was calculated and recorded for each time-step. Because of the gap between the walls and the main sample surface at the start of the simulation, it is not possible to use the wall location to accurately calculate the axial strain. Two approaches were used here for strain measurement, with almost identical results. In the first method, a measurement sphere was created inside the sample to record the strain rate, that subsequently was used to calculate the strain at each time-step. The second method utilised the location of several balls, called Sensor Balls, to track the sample deformation in the axial and radial directions. The set-ups of both methods are shown in Figure 4-11.

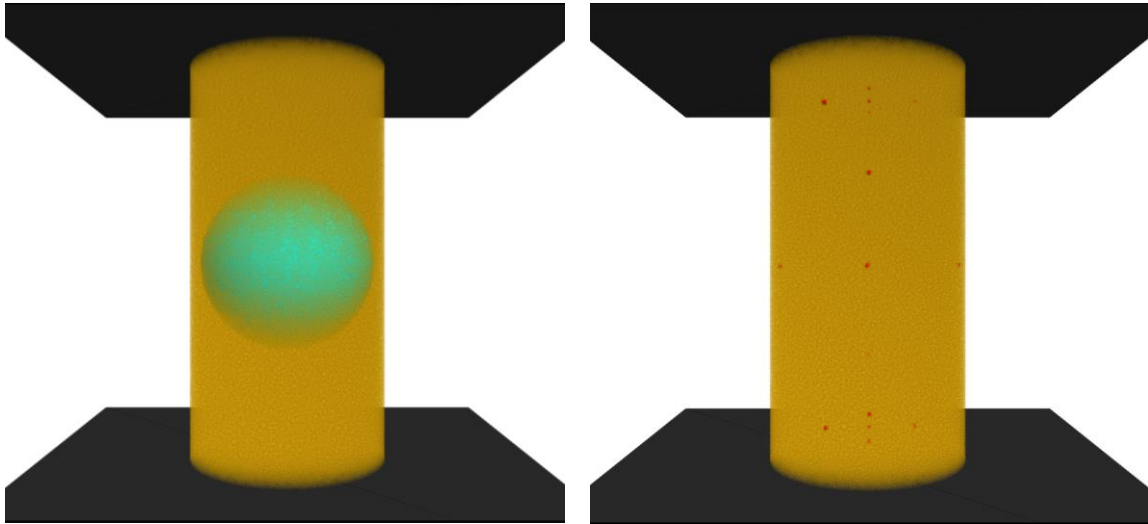


Figure 4-11 Strain measurement methods: Left: Measurement Sphere shown in Blue; Right: Sensor Balls, shown as small red spheres.

The **tensile strength** can be measured using a direct tension test (Figure 4-12). A constant strain rate was specified and applied by two thin layers located at the top and bottom of the sample. The stress was measured inside the measurement sphere and recorded at each time-step. The maximum value is the tensile strength of the sample.



Figure 4-12 Direct tension test set-up.

As argued by Wang and Tonon (2009), using rigid walls around the sample prevents natural deformation. It was mentioned in Chapter 4 that the method proposed by Wang and Tonon (2009) to conduct confined tests is likely to cause local stress concentration. To overcome this issue, a new method was developed here that uses a layer of smaller balls, packed around the sample, to apply the confined stress (Figure 4-13). The balls insert a constant force, the direction of which is updated every

time-step to ensure it is in the radial direction. The balls are smaller than the average sample grain size and apply a uniform stress, which can be measured and recorded by the measurement sphere.

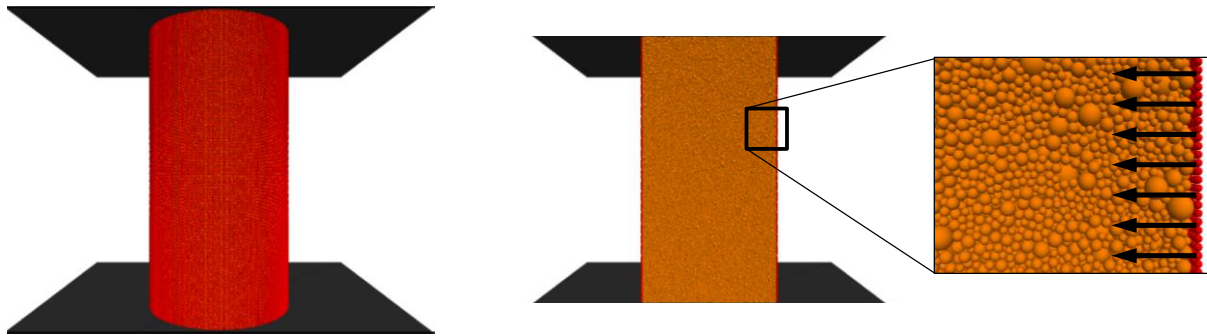


Figure 4-13 Generating an outer layer for applying confined stress. Left: Confined test set-up; Right: Cross-section of the model showing the outer layer.

4.3.2 Early Samples

The early samples include EXP2D, Int3DBall and Int3DClump, as listed in Table 4-4. They were only calibrated to match the stress-strain curves obtained from laboratory UCS tests. The particles were generated with the specified minimum and maximum radii and bonded by a parallel-bond contact model. Only the final calibration process, as applied on the final FNL3D samples, will be explained in this chapter and the details of the simple calibration method (PFC3D Manual, 2014) will not be repeated. The micro and macro-properties of these samples can be found in Appendix A. Figure 4-14 shows the Int3DBall and Int3DClump samples. Note the clump types in Int3DClump, which were designed to qualitatively match the grain shapes observed in the microscopic pictures (Figure 4-1).

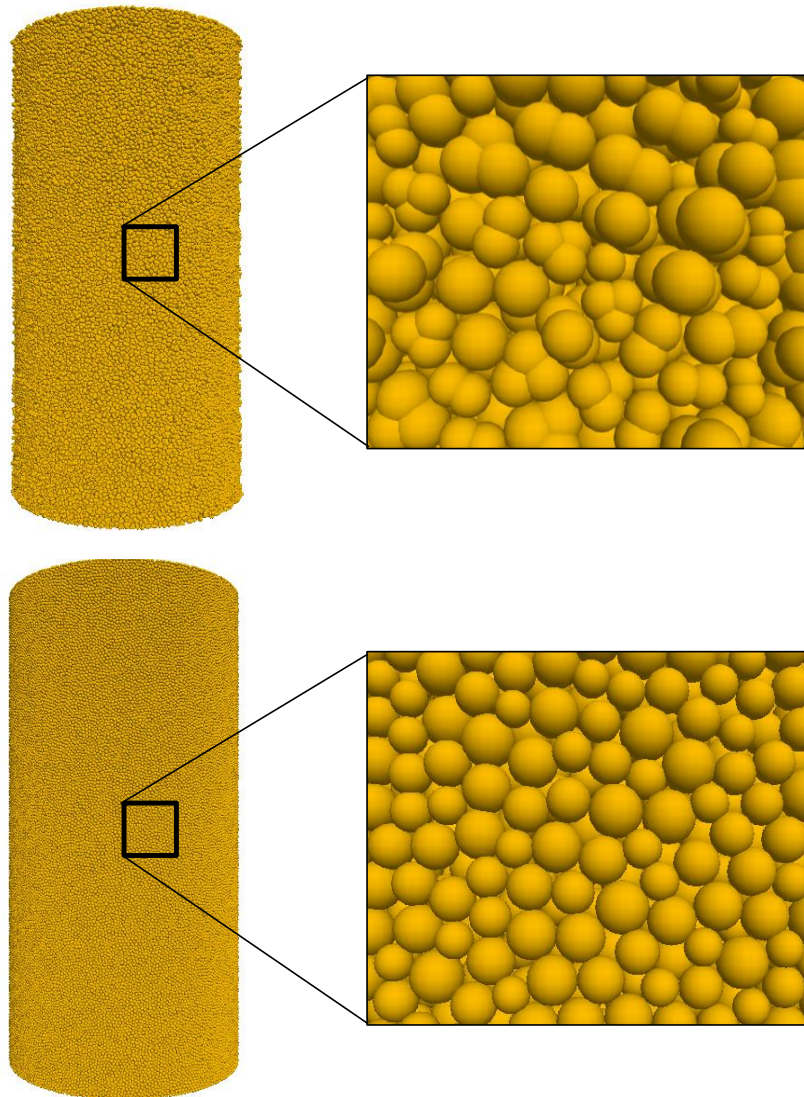


Figure 4-14 Top: Int3DClump; Bottom: Int3DBall.

4.3.3 Calibration Procedure

Calibration refers to adjusting the system properties to obtain the same measurements in the simulation tests as those obtained in the laboratory. It is the most critical part of a DEM simulation, as running a simulation on a poorly calibrated model can result in an unpredictable and erroneous behaviour. This section explains the steps involved in selecting the model properties. The generated samples were tested using the methods explained in the previous section.

The first step is to decide on the particle size. There have been several studies in the literature to explain the scale effect on DEM modelling results, however limited references were found regarding size effect in RST modelling. In this study, this will be addressed by running sensitivities on the particle size. To

minimize the particle size effect on the modelling results and conclusions, it will be attempted to use the models with particles as close to the real grain sizes as possible.

Apart from the direct impact on the results, the particle size also dictates the hardware requirements and simulation time. Using some examples from the current study may help to clarify the point: The particle size distribution of Bentheimer sandstone is presented in Figure 4-9. To reduce the number of particles and increase the time-step, the smallest 8% were ignored and replaced with particles of 0.2mm in diameter. Even with this simplification, 5.6 million particles were required to build a standard core cylinder of 1.5” in diameter and 3” in size. A relatively powerful PC (Table 3-1) was unable to run this model because of the large RAM requirements. To resolve this issue, further coarsening was necessary. After trying several coarsening techniques, the best method was found to be the use of a radius multiplier to increase the particle sizes in all the size bins. This ensured a constant particle size ratio and a consistent PSD curve shape. The finest model that the specified PC could run had a Coarsening Factor (CF) of 1.4, which consisted of 2.5 million particles. Simulating the UCS test of this model required 32 GB of RAM and was completed in approximately 4 days for a FJM and 1.5 days for a PBM. It is clear that using this model for the trial and error stage of calibration was not practical. For this reason, different samples, with different CFs were generated. Based on the observations, increasing the CF up to 3 did not change the rock behaviour significantly; hence, the CF3 samples were selected as the base case for calibration. It consisted of 260,000 particles and required approximately 6 hours for the UCS modelling. The expectation was once this model was calibrated, refining the model would not change the macro-properties significantly. Figure 4-15 shows the different sample resolutions. The number of particles in each sample is listed in Table 4-5.

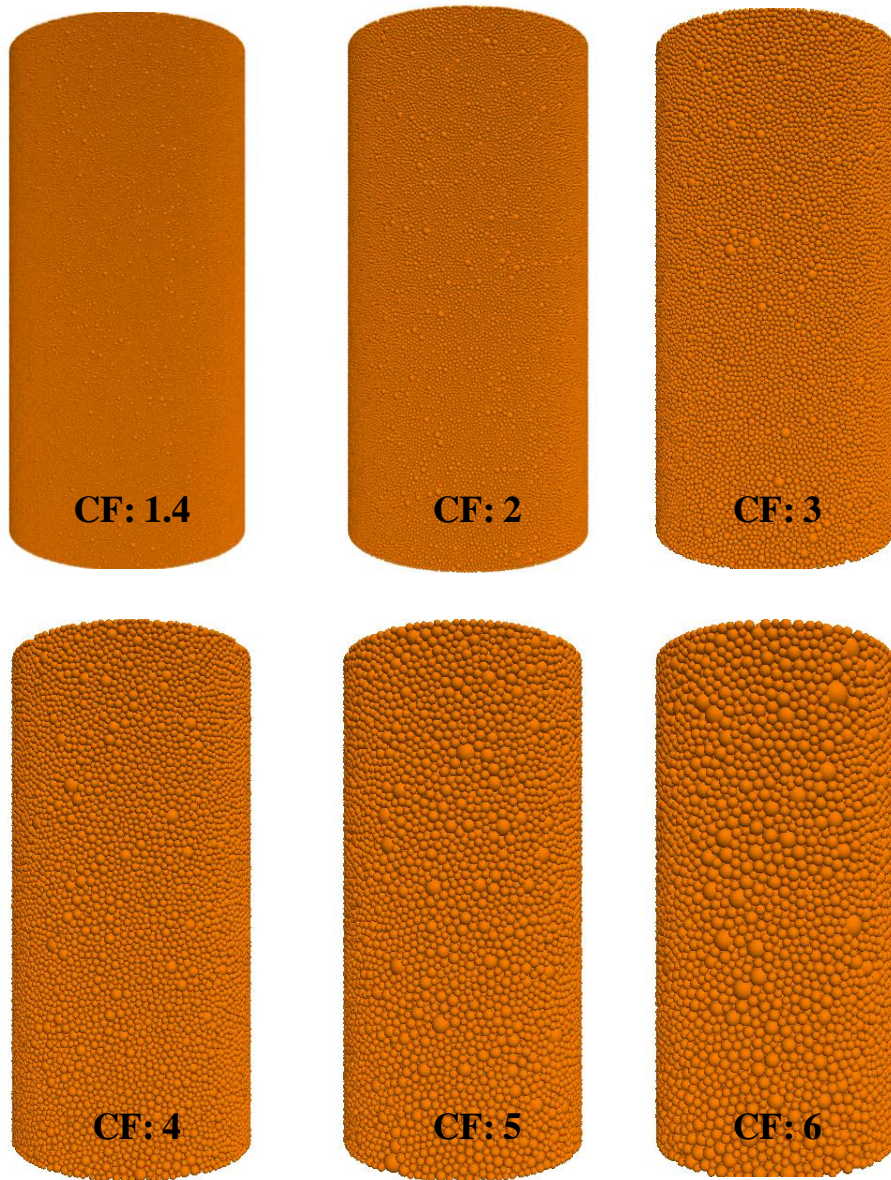


Figure 4-15 Different sample resolutions as a result of different Coarsening Factors.

Table 4-5 Coarsening Factor versus the number of particles required for building a standard 1.5" core sample.

Coarsening Factor	Number of particles required to build a 1.5×3" core sample
1	5,600,000
1.4	2,500,000
2	863,000
3	258,000
4	110,000
5	57,000
6	33,000

Once the particle size and its distribution are selected, a contact model should be chosen to bind the individual particles. If an improper contact model is chosen, it may not be possible to calibrate it to achieve the desired rock behaviour. A linear model, for example, is suitable for point contacts, similar to the touching points of perfectly spherical glass beads. It resembles an unbound state, so it is not possible to model a cemented rock using this model. However, it is a good choice for modelling the contact points of balls and walls, or the loose particles detached from the rock sample.

The parallel-bond model, on the other hand, shows acceptable results in modelling a bound rock. It is computationally efficient and can be used in applications where the goal is to match the basic elastic properties (i.e. UCS, E and ν). This model is not suitable for cases where a more comprehensive response calibration is required. It was explained in Chapter 2 that one of the main limitations of this model is that it is incapable of yielding a realistic uniaxial compressive to tensile strength ratio (UCS/ T). It has been explained by several authors (Chapter 2) that this is caused due to a lack of sufficient moment transfer. This can be overcome by adding some degree of interlocking to the system, by using clumps. While the use of clumps can be helpful in calibrating the tensile strength, it increases the particle numbers (each clump is composed of several balls) and the required calculations. This, in turn, results in significantly longer computer run times.

The flat-joint model is designed to overcome the restrictions of the simpler contact models. It “artificially” converts round particles to faced grains, which can provide interlocking and moment transfer. FJM is best suited for modelling rocks and is able to match the UCS/ T ratio. Each FJM contact consists of smaller elements. Before calibration, the number of elements in radial and circumferential directions must be selected. It should be noted that a higher number of elements requires more calculations and will result in longer run times. To investigate the effect of element number on rock behaviour, a simple model was generated and underwent the UCS test (Figure 4-16). The particle size of the samples was 0.8 to 1.6 mm. It must be emphasized that this sensitivity was done before the final calibration and the sample properties are different than those of the final sample. Where the installation gap is not specified, it is set to zero (contacts only installed between the touching particles). Adding the installation gap establishes a flat-joint contact between the particles that are not in touch, however are in close proximity. Increasing the installation gap increases the UCS, E and causes a more brittle behaviour. A higher installation gap also increases the number of contacts in the system, which in turn increases the coordination number (number of contacts per particle). A higher coordination number is known to increase UCS/ T ratio and reduce Hoek-Brown strength parameter m_i . The gap value cannot be more than the diameter of the smallest particle size, otherwise the contacts can “bridge” the particles, which is not physical. When calibrating models of different coarsening factors, the ratio of the installation gap to the minimum particle size should be kept constant.

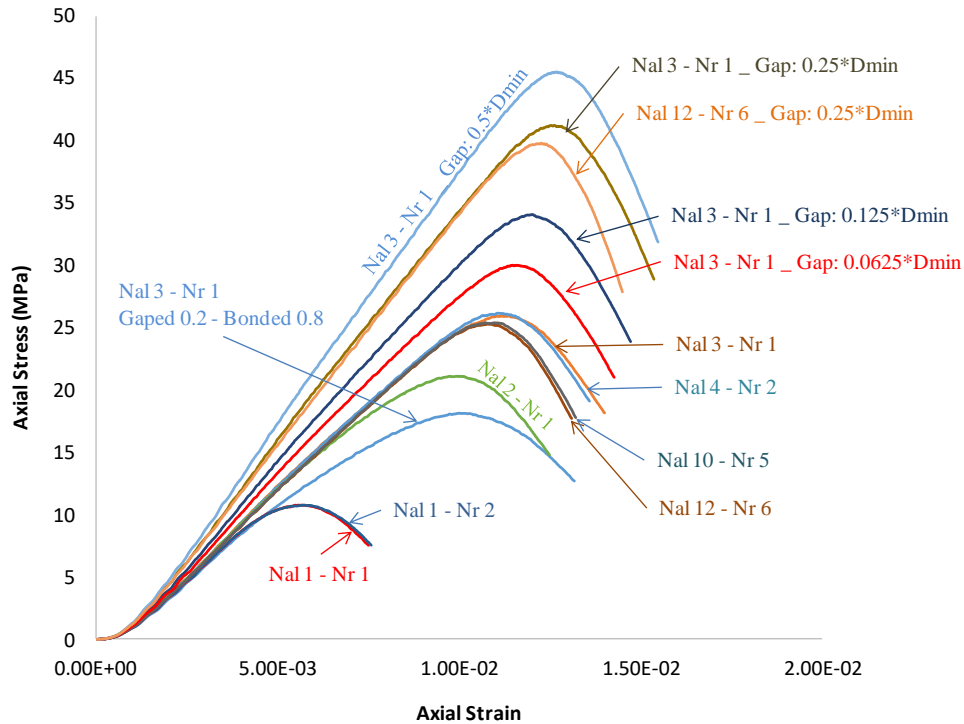


Figure 4-16 Effect of FJM element number on stress-strain curve.

Investigation of the curves shows that above “Nal 3 – Nr 1” the curve shape does not change significantly. It also shows that the curves related to contacts with a lesser number of elements show a more ductile behaviour, which is not a characteristic of the Bentheimer sandstone. For these reasons, in the final calibration, the values of Nal and Nr were set to 3 and 1, respectively.

Several calibration methods were covered in Chapter 2. Testing of these methods revealed that the procedure proposed by Wu and Xu (2016) is more efficient because of the lower number of trial and error tests required to reach the final calibration. It was also noted that there are few parameters affecting the rock behaviour which were not covered by Wu and Xu (2016).

Based on the observations and the sensitivity studies performed during the numerical modelling of the current study, a new method is proposed to further enhance the calibration process. It is aimed at reducing the number of trial and errors and the required time for calibration. The process is shown in Figure 4-17 and described below:

1. Decide on the sample resolution (particle size) and damping factor. The particle size selection requires a sensitivity analysis and depends heavily on the final application that the sample will be used for. This matter will be discussed in more detail in Chapter 5, however an example may assist in clarifying the concept. It was explained in Chapter 3 that the model scale is expressed in L/D . In the case of a rock scratch test, L can be considered as the depth of cut, or the cutter width. There is a

minimum number of particles required to be in contact with the cutter to make a stable simulation. This implies that the particle size should be kept smaller than a certain size. In this research, due to the extremely small depth of cut (0.25-4 mm), the actual Bentheimer grain size was used in the simulation. In other applications, where the characteristic model length is larger, the model scale is less important and larger particles can be used.

2. Select contact type and contact geometry parameters, as explained above and in Figure 4-16.
3. Build a much coarser model for initial first-pass calibration. The coarse model (e.g. CF6) should run in a few minutes and the intent is to assist in selecting the range of the properties, not fine tuning. The reason for doing so is that each micro-property will affect more than one macro-property. Wu and Xu's method calls for tuning the elastic properties at the last stage of the calibration. If this stage (running the coarse model) is not done prior to the calibration of the post-peak behaviour, tuning the elastic properties at the end may require large changes in the micro-properties, which is more likely to disturb the calibration done in the previous steps. This step ensures the adjustments required in the next stages of calibration are as small as possible. For this reason, it is likely to save significant time and effort by reducing the number of trials and errors in calibrating the actual (finer) model. In this step, using the coarse model, the UCS/ T , UCS, E and ν are qualitatively calibrated.
4. Use the sample with the particle size selected in step 1 and proceed with the calibration process by calibrating the properties in the order shown in the Figure 4-17. This step is very similar to the method proposed by Wu and Xu (2016), except matching of the internal friction angle, which is calibrated by FJM friction angle, as well as FJM friction coefficient.
5. The last step is testing the rock behaviour in the final application. If the rock does not behave as expected, the underlying assumptions should be amended. This includes changing the fraction of the bonded contacts, damping factor and the default contact model. Once this step is done, repeating Steps 3 and 4 may be necessary to ensure the macro properties are in the desired range.

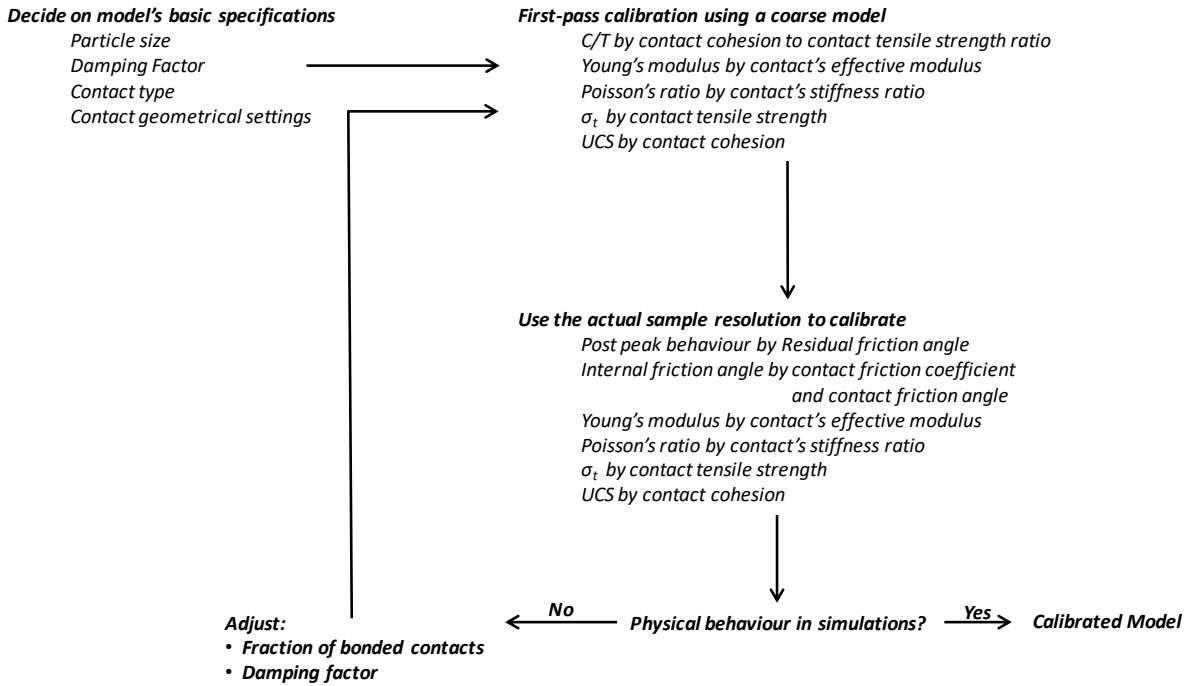


Figure 4-17 Proposed calibration process.

As previously explained, a CF of 3 was selected for fine tuning the model. The final micro-properties used to achieve the calibration of this sample, called FNL3D-A, are listed in Appendix 1. In this model all the contacts were initially bonded, which is equivalent to a sample with zero pre-existing cracks. A comparison of the simulated UCS tests versus the experimental test results is shown in Figure 4-18.

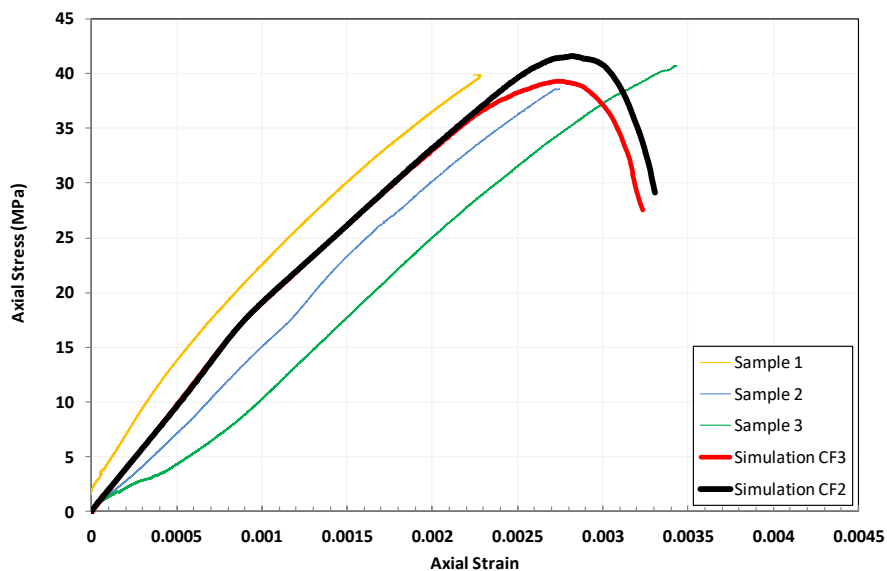


Figure 4-18 Stress-strain curves obtained from experiments versus the simulation results.

The model scale sensitivities were conducted by changing the CF from 6 to a minimum of 1.4. Due to hardware and processing time limitations, it was not possible to reduce the CF below 1.4. A comparison of the stress-strain curves obtained for the calibrated model is shown in Figure 4-19.

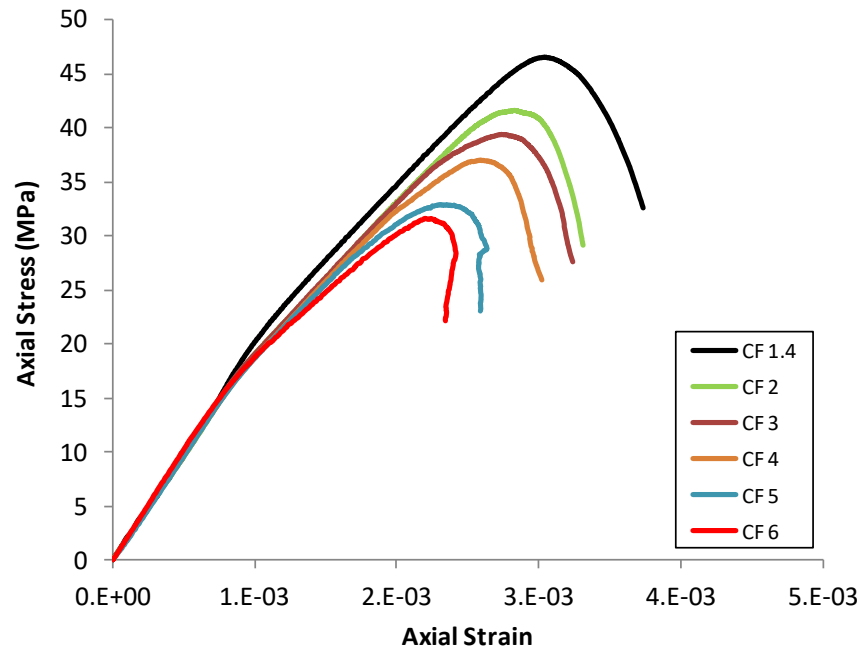


Figure 4-19 Size sensitivity on FNL samples (Damping Factor 0.7).

The failure envelope parameters of each sample were defined by conducting confined tests. Table 4-6 summarizes the properties of the FNL3D-A sample with different coarsening factors. The stress unit is MPa throughout this thesis.

Table 4-6 Model scale effect on macro properties

Sample	CF	UCS	E	v	Tensile Strength	UCS/T	C	ϕ
FNL3D-A-1.4	1.4	44.48	13.34	0.22	2.17	20.5	41.8	9.51
FNL3D-A-2	2	41.65	14.68	0.23	2.21	18.8	42.4	8.91
FNL3D-A-3	3	39.3	14.9	0.23	2.34	16.8	42.8	8.58
FNL3D-A-4	4	37.03	15.4	0.193	2.36	15.7	43.16	8.02
FNL3D-A-5	5	32.9	16.5	0.15	2.44	13.5	44.58	6.88
FNL3D-A-6	6	31.64	16.3	0.14	2.47	12.8	44.62	6.6

Since most of the simulations will be run on the sample with the actual grain size distribution (CF1), it is necessary to estimate the properties of this sample from the trend observed from the coarser samples. Fortunately, a strong linear trend exists in most of the obtained numbers, suggesting a reliable estimate. The trends are shown in Figure 4-20.

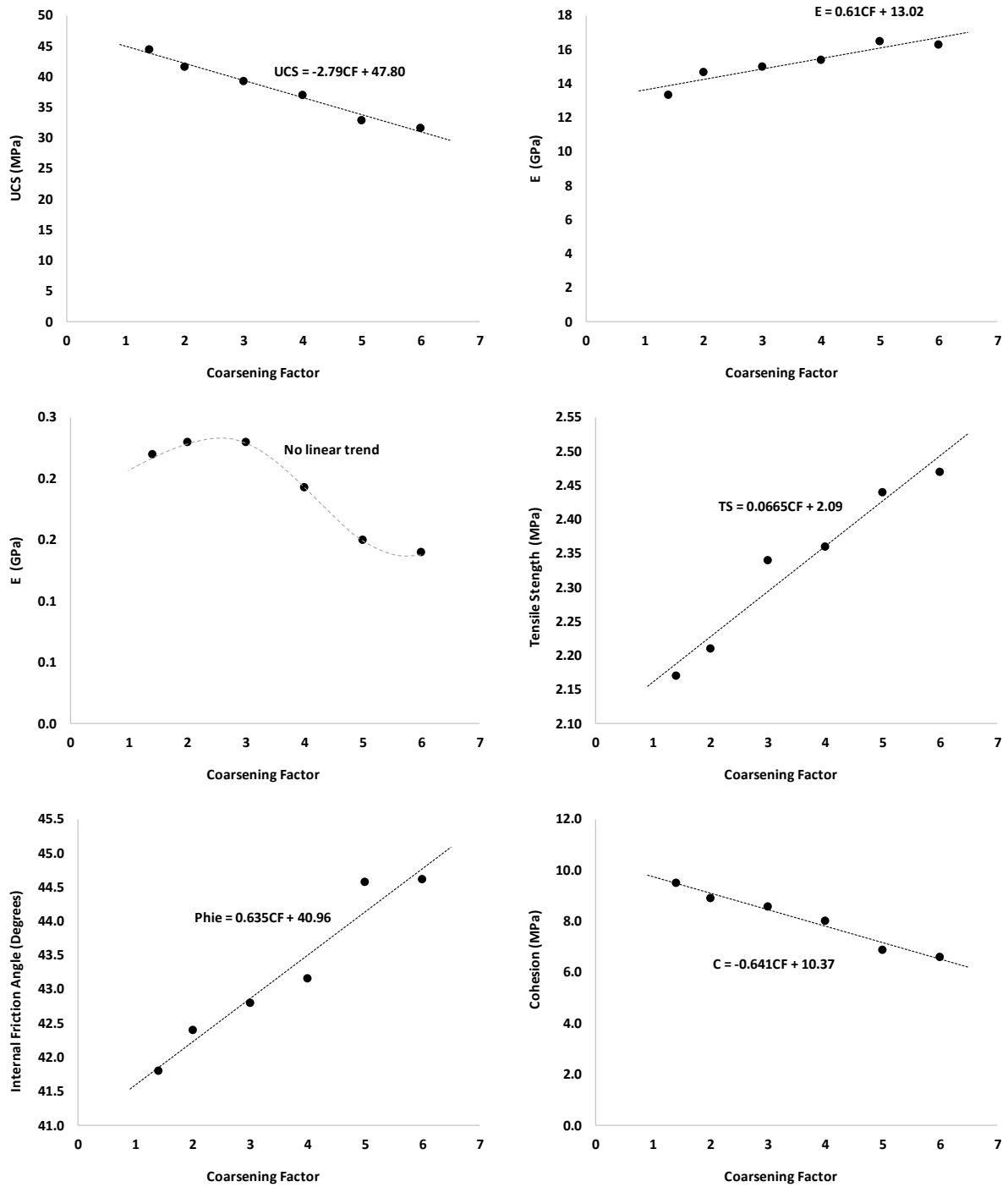


Figure 4-20 Model scale effect on macro-properties.

The properties of FNL3D-A-1, as a result of the extrapolations above, are shown in Table 4-7.

Table 4-7 Properties of FNL3D-A-1

Sample	CF	UCS MPa	E GPa	ν	Tensile Strength MPa	UCS/T	ϕ	C
FNL3D-A-1	1	45.01	13.63	0.215	2.2	20.3	41.5	9.7

The calibrated sample explained above is based on the assumption that all of the particles within $0.35D_{\min}$ are bonded by a flat-joint contact, which can be translated into the existence of cement bonds between all of the grains. A closer look at the microscopic picture of Bentheimer sandstone (Figure 4-1), however, shows that there are grain contacts which may not be bonded by cement. Considering the fact that the ultimate goal of this sample generation exercise is building a representative model to use in rock scratch test simulation, the unbound contacts should also be incorporated in the modelling. This was done by calibrating a second sample with 20% unbound contacts, modelled by Type-S flat-joint contact model, as explained in Chapter 2. The proportion of unbounded contacts was taken qualitatively from the microscopic image. Adding the Type-S contacts to the calibrated “A” sample explained above causes a substantial reduction of the rock strength and significantly affects the Young’s modulus and Poisson’s ratio. This necessitates re-adjustments of the micro-properties to obtain a match for the new sample. Of interest is the relative ease of re-calibration which only required increasing the tensile strength and cohesion of the FJ contacts, while keeping their ratio constant. A minor adjustment was also necessary on the effective modulus of the contacts to calibrate the Young’s modulus. The micro-properties of the new sample, called FNL3D-B, are summarized in Appendix-A. It should be noted that the “B” samples were generated after a feedback from the RST simulations (Chapter 5) that “A” samples may not produce the expected cutting response. As will be discussed in Chapter 5, the new sample shows considerably different behaviour in the RST simulation.

Again, based on the feedback from the RST simulations, two more samples were generated. Sample FNL3D-C was built by introducing 20% variance to the tensile and cohesion strength of the flat-joint contacts. This represents different cement qualities between the particles and introduces weak points to the sample, that may act as the nuclei for crack initiation. Re-adjustments were necessary to re-calibrate the properties of this sample.

In all the above samples, the existing contacts were defined as FJM. However, the new contacts, similar to the ones generated in front of the cutter in the crushed zone, were assumed to be linear. The RST results feedback necessitated some more refinement on the sample generation process. The last sample, called FNL3D-D, was built by assigning FJM to the new contacts, as well as the existing ones. This means the detached grains in front of the cutter will be treated as “faced” particles, capable of transmitting momentum. This proved to make a significant improvement on the RST response of the sample. The micro-properties of samples “C” and “D” are also listed in Appendix A.

Damping factor sensitivity

The samples explained above were built using a damping factor of 0.7. This was to ensure a quasi-static condition in the simulations. As described in Chapter 2, the only method of energy dissipation is through damping, while in the real rocks this happens due to grain/cement crushing. The value of 0.7 is widely used in the literature and is the default value for rock testing in Itasca’s documentation. The choice of

damping factor value is dependent on the nature of the application (refer to Table 2-1), however it should be noted that the damping magnitude affects the model behaviour. This will be discussed in more detail in Chapter 5, where samples of different damping ratios will be subjected to rock scratch testing. Figure 4-21 shows the effect of reducing the damping from 0.7 to 0.4 in the previously calibrated samples. The solid lines represent the damping of 0.7, while the dashed lines are generated by samples of the same properties, but a lower damping factor of 0.4. It is known that a lower damping factor results in more brittle behaviour.

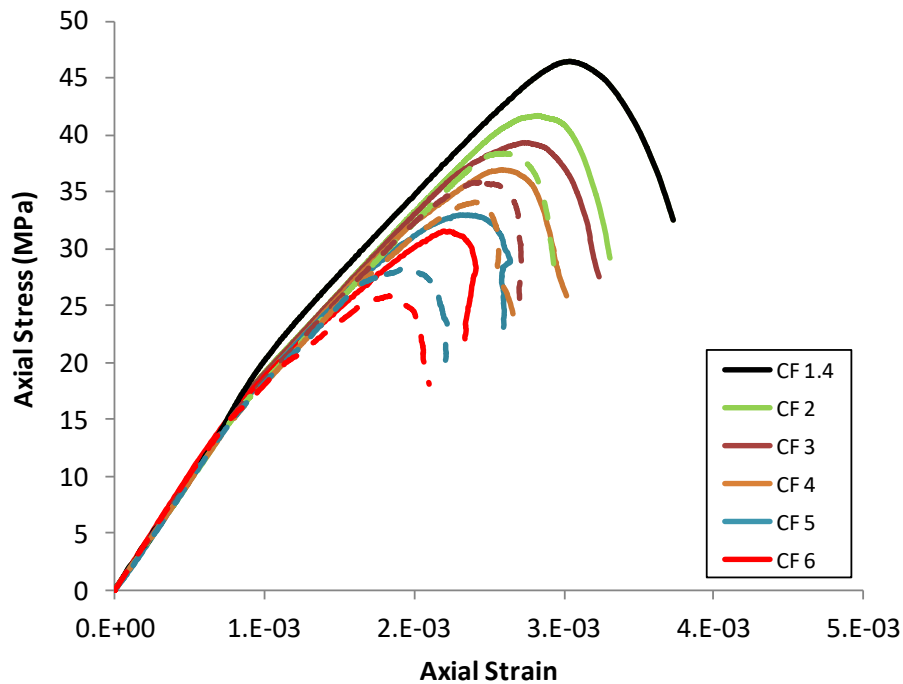


Figure 4-21 Damping effect on stress-strain curves. Solid lines: Damping Factor of 0.7; Dashed lines: Damping factor of 0.4.

4.4) Chapter Conclusions

This chapter explained properties of the physical and numerical samples used throughout this research. The experimental procedures for measuring the properties, as well as the equivalent numerical simulations, were described. A new method was developed for the numerical simulation of confined tests to enable “natural” deformation, instead of using the traditional rigid walls.

The sample calibration process proposed by Wu and Xu (2016) was modified to achieve the final result faster and more efficiently. Additional parameters were identified which were not addressed by Wu and Xu (2016). Four calibrated samples, with different pre-existing crack contents, cement strength homogeneity and default contact model, were built and calibrated. Size and damping sensitivities were

also conducted which will be used in the interpretation of the results obtained in Chapter 5. In general terms, the numerical samples:

- Use a realistic particle size distribution. Where a coarser sample was required, a Coarsening Factor was used to increase the particle sizes, while keeping the ratio constant.
- Closely match the UCS, Young's modulus, Poisson's ratio, tensile strength and failure envelope.
- Show a high degree of interlocking by using clumps and a flat-joint contact model. The microscopic pictures show the particles are tightly packed and well cemented. For this reason, the flat-joint model was defined with small portion of slit bonds. In clump samples, the gap was adjusted so that the neighbouring particles satisfactorily bond together (higher coordination number).

5 Rock Scratch Testing

The concept of Rock Scratch Testing (RST) was explained in Chapter 3 and a review of the available literature was presented. RST provides a basic controlled approach to study the rock-bit interaction at a single-cutter level. It is also considered an alternative method to measure the rock strength, due to the strong correlation between the rock's uniaxial strength and the Intrinsic Specific Energy (ISE) – i.e. the energy required to cut a unit volume of the rock sample. It was shown in Chapter 3 that the numerical modelling of RST has suffered from a lack of a comprehensive study to investigate the effect of sample calibration and cutting parameters on RST modelling in three dimensions. The motivation behind the current research was to use the recommendations from the literature to build a numerical sample, which sufficiently represents the properties of the physical rocks, and investigate the effect of different settings on the RST response.

The calibration process and the sensitivity studies of the parameters, including the average particle size, contact type and the selection of the micro-properties, were described in Chapter 4. To narrow down the unknowns, a single rock-type was used for the laboratory experiments, as well as the numerical calibration and RST simulation. The rationale was to make sure the numerical model settings are meaningful, so that the results can be validated against the well-known cutting response. This chapter will summarize the simulations performed as part of the current research to model the cutting action of a single cutter.

5.1) Model Set-up

Similar to the numerical modelling efforts explained in Chapter 4, the purpose of the simulations performed in this chapter are to build a numerical system which sufficiently represents the mechanics and results of the experimental tests. This was partly addressed in Chapter 4, where the rock sample was calibrated to produce the same response as measured experimentally. To model rock scratch tests, a cubic sample was generated with the same particle size distribution and contact properties as the cylindrical samples used in the calibration process, i.e. UCS, Brazilian and confined compressional tests. To minimize the unknowns and exclude the scale effects, the cubical samples were not coarsened ($CF=1$). This ensures that the particle size distribution closely matches those of the Bentheimer sandstone (Figure 4-3). To avoid modelling a sample which is unnecessarily large, the early simulation results on different sample sizes were investigated, which showed the results essentially remains the same beyond a certain cubic sample dimension. When using a cutter size up to 1cm, a conservative size to minimise boundary effects was found to be $[L]30 \times [W]24 \times [H]8$ mm (Figure 5-1). Although this is

much smaller than the sample used in the laboratory, more than 450,000 particles were required to build this relatively small sample.

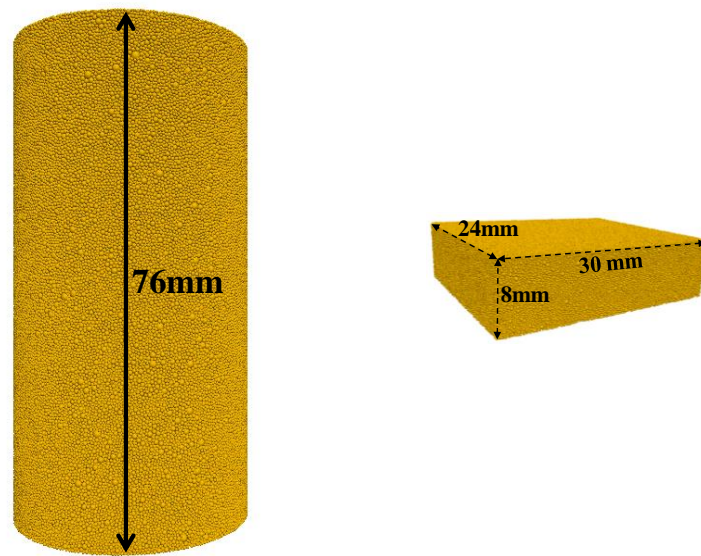


Figure 5-1 Left: Sample size used for UCS and confined tests; Right: Sample size used for RST tests

To further reduce the number of particles and the simulation time, coarser particles were used beyond a certain distance (3mm) away from the cutting groove, as proposed by Su and Akcin (2010). Given the results of the sensitivity analysis in Chapter 4 (Figure 4-19), the properties of the finer and coarser samples were different, however still close enough to be used in the edges, where no interaction with the cutter was expected. This reduced the number of particles to 143,000.

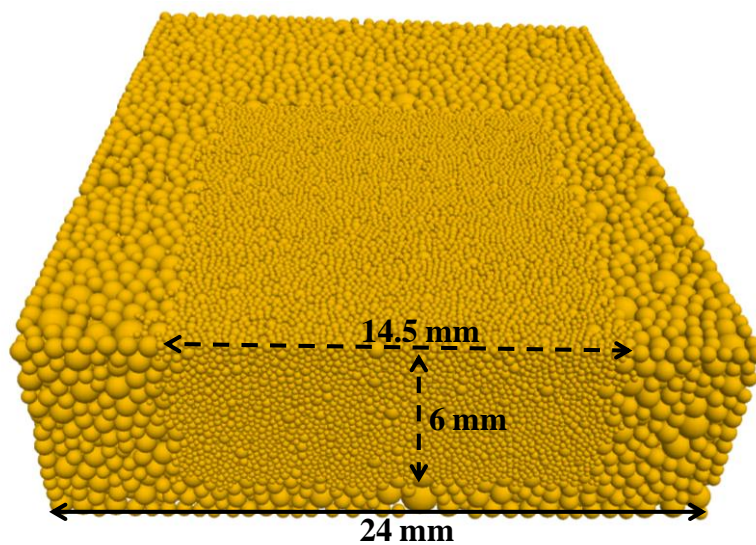


Figure 5-2 Using coarser particles around the cutting area

To perform the rock scratch test, the sample was contained by two walls, placed at the bottom and rear sides. A thin layer of particles at the bottom of the sample was fixed to stop movements in all directions. Observation of the early results revealed that these settings were sufficient to keep the sample stationary, while providing enough clearance to prevent the boundary effects. A cutter was built from rigid facets and placed at the finer end of the cubical sample. The location and orientation of the facets adjusted to generate the specified back-rake angle and depth of cut. At the initial state, the position of the cutter was set to just touch the rock sample, without applying any stresses. A constant speed was assigned to the cutter to move it along the length of the sample. All the other cutter velocity components were set to zero to prevent the cutter movements in the lateral and vertical directions. The RST simulation set-up is shown in Figure 5-3.

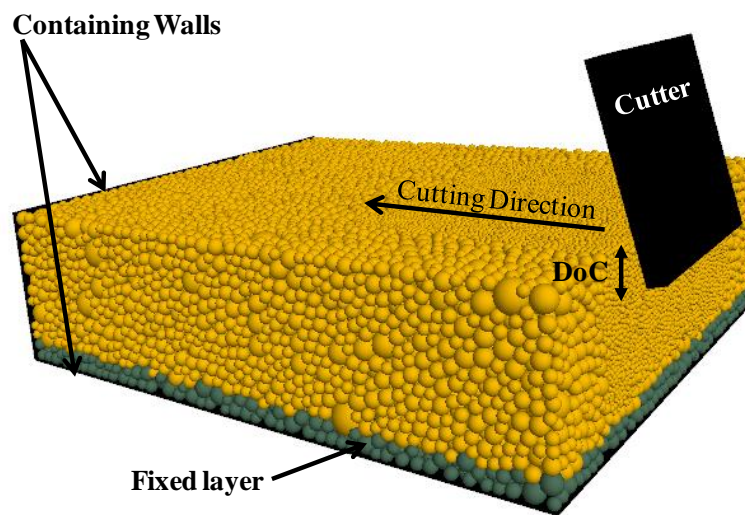


Figure 5-3 RST simulation set-up showing a deep cutting

It should be noted here that a minimum scratch length of 10 times the depth of cut ($10 \times \text{DoC}$) was recommended in the literature (Richard, 2012). For a shallow depth of cut ($< 1\text{mm}$), this can be honoured easily, however for a deeper DoC ($\sim 3\text{-}4\text{mm}$), it requires cutting the rock for 30-40mm, which significantly increases the computation time. For this reason, the length of cut for the fine models were restricted to 10mm. The average cutting force (or ISE) was calculated from the stable part of the curve in the second half of the cut.

5.2) Visual Investigations and Validation Criteria

The results of two dimensional (2D) and 3D simulations will be presented in the following sections. During the processing of the results, in addition to studying the recorded forces and stresses, the rock failure was also investigated visually to determine / confirm the chip formation and the extent of crack propagation in front of, and under the cutter. This was easy to perform 2D simulations, using the

software output snapshots (Refer to Figure 5-6). In three-dimensional simulations, however, due to the 3D extension of the sample and accumulation of detached particles in front of the cutter, it was not possible to easily identify the cracks. For this reason, the outputs were displayed in the form of cross-sections through the middle of the sample and the cutter, as demonstrated in Figure 5-4. The particles were shown as transparent circles, while the contacts were in the form of rods connecting the particles. The contacts were colour coded to differentiate between the status of the contacts, namely red (bonded, intact), blue (slit, pre-existing cracks), green (failed, tensile) and yellow (failed, shear). Several chips are visible in front of the cutter in the sample cross-section shown in Figure 5-4.

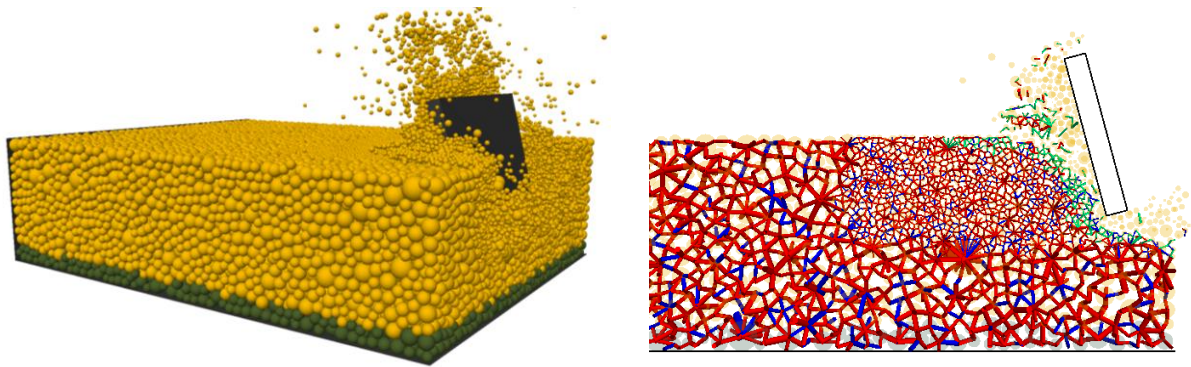


Figure 5-4 Graphical representation of deep cutting results in 3D simulations. Left: Full 3D; Right: Cross-section through 3D model

In fact, this technique was part of the validation criteria, which was established based on the observations from numerous references described in Chapter 3. After each scratch test, the following analyses were performed to compare the obtained results against the experimental observations:

1. Cutting mode: ductile or brittle, identified from the extent of crushing or chipping in front of the cutter, and to a lesser extent from the cutting force curve shape: white noise for ductile, and sawtooth shape for brittle mode.
2. Critical Depth of Cut: As explained in Figure 3-12, there is a critical depth of cut, beyond which the cutting mode changes from ductile to brittle.
3. ISE vs UCS: This is based on the extensive experimental simulations and literature review performed by Richard (2012), as demonstrated in Figure 3-10. The recorded cutting forces are converted to ISE and compared to UCS. The expectation is the ISE/UCS is close to unity.

5.3) Exploratory 2D Simulation

The main research was carried out in 3D, however to get familiarised with DEM modelling and explore the RST simulation, a brief 2D simulation was carried out. As explained in Chapter 4, to validate the results of the simulation, the laboratory results of Glowka (1989) were used, in which the scratch tests were performed by a 0.52in sharp cutter on Berea sandstone. The numerical model was generated using particle sizes of 0.4-0.64mm, which required approximately 30,000 particles to fill a standard 1.5×3” core sample. 2D DEM particles are in fact rods with a unit length, which implies the cutter also has a length of 1m. This is important when calculating the Intrinsic Specific Energy from the recorded cutting forces and the cut volume (DoC × Cutter Width).

The micro-properties of the numerical sample were calibrated to match UCS, Young’s Modulus and Poisson’s ratio of Berea sandstone. Because the parallel-bond model was used for bonding the particles, the sample’s tensile strength was over-estimated.

Table 5-1 Mechanical Properties of Berea Sandstone and those obtained from the exploratory PFC2D simulations

	UCS (MPa)	Elastic Modulus (GPa)	Poisson’s Ratio	Tensile Strength (MPa)
Laboratory (Glowka,1989)	49	14	0.36	3
PFC2D (Joodi et al., 2012)	48.8	14.3	0.366	11.6

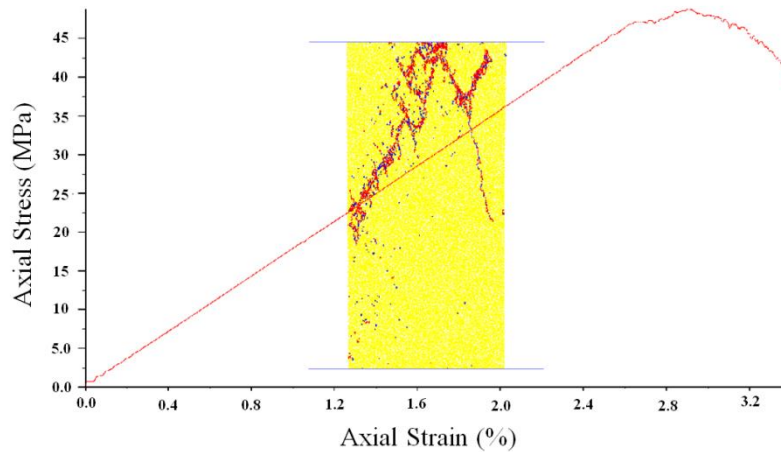


Figure 5-5 Results of the 2D UCS test simulation (Joodi et al., 2012)

Similar to Glowka’s (1989) laboratory tests, the simulated cutter was sharp, with a back-rake angle of 20°. Based on the feedback from the literature review on 2D simulations (Chapter 3), the cutter speed

was set to 2m/s, while the cutting speed in the laboratory was 5.6 cm/s. The speed sensitivity and further discussions related to the cutting speed will be discussed in detail in the 3D simulations.

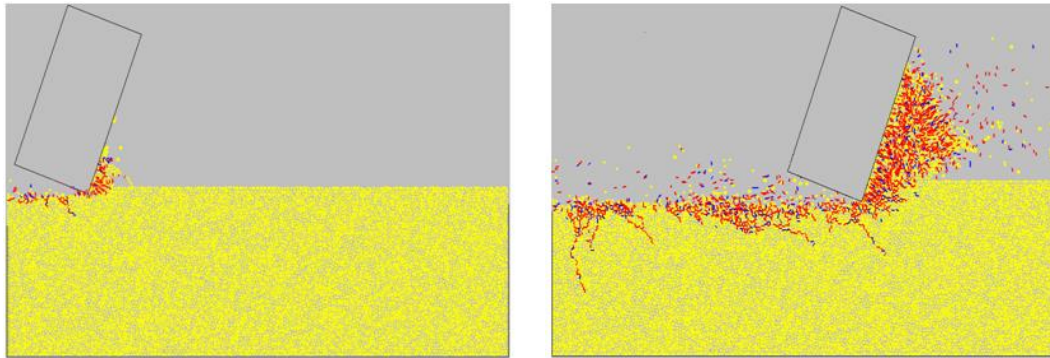


Figure 5-6 PFC2D cutting simulations. Left: Relatively shallow depth of cut (1mm); Right: Deep depth of cut (4mm) (Joodi et al., 2012)

The model output snapshots showed extensive cracking in front of, and below the cutter. The cracks propagated deeper in larger depths of cut, which agrees well with the expectations. A good agreement was observed between the recorded forces of shallow DoC with the laboratory measurements. In deeper cuts, the simulation results followed a linear increasing trend (Figure 5-7). Laboratory observations, however, showed beyond 1.5mm the data deviates from the straight-line trend, which can be explained by a change in the cutting mechanism: from ductile to brittle. One possible reason for the difference between the experimental and numerical results can be a lack of enough chipping in front of the cutter. In other words, the rock appears to undergo a substantial plastic deformation, even at the deeper cuts, while a brittle chipping was expected.

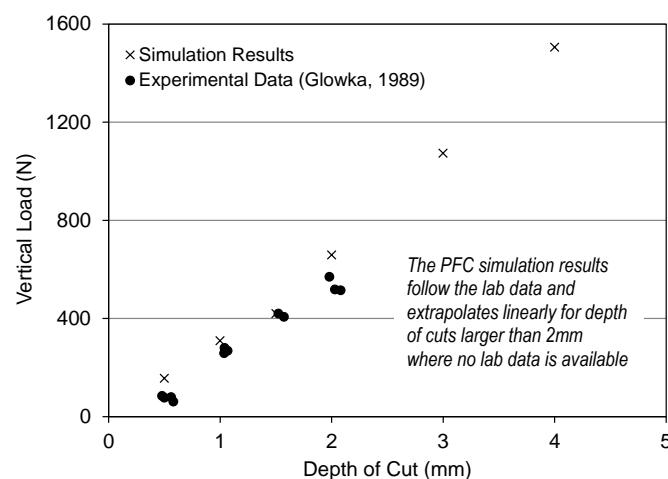


Figure 5-7 PFC2D cutting response for Berea Sandstone (Joodi et al., 2012 and Tulu and Heasley, 2009)

While the 2D results showed the potential of a DEM simulation to model rock cutting, especially at shallow depths of cut, a clear mismatch was identified between the laboratory results and the simulations, in terms of the cutting mode and the recorded forces in deeper cuts. Further refinement of the sample calibration and sensitivities of micro-properties and cutting settings were performed in 3D simulations, as discussed below.

5.4) 3D Simulations

The core part of this research, DEM simulation of RST (this chapter) as well as TWC and Erosion (Chapter 6), was performed in three dimensions. Itasca's Particle Flow Code in Three Dimensions (PFC3D) was used for the simulations. This package supports different contact models (refer to Chapter 2) and is able to perform parallel-processing. This is an extremely important feature in Discrete Element Method modelling, particularly in the case of the 3D applications, where the number of particles and their degrees of freedom are higher. 3D applications require significantly more computations in each time-step, which can be partially offset by using more powerful computers. Since the clock rate of the computers is limited, parallel processing is the only option in increasing the computing power and reducing the simulation time. A comparison of simulation time versus available processing cores was presented in Figure 2-13.

The 3D RST simulations of this study were started by modelling the scratch tests on samples built using the Parallel Bond Model. For referencing purposes, this step is called Intermediate Studies and the samples were named INT3D. The intention of performing this step of studies was to validate the RST simulation by seeking an analogy between the numerical results and the validation criteria explained previously in Visual Investigations and Validation Criteria. These include the correlation obtained by Richard (2012), as well as the crack propagation / chipping pattern. The INT3D samples were only calibrated to match the stress-strain curves obtained from the uniaxial compression tests. This is the approach used in most of the available literature (Chapter 3). Both spherical and non-spherical (clumps) particles were used to generate the INT3D samples. Details of the numerical samples were presented in Chapter 4.

Three sample types were generated for the intermediate studies, all based on the Bentheimer sandstone properties. INT3D-A1 and INT3D-A2 were built using balls and clumps, respectively, and were used to study the effect of cutting parameters on the recorded response. The properties of these samples are summarized in Table 5-2. The simple clump geometries used in A2 samples were selected to approximate the typical grain shapes observed in the microscopic pictures of Bentheimer Sandstone, as shown in Figure 4-1. The particle size in each case was 0.31-0.47mm, i.e. 30% larger than the measured Bentheimer grain diameter (Yaseri et al, 2014). The reason for this coarsening was to limit the number of particles to stay below 2 million, mainly dictated by the hardware limitations and simulation time.

Sample B1 was built using the same settings of A1, however using a lower K_n/K_s , to generate a rock type with different properties. This sample was used as a control group to confirm the findings of the A1 and A2 simulations.

Table 5-2 Properties of the three INT3D rock samples (Joodi, 2016)

Sample	Particle type	K_n/K_s	UCS (MPa)	E (GPa)
A-1	Spherical	1	34.2	11.9
A-2	Clumps	1	33.9	12.5
B-1	Spherical	0.2	22.4	16.6

A wide range was selected for the main cutting parameters, including DoC, Back-rake angle, cutting speed and cutter width. 98 RST cases were simulated on samples A1 and A2, using different combinations of the cutting parameters. Investigation of the results showed that when the cutting parameters are the same, there is no substantial difference in the normalized results (ISE/UCS) of the samples A1 and A2.

A sensitivity analysis was performed to investigate the effect of cutting speed on the average cutting force. While the expectation was the cutting forces to be almost independent of the cutter speed, the tests showed a strong linear relationship between the two parameters. Figure 5-8 shows the ISE values

obtained from scratch test modelling on A1 and A2 samples at different speeds and depths of cut. The trend is in agreement with the 2D simulation results of Rizo (2013).

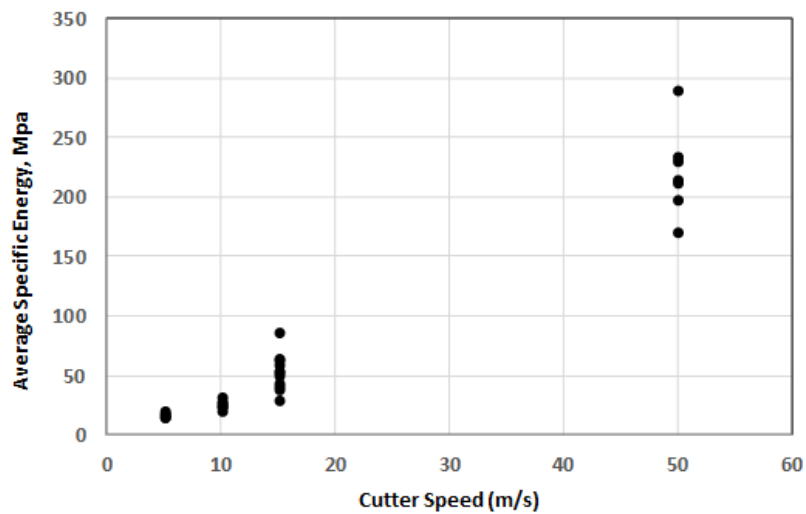


Figure 5-8 Average ISE obtained from different cutter speeds. BR angle:15°, DoC:0.44-4mm, Cutter Width:8 mm (Joodi, 2016).

All the intermediate simulations (98 cases) were investigated to compare the results with the validation criteria, i.e. crack propagation / chip formation, critical depth of cut and ISE/UCS ratio. For each of the cutting parameters, a suitable range was identified to yield an ISE/UCS ratio of close to unity. In each step, only one parameter was considered, and the data points were colour coded to exclude the range which always generated unacceptable results. A summary of the filtered data in each step is shown in Figure 5-9.

A review of the simulation snapshots demonstrated that the chipping in front of the cutter was minimal, and the ductile cutting mode extended much beyond the typical 1-2mm observed in the laboratory. A substantial crushing was observed at cutting depths as deep as 3mm. However, beyond DoC = 2mm the recorded data were highly scattered, without any clear trend. DoC needed to be constrained below 2mm to keep the reading stable. This is in agreement with the findings of the 2D model, which showed a ductile cutting in the 0.44-2mm region. Using a similar analysis, the back-rake angle should be limited to 15-25°, cutter width to more than 3mm, and the cutter speed to less than 10m/s.

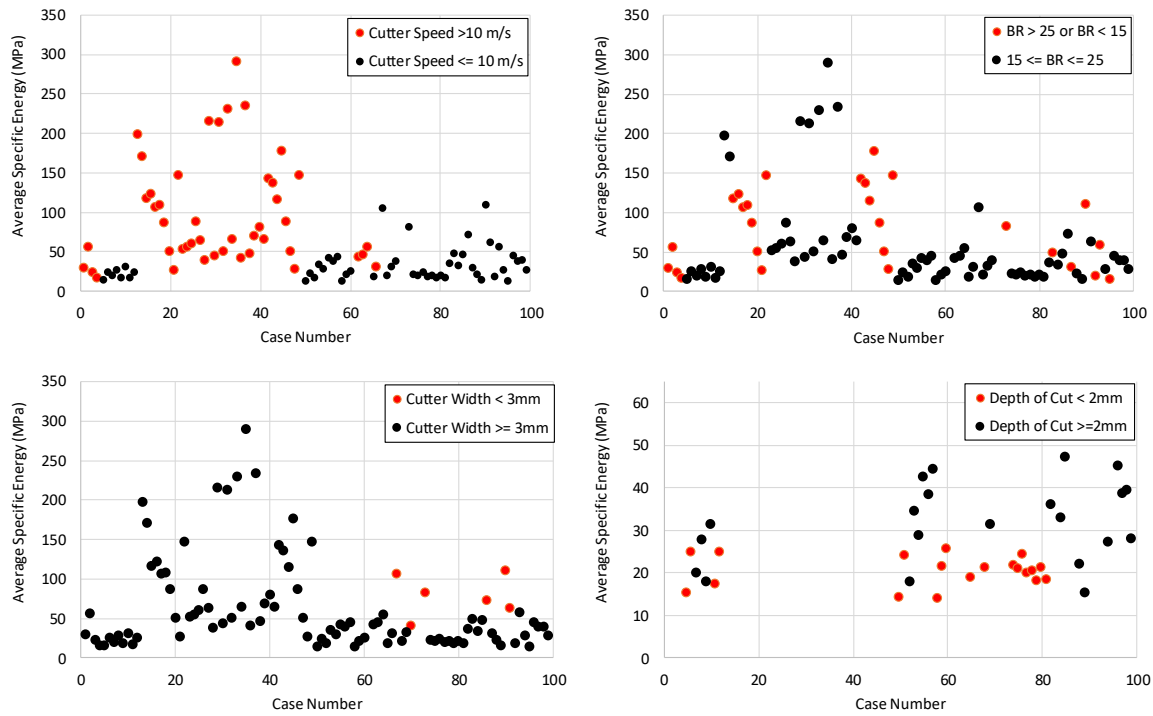


Figure 5-9 Colour coding of the cutting results based on the limiting criteria. Sample UCS is 34.2 MPa. Note the Scale of graphs (Joodi, 2016)

To confirm the findings, four scratch tests were performed on sample B1 (control rock type) by selecting the cutting parameters from the identified range. The results, as shown in Table 5-3, confirmed the ISE values were very close to the uniaxial compressive strength of 22.4 MPa. No improvements were observed in meeting the other validation criteria (cutting mode and chip formation in deeper DoC).

Table 5-3 Cutting results of Sample B-1 (Joodi, 2016)

Case No.	BR (°)	DoC (mm)	Cutter Speed (M/s)	Cutter Width (mm)	ISE (MPa)
1	25	1	10	8	25.74
2	25	2	5	8	24.88
3	15	1	10	8	20.38
4	15	2	10	8	27.34

The cutting results using the constrained values confirmed that it is possible to perform rock scratch tests under controlled conditions (specific combination of cutting parameters) to generate ISE close to the rock’s UCS. With regard to the UCS to ISE comparison, it must be emphasised here that the difference between the two values is not entirely related to RST method’s suitability to estimate UCS. Even the conventional compression test results are subject to some variation, both in the laboratory

experiments (due to rock heterogeneity, set-up and measurement accuracy) and the numerical simulations (random packing of the particles). Figure 5-10 shows an example, where the conventional UCS test is repeated on a simple numerical sample by only changing the random seed number (different particle packing). The captured deviation is $\pm 4\%$ of the average.

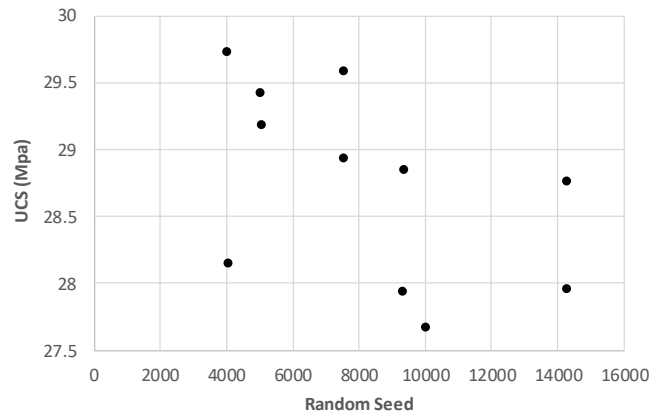


Figure 5-10 Dispersion of UCS data as a result of different random seed in sample generation (Joodi, 2016)

Discussion on Intermediate Simulation results

The 2D and intermediate 3D RST simulations, both performed on simple PBM numerical rock samples showed that under specific conditions, especially a certain cutting speed, it is possible to obtain an ISE close to UCS. This is the method used in all the publications reviewed by the author. The typical cutting speed used in the literature is 2m/s for 2D and 5m/s for 3D RST simulations. It could be concluded that the DEM modelling of the RST, using the PBM samples, can conditionally meet the first validation criterion: Under a specific combination of cutting parameters, the cutting response in the ductile cutting mode is in agreement with the observations of Richard et al. (2012). This limitation is rarely referenced in the literature (e.g. Rizo, 2013) and most authors have conveniently used a cutting speed and made a generalised conclusion that DEM is capable of capturing the rock-cutter interaction, both in predicting the cutting mode and cutting force.

The other observation of the *Intermediate Studies* results was the inconsistency in the critical depth of cut, which occurs much deeper in the numerical simulations. Investigation of the cutting mode revealed that under the ductile mode, the failure mainly happened due to plastic deformation and complete

crushing/separation of particles. This agrees well with the expectations. However, similar to the 2D results, the ductile region extends to much deeper DoCs.

RST on Flat-Joint Model Samples

To address the inconsistencies observed in the intermediate 3D studies and to refine the sample modelling, a new group of numerical samples were built to represent the mechanical behaviour of Bentheimer sandstone more accurately. For referencing, this step is called *Final Studies* and the samples were named FNL3D. Based on feedback from the literature review, FJM was selected for modelling the contacts. The sample generation process, as well as the performed sensitivities were explained in detail in Chapter 4. It should be noted here that at the time of building the intermediate INT3D samples, only one UCS experiment was performed. Further UCS and confined tests were conducted later which were consistent with the results of the first test, with minor differences. This caused some insignificant differences in the mechanical properties of the INT3D and FNL3D samples. Since the results were normalized before interpretation (ISE/UCS rather than the ISE), it is still possible to compare the Intermediate and Final results.

The main difference between the Intermediate and Final samples were in the ball-ball contact model. To investigate whether the abnormal behaviour observed in the cutting response of the Intermediate samples were related to the intact rock properties or the interaction of the detached grains in front of the cutter, initially FJM was only used for the existing contacts in the intact rock and linear contact model was assigned to all the new contacts in the detached grains. This implies that the intact rock particles had “skirted faces”, but the detached particles are modelled as spherical particles (Chapter 2). The evolution of the samples, as well as the cutting responses obtained for each sample, are summarised below.

- FNL3D-A: Uniform properties, all contacts were bonded, Existing Contacts: FJM, New Contacts: Linear Contact Model

It was explained in Chapter 4 that the FJM samples, contrary to the PBM samples, match the UCS/Tensile ratio of Bentheimer sandstone. This is the main difference in the properties of the INT3D and FNL3D samples. Following the methodology described earlier in Section 5.1), a cubic sample was generated with a Coarsening Factor of 1.0 in the cutting area, surrounded by coarser particles (CF = 3) and placed between two containing walls. The bottom layer was fixed in all directions to prevent movement of the sample. Based on the feedback from the *Intermediate Studies*, the back-rake angle was set to 15° and the cutting speed to 10 m/s. The back-rake angle of 15° was also consistent with Richard’s (2012) experiments, which were used as one of the validation criteria (ISE=UCS) in the current study. The measured forces were converted to the intrinsic specific energy, as plotted in Figure 5-11 for different depths of cut. Of interest was the value of ISE at DoC<1mm, ~42MPa, which

compared well with the UCS of this sample at 45.01 MPa. ISE remained constant for the cuts shallower than 1mm, however beyond this depth it started to increase. This contradicts the expectations that at larger DoCs, a change to the brittle mode should be observed, which is characterized by substantial chip formation and a drop in the observed ISE. Graphical investigation showed that even at higher DoC, there is almost no chipping in front of the cutter.

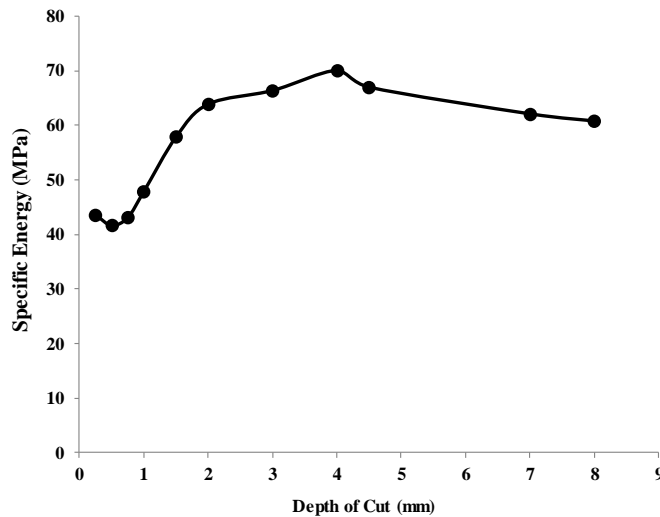


Figure 5-11 RST simulation results for sample FNL3D-A

To study the scale effect on the cutting response, the simulation runs were repeated for FNL3D-A sample with different coarsening factors (refer to Table 4-6). Knowing that the critical depth of cut is larger for coarser samples, the scratch tests were performed at DoC = 0.5, 1, 2 and 3 mm, as shown in Figure 5-12. Ideally, in the ductile region the ISE/UCS ratio should fall on the dotted unity line. Interestingly the data corresponding to the shallower DoC in the Coarsening Factor 1, 1.4 and 2 had the same ISE/UCS ratio, ~0.95, suggesting the cutter speed should have been marginally higher than 10m/s to get ISE/UCS = 1. Coarsening factors of 3 and 4 were also close, however showed different behaviour at deeper cuts.

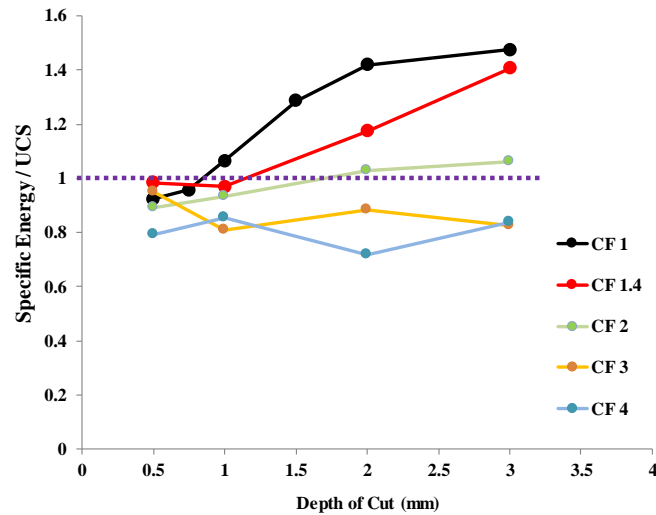


Figure 5-12 RST simulation results for different coarsening factors of Sample FNL3D-A

It is interesting to note the responses details of different cases. The CF5 (Coarsening Factor of 5) and CF6 cases were too coarse and there were not enough particles and contacts at the cutting area to produce a stable response. CF1, CF1.4 and CF2 essentially had the same response, although it can be seen that CF2 starts to increase at deeper DoC. This can be attributed to the size effect. In CF2, if all the geometrical settings including particle size and DoC were normalised with respect to grain size CF, the phenomenon that happens at a DoC of 2mm will be equivalent to DoC of 1mm in CF1. This can be confirmed by the behaviour of CF4 and CF3, which do not show any increase even at a DoC of 3mm. A DoC = 3 in CF4 and CF3 samples will be equivalent to a DoC of 0.75mm and 1mm in CF1 sample, respectively.

To make a one-to-one comparison, the x and y axes of Figure 5-12 were normalised to recognise the larger particles in the higher Coarsening Factors and the differences in the UCS values of the samples. The updated plot is shown in Figure 5-13 and confirms that the recorded response of CF1 to CF3, especially at the ductile region ($\text{DoC}/\text{CF} < 1$), is almost the same.

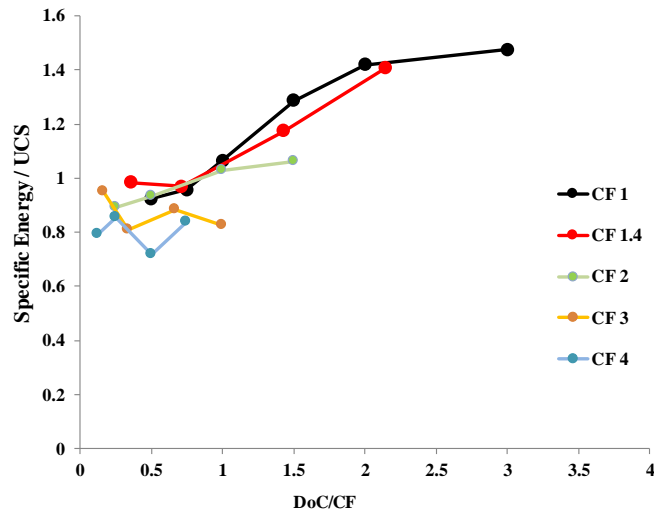


Figure 5-13 Normalised RST simulation results for different coarsening factors of Sample FNL3D-A

It can be concluded that for the given geometrical cutting parameters (cutter size and depth of cut), the particle size can be increased by a factor of three without a substantial effect on the normalised cutting force (or ISE). This has a huge effect on the total particle number and simulation time. It was explained in Table 4-5 that increasing the coarsening factor from 1 to 2, decreases the required particles to fill a standard size 1.5”×3” core sample by one order of magnitude. Despite this conclusion, to reduce the number of unknowns and isolate the scale effect, the rest of the simulation cases were performed on the samples of the original particle size without any coarsening (CF1).

In an effort to enhance the rock behaviour at deeper depths of cut, the effect of contact geometrical properties was investigated. Recall from Figure 4-16 that the contact geometrical settings affect the UCS response of the rock sample. A low number of elements causes a more ductile behaviour, while having more elements in each FJM contact increases the rock brittleness. In Chapter 4, after an extensive sensitivity analysis, the contact geometrical parameters were set to $N_{al} = 3$ and $N_r = 1$.

Two new samples were generated using the same properties of FNL3D-A, but different contact geometrical settings (N_{al} and N_r). The results (Figure 5-14) showed that this modification has a very minor effect on the rock behaviour in deeper cuts and the rock does not exhibit enough brittleness to form sufficient chipping required for a decreasing trend of ISE.

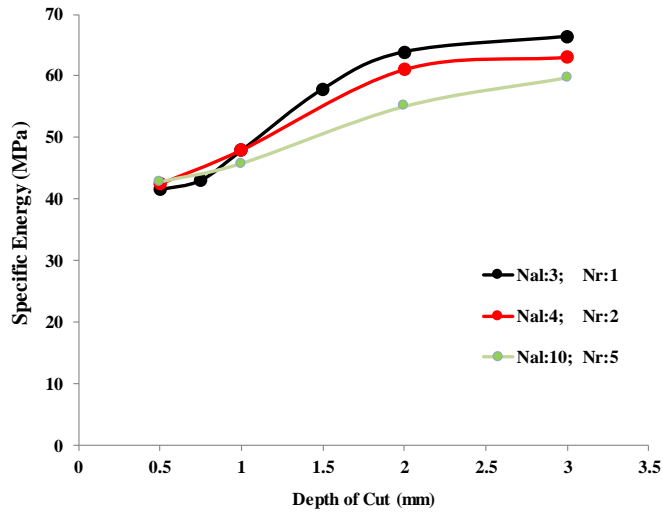


Figure 5-14 Effect of FJM contact geometrical settings on RST response

It was quoted in the literature (e.g. Rizo, 2013) that a low damping factor promotes chipping and brittle rock behaviour. To check the effect of damping factor on the RST response, two different damping ratios were investigated, both below the reference FNL3D-A case. It is clear from Figure 5-15 that reducing the damping factor only reduces the ISE (note the secondary axis scale), without changing the behaviour of the rock at deeper cuts.

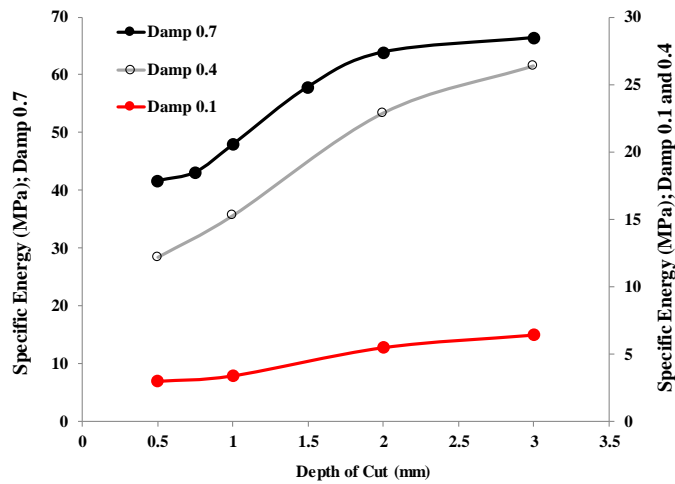


Figure 5-15 Effect of damping ratio on RST response

It was shown before that the RST simulation is velocity dependant. Figure 5-16 shows the effect of cutting speed on the calculated average ISE of sample FNL3D-A.

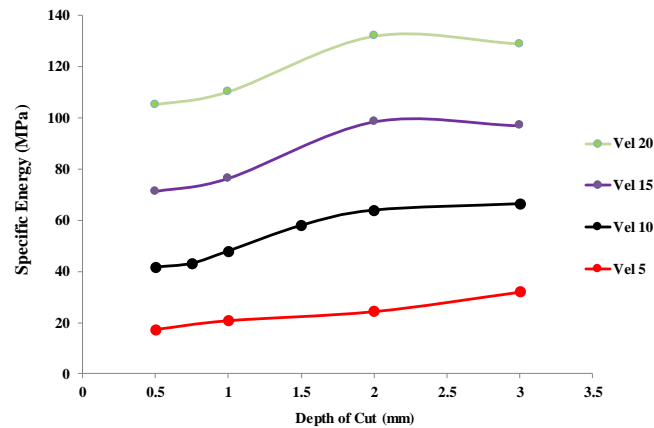


Figure 5-16 Effect of cutting velocity on RST response

In spite of the efforts to tune the parameters in favour of a more brittle behaviour, sample FNL3D-A failed to generate an acceptable cutting response. The next generation of FNL3D sample was built by modifying the properties of the intact rock to increase the rock's brittleness and its potential in chip formation.

- FNL3D-B: Uniform Properties, 80% Bonded Contacts, 20% Pre-existing Cracks (Slit Type), Existing Contacts: FJM, New Contacts: Linear Contact Model

Revisiting the microscopic pictures of Bentheimer sandstone reveals that not all the contacts are bonded by cement. In the absence of accurate information, a qualitative 20% was taken as the portion of initially un-bonded contacts, which were modelled by Slit-type flat-joint elements. The expectation was that the un-bonded contacts can act as the nuclei of crack generation / propagation, which favours the expected cutting response.

Adding the pre-existing cracks to FNL3D-A significantly altered the rock properties. Re-adjustment of the micro-properties (re-calibration) was required to retain the macro-properties. The new calibrated sample was called FNL3D-B and its cutting response is shown in Figure 5-17. Although at shallow

depths of cut the results are almost identical to FNL3D-A, it produced even more abnormal response at larger DoCs.

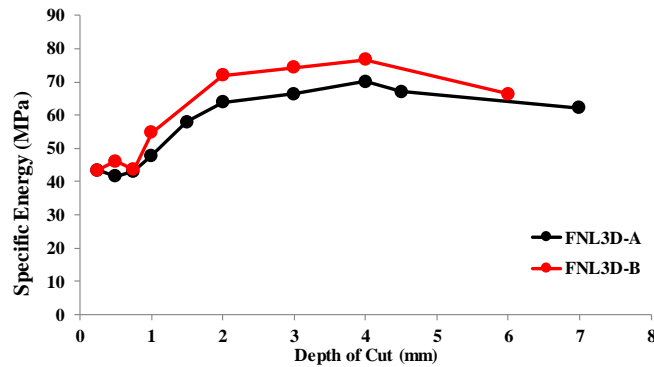


Figure 5-17 Effect of pre-existing cracks on RST response

Several sensitivity runs on cutter speed confirmed the velocity dependency of ISE (Figure 5-18). No improvements in chipping or ISE trend were observed by reducing the cutter velocity.

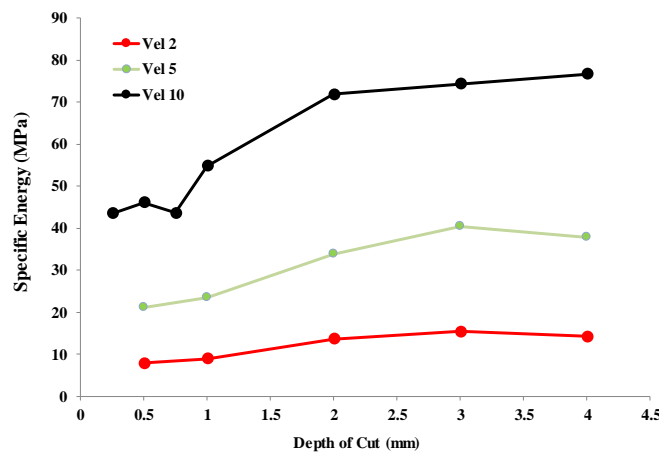


Figure 5-18 Cutting Velocity effect on FNL3D-B sample

- FNL3D-C: Non-uniform Properties, 80% Bonded Contacts, 20% Pre-existing Cracks (Slit Type), Existing Contacts: FJM, New Contacts: Linear Contact Model

In all the previous models, it was assumed that the FJM bond strengths (tension and cohesion) are constant in all the contacts. To assist in crack initiation and propagation, an average deviation factor of 20% was introduced to these parameters. This creates weaker spots in the rock body, which may assist in forming the chips in front of the cutter. The re-calibrated sample was called FNL3D-C. The results did not show any improvements in the ISE trend (Figure 5-19), and only the third validation criteria was conditionally met (ISE = UCS at specific cutting speed).

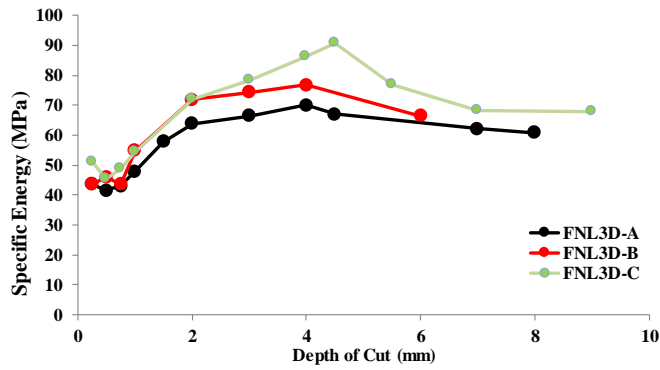


Figure 5-19 Effect of pre-existing cracks and non-uniform bond strength (FNL3D-C) on RST response

Similar to the previous samples, the sensitivity runs on the cutting speed proved speed dependency and no improvements on the trend.

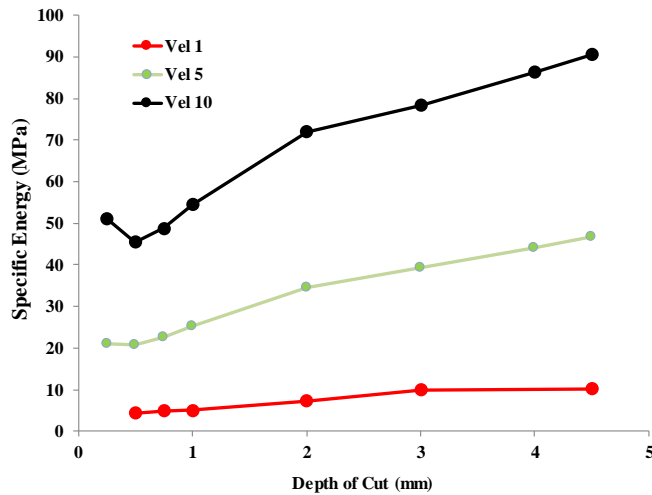


Figure 5-20 Cutting Velocity effect on FNL3D-C sample

- FNL3D-D: Non-uniform properties, 80% Bonded Contacts, 20% Pre-existing Cracks (Slit Type), Existing Contacts FJM, New Contacts FJM

Upon failure of all the efforts to obtain the expected trend from any of the previous samples, testing of contact type in the detached grains became essential. FNL3D-D was built using pre-existing cracks and non-uniform bond strength. Furthermore, FJM was assigned to all the new ball-ball contacts. This only applies to the newly-generated contacts in the failed grains, which occurs mainly in the crushed zone in front of the cutter. The contact element number was also revised from 3*1 to 10*5, that increased the total number of contact elements in the model, and the simulation time. All these modifications were expected to increase brittleness.

Figure 5-21 shows the cutting response of the sample at a cutter speed of 10m/s. The critical aspect of the results is the ISE trend. Contrary to all the previous RST modelling efforts, FNL3D-D met all the validation criteria because it produced chipping and exhibited a downward trend at deeper cuts, a critical depth of cut consistent with the expectations and a constant ISE at shallow DoCs. Although it should be remembered that the third criterion was only conditionally met, because of the speed dependency.

Of importance is the absolute value of ISE in the ductile region ($\leq 1\text{mm}$). While all the previous 3D models required a cutting speed of 10m/s to produce an ISE/UCS ratio close to 1.0, FNL3D-D needed a much slower speed ($\sim 5\text{m/s}$).

It was noted in Chapter 4 that the linear models are lacking the ability to effectively transmit momentum. This shortfall is known to be the reason for the abnormally high tensile strength of the PBM-generated samples. FJM on the other hand, can transmit torque and better represent the tensile strength of a rock sample. Since the main difference of the generation D with previous A, B and C samples was the contact type in the crushed area in front of the cutter, it is likely that the reason for the different cutting response of FNL3D-D is the importance of the grain-to-grain interaction in front of the cutter.

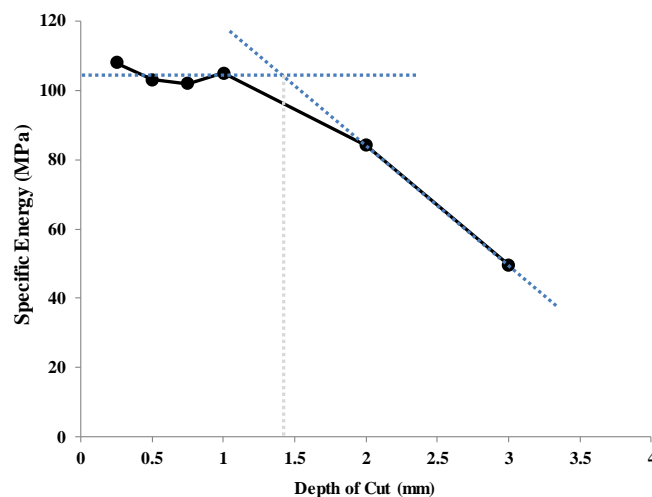


Figure 5-21 Cutting response of FNL3D-D

Repeating the RST at different cutter speeds showed the speed dependency. However, a decreasing ISE trend was observed in all the runs, beyond the DoC of 1mm.

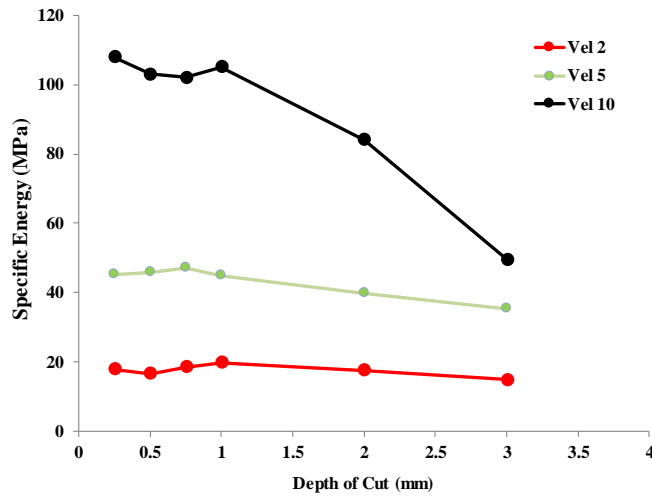


Figure 5-22 Cutting Velocity effect on FNL3D-D sample

A cutter speed of 5m/s was required to make ISE close to the UCS. Figure 5-23 shows a close-up of the response at this cutting speed, which shows in the ductile region of DoC = 0.25mm - 1mm, ISE (46MPa) is in good agreement with the UCS value of 42.1 MPa.

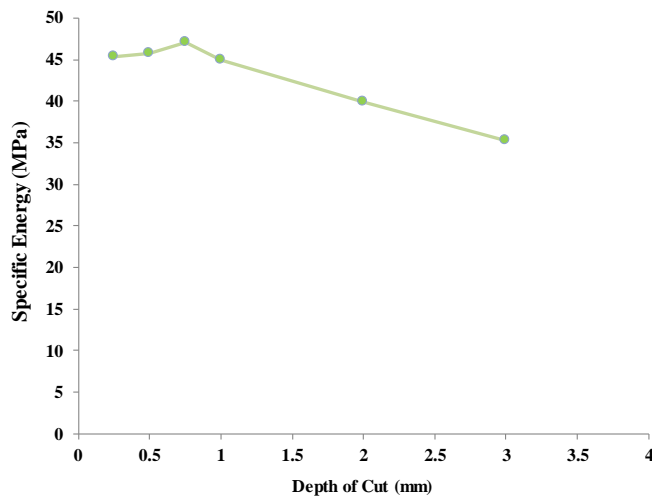


Figure 5-23 Cutting response on FNL3D-D at cutter speed of 5m/s

5.5) Application of RST in numerical modelling

The Rock Scratch Test simulation and the steps to achieve an acceptable result were explained in the previous sections. The strengths and weaknesses of the DEM in RST modelling was also discussed by making the references to meeting the validation criteria. The main purpose of simulating RST in the literature has been understanding the rock-bit interaction to optimise drilling, primarily by modifying the bit design or cutting parameters. This section aims to present the application of RST modelling in

testing the rock mechanical properties. In this case, RST effectively replaces the traditional UCS simulation method (compression test modelling). It was explained in Chapter 3 that RST is commonly used in the laboratory as a tool to determine the rock strength. From the literature review it was concluded that this application has been overlooked in numerical modelling.

5.5.1 UCS Estimation from RST Results

Estimating the numerical sample's UCS using RST results were previously discussed in detail. It was explained that in all the modelling efforts reviewed or modelled, the results were highly dependent on the cutting speed. Once the proper modelling speed was identified, similar techniques could be utilised to extract Young's Modulus and Poisson's ratio, in addition to the UCS, from a single run.

The concept of coarsening and scale effect was also discussed previously in this chapter (refer to Figure 5-12). To determine the required cutter speed for rock cutting so that the ISE/UCS be close to unity, a coarser model can be used to shorten the simulation time. The cutting parameters must be scaled with the same ratio as the grain Coarsening Factor (CF), as demonstrated in Figure 5-13. Details of the grain CF and the sensitivity analyses were covered in Chapter 4.

Figure 5-24 shows the Specific Energy values obtained from the different CF of sample FNL3D-D. Based on the feedback from the previous modelling efforts and to keep the cutting mode in the ductile region, the depth of cut for CF1 was selected to be 0.5mm. In all the other cases, DoC was equal to $CF \times 0.5\text{mm}$. The same method was applied for scaling the cutter width, to ensure that a wider cutter is used when the grain size becomes larger. A scaled cutter cuts the same number of grains and contacts in any CF values, in the cross-section specified by $\text{DoC} \times \text{Cutter Width}$.

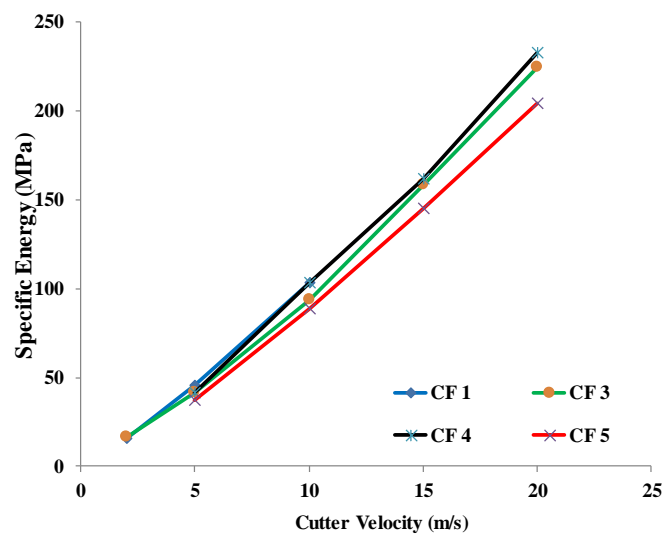


Figure 5-24 Cutting response on FNL3D-D sample with different CF

While very close, the results comparing different grain sizes show some differences in terms of the required cutter speed to obtain a specific ISE. This is attributed to the fact that increasing the grain size without altering the contact properties causes a reduction in the rock's uniaxial compressive strength. To account for this, the results were normalised, which made the trend much closer to a single line (Figure 5-25).

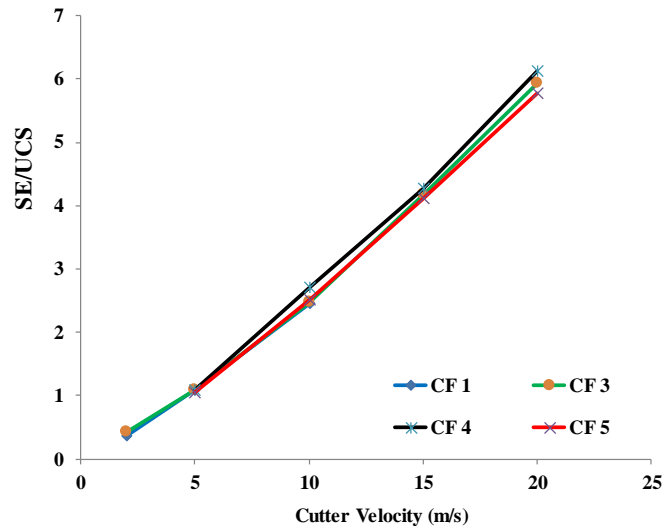


Figure 5-25 Normalised cutting response on FNL3D-D sample with different CF.

Figure 5-25 demonstrates the possibility of using a coarser sample to find the required cutting speed for a sample built from much finer particles. The immediate application of this technique is substituting the time-consuming, and in some cases impossible, compression test of very fine models (CF=1) with RST. The main advantage of this method is a severe reduction in the simulation time. The required time for RST simulation on a coarse model (CF=4) using the PC described in Table 3-1 is shown in Table 5-4.

Table 5-4 Simulation time required for RST simulation of FNL3D-D, CF=4.

Cutter speed	Simulation time (hr)
20	0.75
10	1.5
5	3
2	7.5

Due to the linear nature of the correlation between the cutter speed and the obtained ISE/UCS ratio, it is also possible to estimate the required cutter speed for an ISE/UCS=1 using least number of cutter speeds. In this case, only cutter speeds of 20, 10 and 5m/s were sufficient to establish the linear correlation for cutter velocity estimation. The UCS test for the CF=4 sample was completed in 0.75 hrs.

Once the cutting speed was determined from these tests, the subsequent scratch test modelling on the finest model (CF=1) took almost 4 hours, which makes the total required time equal of $0.75 + 1.5 + 3 + 0.75 + 4 = 10$ hrs. It should be noted that a direct UCS test was not possible on a CF=1 sample, due to the extreme simulation time and memory requirement. Completion of the conventional UCS test on a FNL3D-D sample with CF=2 (with almost 1/10 of the particles in CF=1 sample) took almost five days.

The following sections describe the methodology to extract other elastic properties of the numerical sample from the same RST test used in this section.

5.5.2 Young's Modulus

Each chipping event in RST can be considered a small-scale UCS test (Schei, 2000), as it involves increasing stress on a piece of rock until failure. Regardless of the failure criteria, Hook's law can be used to describe the relationship between the stresses and strains that the cutter movement induces in the rock. This applies if the depth of cut is large enough for a brittle cutting mechanism. Each segment of the cutting force fluctuations can then be analysed for the effective Young's modulus. An example rock cutting response for a FNL3D-D sample is shown in Figure 5-26.

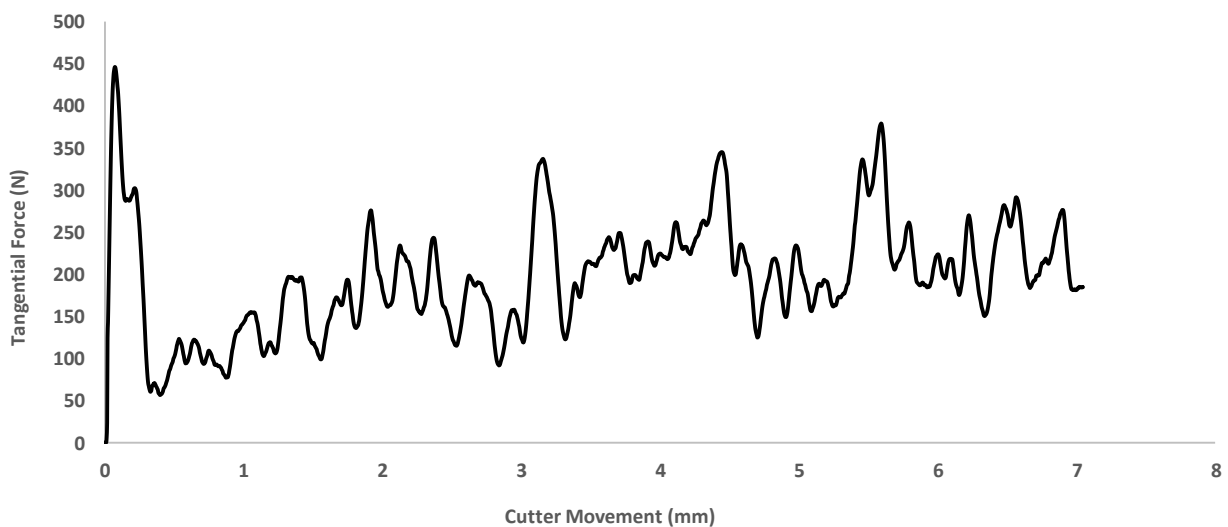


Figure 5-26 Example rock cutting response for a Bentheimer sample. Cutting speed: 5m/hr, DoC:2mm and BR=15°.

The areas of interest are the ascending parts of the curve, corresponding mainly to the behaviour of intact rock under stress. To smoothen the curve and delete the high frequency fluctuations in each step, a simple running average was used. Based on the observations, an averaging interval of 0.04 mm was enough for this purpose. First-order central-difference derivatives were calculated for each point and the data were filtered to only retain the positive derivatives. The second-order derivatives were also

calculated to identify the deflection points, to delete the flat areas before and after each stress increase. The remaining points (Figure 5-27) correspond mainly to the cutting intervals where the cutter was in contact with the intact rock. To make it consistent with other tests, the first 1mm of the data was also ignored to only consider the stable cutting interval.

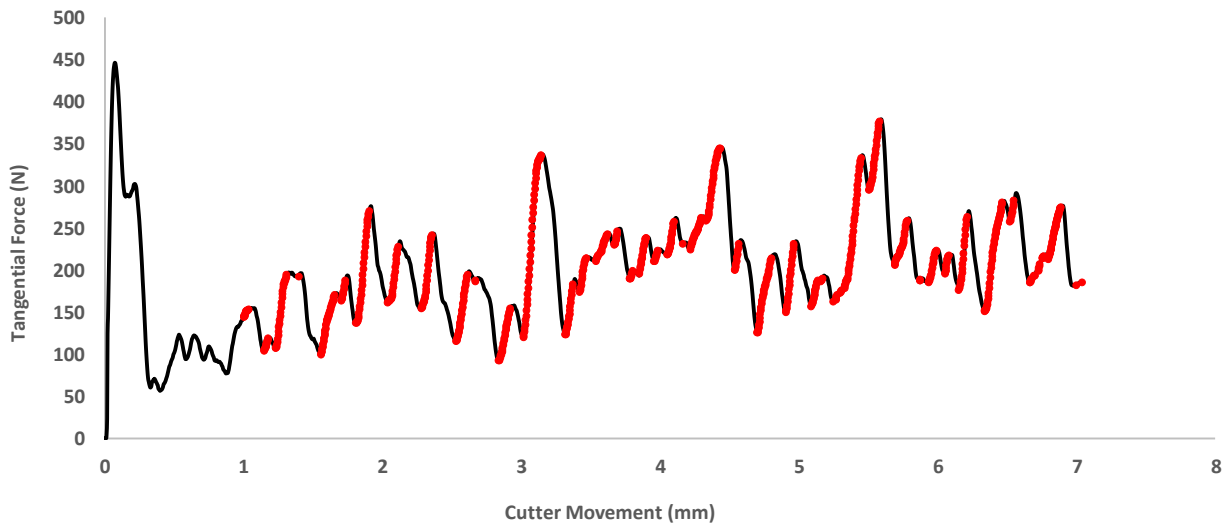


Figure 5-27 Filtered FNL3D-D cutting response

The stress was calculated by dividing the tangential cutting force by the cutting area ($F / (DoC \times \text{Cutter Width})$), and the strain was determined by the cutter's movement in each interval relative to the sample's length in front of the cutter. Based on the observations, the best results were obtained when the test origin for calculating the ΔL was assumed to occur at 80% of the distance between the end of the previous interval and the start of the new interval, as shown in Figure 5-28.

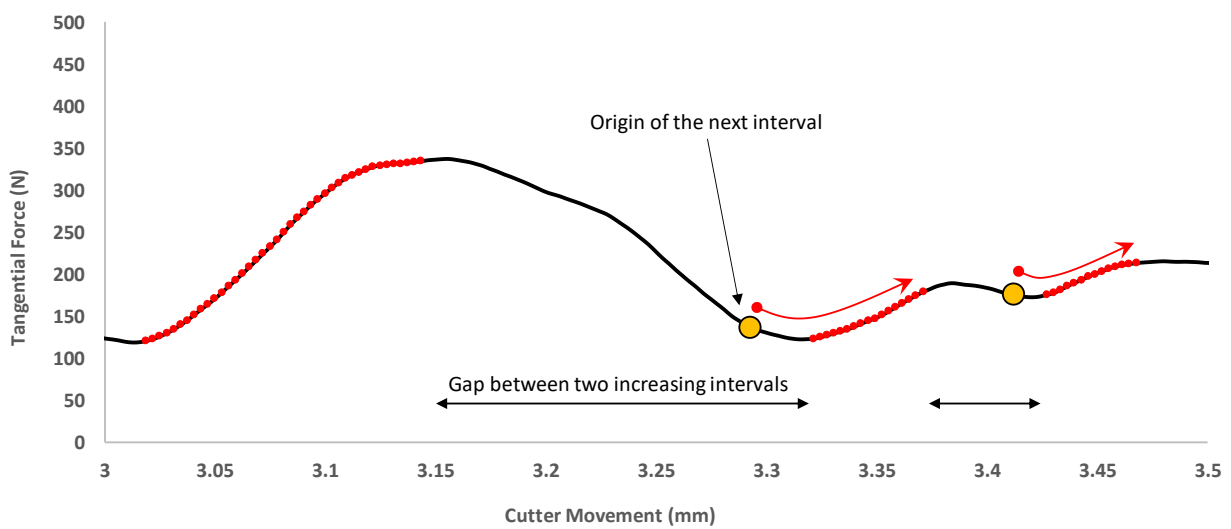


Figure 5-28 Strain calculation method

For any of the successive points in each interval, a value of E was calculated from the stress ($F/DoC \times \text{Cutter Width}$) and strain ($\Delta L/L$) values. A histogram of the data was plotted and the data points with the highest frequency (top 25%) were used to calculate the weighted average. A sample histogram is shown in Figure 5-29, with the weighted average E of 14.88MPa, which is a close estimation of the sample E , at 14.1 MPa. Conversion of the planar strain to 3D had a very minor effect in the final result.

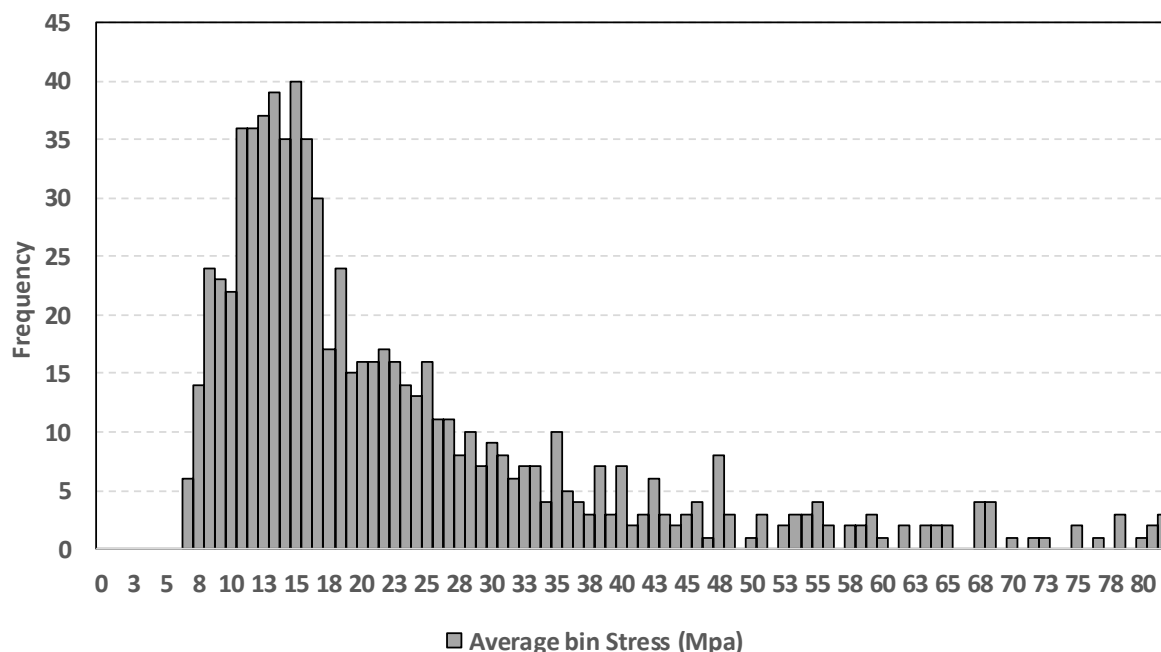


Figure 5-29 Histogram of the Young's Modulus obtained from Bentheimer cutting data

5.5.3 Poisson's Ratio

Sensors can be fitted inside the numerical sample to measure the deformation in the direction of cutting (X-axis), as well as in the lateral direction (Y-axis). To do the measurements, a network of equally-distanced points was designed inside the cubic sample and the closest grains to these points were selected as Gauge Grains (Figure 5-30). Their displacement was recorded at each time-step and the lateral and tangential strains were calculated.

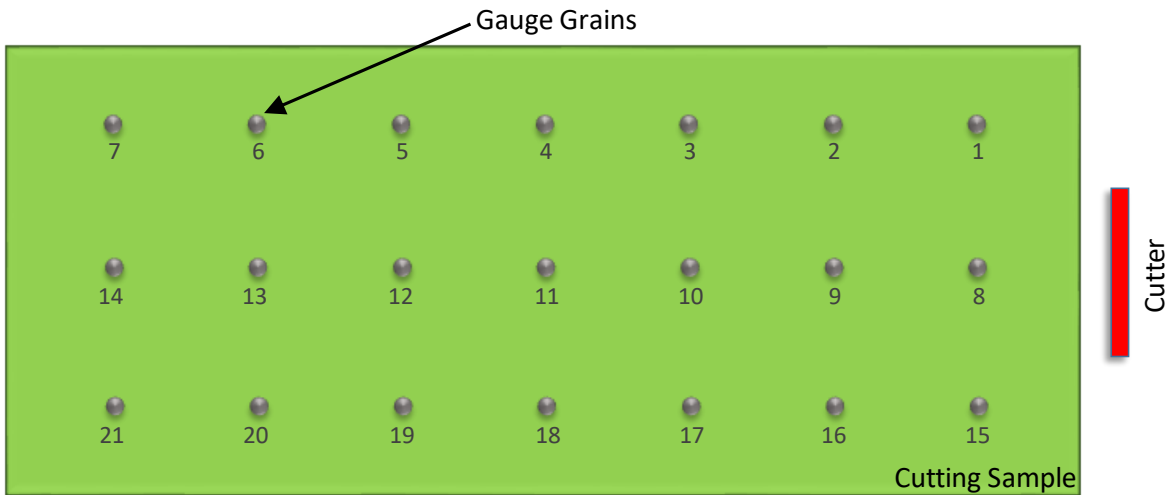


Figure 5-30 Gauge grain set up for strain measurement

Investigation of the X and Y stresses showed that an area of highly non-uniform stress distribution exists close to the cutter, where the magnitude and direction of stresses severely changes over small intervals. Away from the cutter, however, the stress is more uniform. This can be seen from Figure 5-31, where the lateral displacement is shown by filtering different parts of the cutting sample. The white curve is the cutting force, which emphasizes all three pictures are generated from the same time-step. The small dots visible in the filtered areas are the Gauge Grains. The non-uniform displacement close to the cutter is evident in the top picture. The middle and bottom pictures show that the displacement, and hence strain distribution, becomes more uniform as we move away from the cutter.

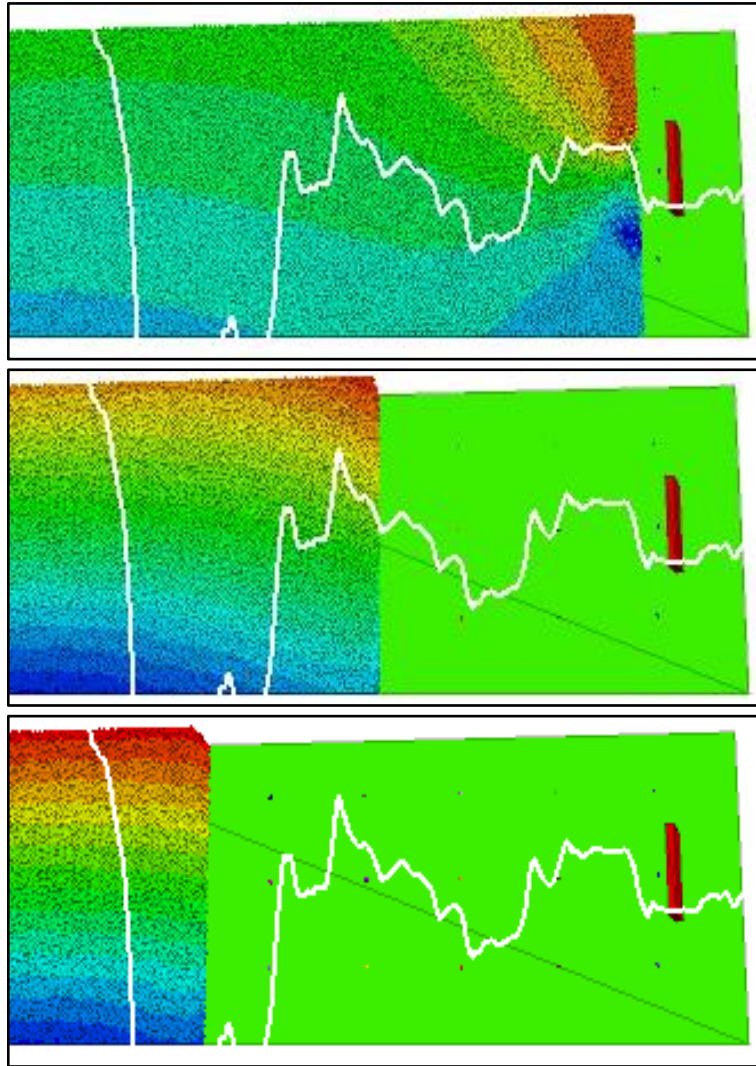


Figure 5-31 Lateral displacement along sample's length

The Poisson's ratio can be calculated by dividing the lateral to longitudinal strains. Each strain can be calculated from different pairs of gauge grains. Due to the system configurations (stress on a thin bed), the stress-strain relationship would be planar, which needs to be converted to 3D.

The ν values were calculated for different configurations of Gauge Grains, as shown in Figure 5-32. As expected, it was observed that the Poisson's ratio calculated from the Gauge Grains located farthest away from the cutter yield closer values to the results derived from the UCS tests. This is the area shown in the bottom picture of Figure 5-31, where lateral displacement is more uniform. A sensitivity analysis on the lateral distance of the Gauge Grains showed that a minimum distance of twice the cutter width is required for producing stable results. Below this distance, severe fluctuations were observed.

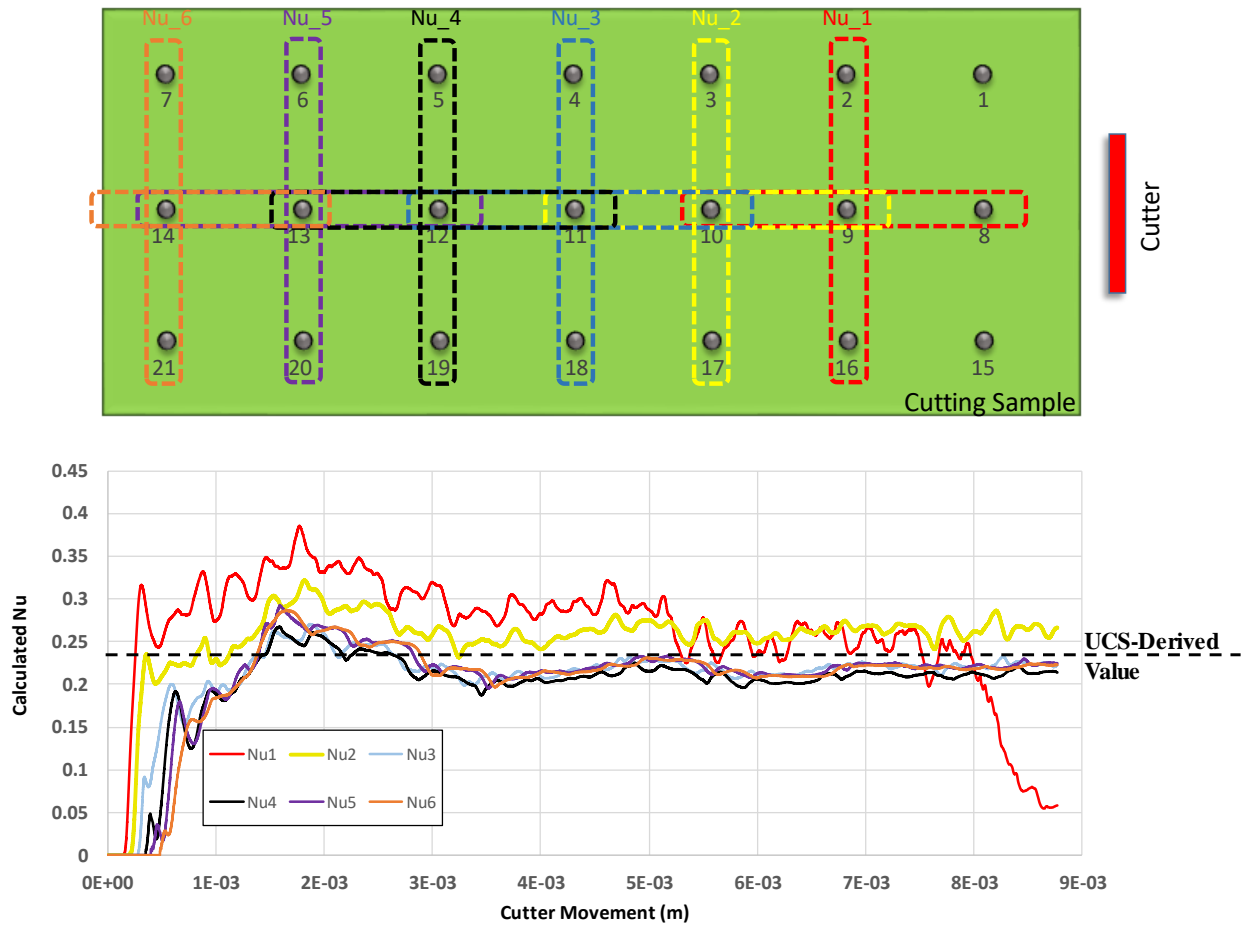


Figure 5-32 Different configurations of Gauge Grains for strain calculation

In a relatively long sample, the Poisson's ratio calculated from any of the Gauge Grains are almost the same, and very close to the UCS-derived value. As the numerical sample gets shorter, mainly for reducing the simulation time, the ν value starts to deviate and only the reading from the last point (farthest from the cutter) should be used.

5.6) Chapter Conclusions

The chapter presented the 2D and 3D rock scratch test simulations. All the numerical modellings were performed on the actual Bentheimer grain size, with sensitivities performed on scale effect, damping factor, cutting speed and back-rake angle. Validation criteria were established and used to assess the validity of the numerical results. The evolution of the numerical samples explained from simple 2D models to the final samples, where a comprehensive calibration method was used to accurately match the macro-properties while honouring the microscopic features, including the pre-existing cracks, varying cement quality (bond strength) between the contacts and the angular nature of the grains which promotes interlocking. Initial efforts suffered from a lack of sufficient chipping and exhibited an unacceptable ISE trend. Model refinement improved the match. The results of the final model were shown to meet two of the three validation criteria, while conditionally meeting the last criterion.

A method was presented to replace the conventional UCS test. Practical techniques presented to reduce the simulation time and extract the elastic properties from a single RST simulation run.

6 Other Example Applications

An introduction to the Discrete Element Method, a brief summary of previous efforts in modelling synthetic rocks and Rock Scratch Testing, and simulation of RST using DEM were presented in Chapters 3 to 5. This Chapter is aiming to further demonstrate the application of DEM in geomechanics. The applications selected for modelling were ongoing experimental research projects at the Petroleum Department at the time of carrying out this research and were chosen to cover a wider range of geometric and kinematic settings:

- The Thick-Walled Cylinder (TWC) represented a case with a minimum particle movement. The TWC sample was essentially at static conditions, while a radial load was gradually applied.
- In the case of Rock Scratch Testing, while the sample was at static conditions, the cutter was moving at a relatively high speed to cut a groove at the surface of the sample.
- In erosion modelling a completely different setting was considered. Discrete particles were used to match the apparent fluid rheological properties. The modelled discrete fluid “flowed” through a hole inside the modelled sample to investigate the erosional effects.

Compared to the Bentheimer sandstone, very limited information was available from the synthetic samples used in the applications presented in this chapter; hence simple models were selected to match the rock properties. The results, although encouraging, should only be considered as preliminary. Further work is recommended to fully understand the capabilities and limitations of the discrete element model in simulating these applications.

6.1) Thick-Walled Cylinder Test

6.1.1 Introduction

The TWC experiment is designed to investigate the sanding risk under varying conditions. The sanding phenomenon occurs because of a combination of mechanical failure and erosion, governed by geomechanical and hydrodynamic processes, respectively (Berntsen and Papamichos, 2012). These are also the parameters which determine the best completion method for oil and gas wells.

To determine the sanding onset, laboratory studies are normally carried out using the thick-walled cylinders under controlled conditions. Of the critical findings of these tests is the dependency of the results on the scale factor, namely the ratio of the sample’s outer to inner radius, OD/ID. A good example of the TWC experiments is the study performed by Veeken et al. (1991), where it was concluded that increasing OD/ID causes a rise in the sanding onset. The scaling effect was also studied

as part of a PhD thesis at the Petroleum Department of Curtin University (Tehrani, 2018). Analytical models, as well as experimental tests confirmed the effect of scaling factor, the results of which will be used to validate the numerical simulations presented here. As in the case of RST, the analytical methods are generally solutions to simplified problems and often ignore the discontinuities in the rock bodies.

In this study, a numerical model was built to match the known properties of the loose synthetic sandstone used in the TWC experiments. The modelling results were compared to the experimental outcome, as well as the trends obtained from the analytical methods. The experimental set up and early numerical results of the current study were previously published (Tehrani and Joodi et al., 2017). The following is a summary of the experimental procedure, followed by more detailed numerical modelling and the simulation results for a wider range of OD/ID.

6.1.2 Experimental Set-up

To evaluate borehole stability under underground stress conditions, a thick-walled cylinder test is routinely used. The test involves applying confining stress on a hollow core sample, with an outer diameter of OD and a hole size diameter of ID. The critical parameters in determining the TWC results are rock strength, OD/ID ratio and sample size (scale effect).

The experiments related to the current study were performed on soft synthetic sandstones. Regrettably, very limited information was available from the mechanical properties of the samples, as shown in Table 6-1. The Particle Size Distribution (PSD) of the sample was available from a sieve analysis performed on the constituting sand before sample preparation. This is shown in the numerical modelling section.

Table 6-1 Properties of synthetic rock samples used for TWC tests (Tehrani and Joodi et al, 2017)

Physical properties			
ρ_b	Bulk density	1,815	kg/m ³
ϕ	Porosity	0.26	-
Elastic properties			
E	Young's modulus	5.9	GPa
ν	Poisson's ratio	0.25	-
Strength parameters			
UCS	Uniaxial compressive strength	17.92	MPa

Figure 6-1 depicts the experimental set up of a TWC test. The samples are inserted into a sleeve, which subsequently fits in the cylindrical triaxial cell. The radial and axial stresses are controlled by the ISCO pumps. The applied stresses and the resultant strains are measured and recorded by a data acquisition system.

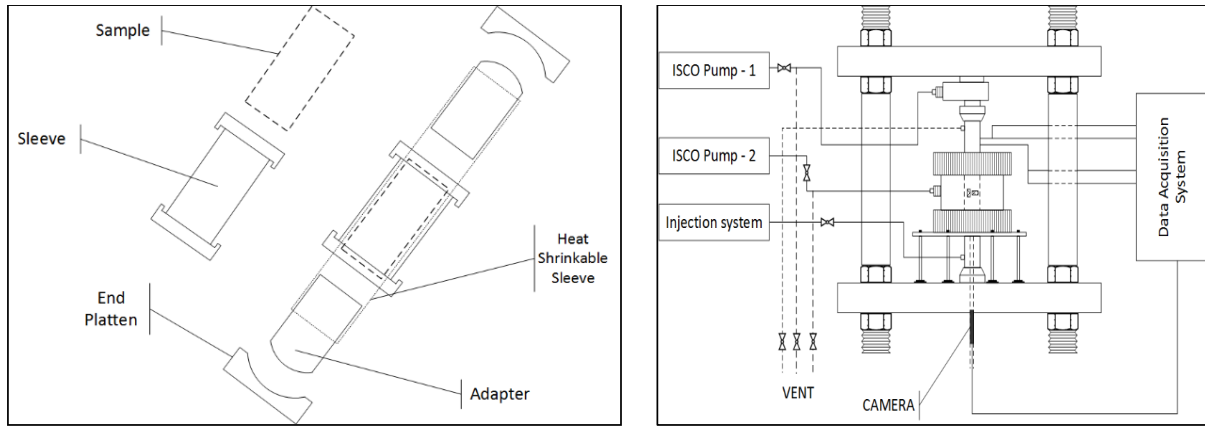


Figure 6-1 Left: Sample and sleeve arrangement. Right: TWC experiment set-up (Tehrani et al, 2017)

The experiment was performed on samples with different hole sizes to investigate the effect of OD/ID ratio on TWC strength. Figure 6-2 summarizes the experimental results and compares them with the analytical solutions.

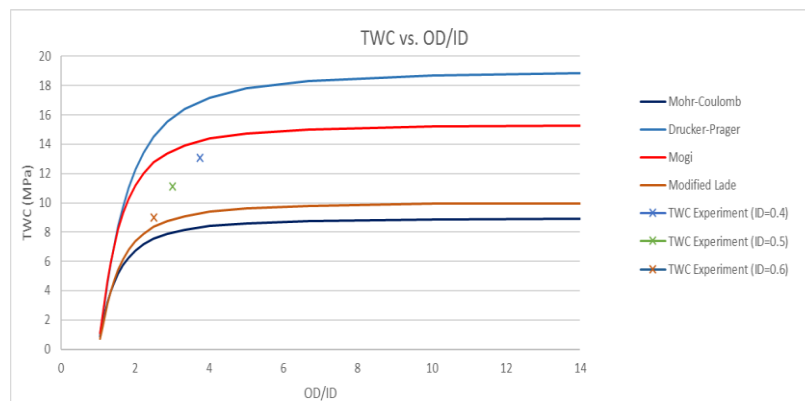


Figure 6-2 TWC test results versus different analytical models (Tehrani et al., 2017)

6.1.3 Numerical Set-up and Results

The numerical simulation was performed using a simple Parallel Bond Model and spherical particles. Similar to the strategy used in Chapter 5 for RST simulation, to isolate the particle size effect, it was decided to use the particle size distribution from the sieve analysis without coarsening. A comparison of the physical and numerical samples' PSD is shown in Figure 6-3.

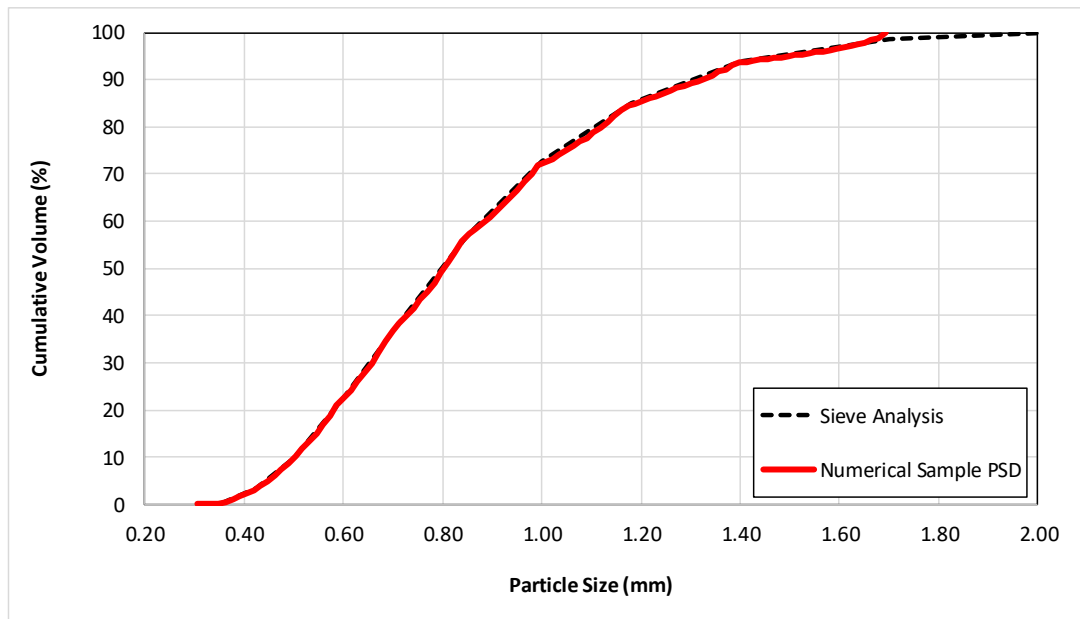


Figure 6-3 Sieve Analysis versus Numerical Sample PSD

Only UCS test results were available for the synthetic rock samples. Due to the uncertainties in the rock properties and exploratory nature of the numerical modelling, a simple PBM was used and calibrated to match the UCS stress-strain curve. No effort was made for further calibration, due to the lack of information from rock properties. The selected micro properties are listed in Table 6-2.

Table 6-2 Micro properties of the simple model for exploratory TWC modelling (Tehrani et al, 2017)

Micro-properties of the bonded particle model	
Particles Deformability	3.0 GPa
Particles K Ratio	3.5
Contact Deformability	3.0 GPa
Contact K Ratio	3.5
Parallel Bond Tensile Strength	3.8 MPa
Parallel Bond Cohesion	3.8 MPa

For each OD/ID ratio, the internal diameter of the thick-walled cylinder was calculated, and a hole is created at the centre of the sample. The membrane method, developed in Chapter 4, was used to apply the axial and radial stresses. It was previously explained that the reason for using this method instead of rigid walls was to allow the sample to deform naturally under the applied stresses. The model set-up is shown in Figure 6-4.

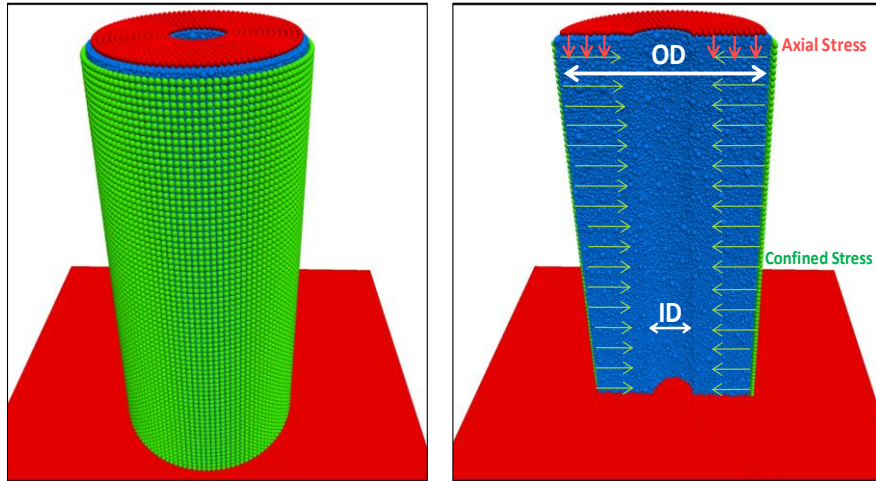


Figure 6-4 Left: Generated membrane around the sample. Red layer exerts the axial stress while the green layer applies the radial stress; Right: a cut-through view of the sample (Tehrani et al, 2017)

Because the membrane balls were distributed uniformly, it was possible to calculate the force required from each ball to achieve the target radial and axial stresses. Initially the axial stress was applied in 20 increments. After each increment ($F_{\text{target}}/20$), the model was cycled enough to reach a constant stress state. The target for the radial stress was set to 1.5 times the expected failure value and the equivalent radial forces were applied in 40 increments. Two measurement spheres inside the sample monitored the stresses, as shown in Figure 6-5. It should be noted that because of the positioning of the measurement spheres in the sample, their recorded value is not equal to the radial stress and the values were only used as an indication of stable condition.

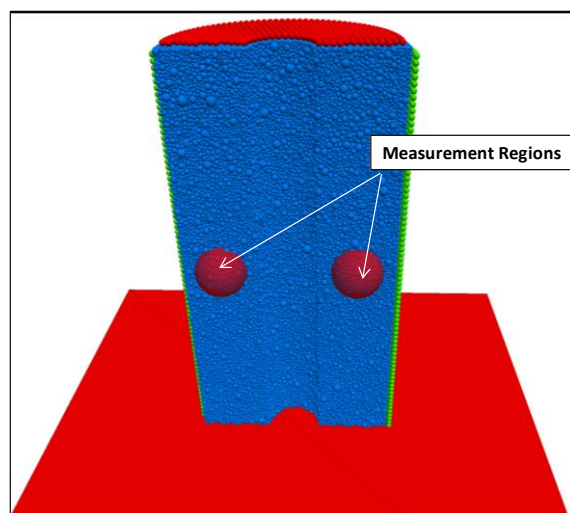


Figure 6-5 Measurement spheres

Based on the observations, it was concluded that the failure can first be detected visually in software snapshots, followed by the stress-strain curves. The first failure indication on the stress-strain curves

occurs ~ 0.5 MPa after visual grain movement detection. For this reason, the camera view was set inside the internal hole and a picture was exported at regular intervals. The failure could easily be identified when the exported pictures were animated.

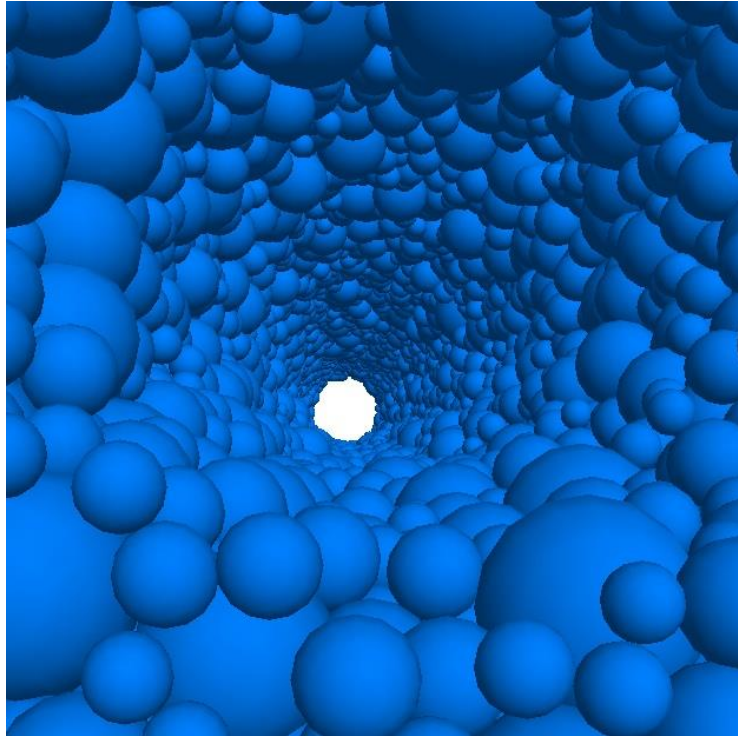


Figure 6-6 Camera view inside the internal hole, which was used for detecting the sample failure

The failure point was taken as the stress value at which the first grain detaches from the borehole. Figure 6-7 compares the results of numerical simulations with the laboratory observations. A clear increasing trend was obtained between the TWC failure points and the OD/ID ratios, which was in agreement with the expectations. Surprisingly, the numerical failure stress values matched Mogi's correlation.

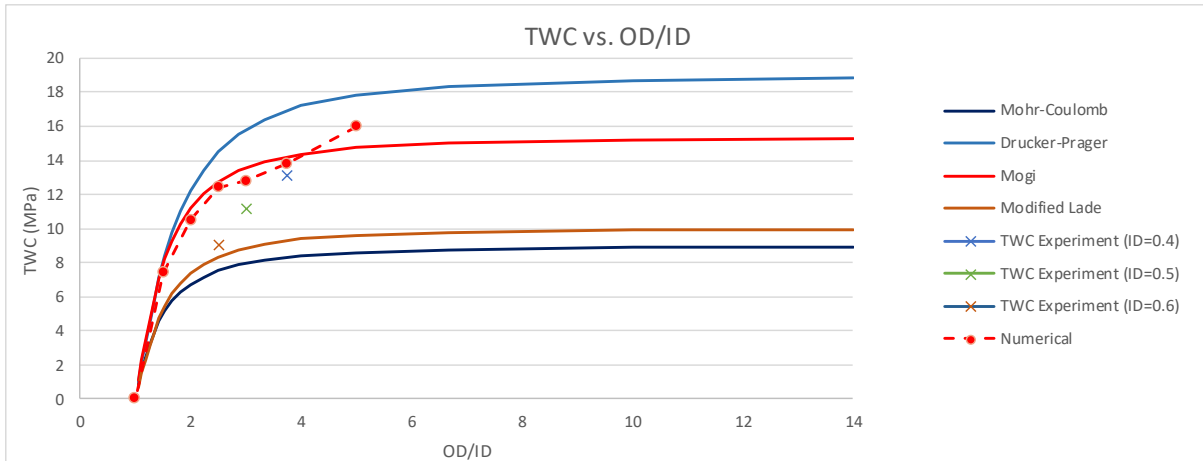


Figure 6-7 Numerical simulation results of TWC test versus experimental observations

6.1.4 Comparison with Experimental and Analytical Methods

While the numerical method, in the simplest form, seems to show the general trend, further calibration is necessary to match the experimental results, especially at lower OD/ID ratios. This was not possible due to the lack of information from the mechanical properties of the samples. As outlined in the introduction of this Chapter, this simulation was initiated because of the opportunity of having access to the experimental results in the ongoing projects in the department. The results further proved DEM capability in practical geomechanical applications. Use of more representative contact models, such as Flat-Joint Model, is likely to improve the match with experimental data.

6.2) Erosion

6.2.1 Introduction

DEM simulation of erosion in soft media is an interesting case, which, similar to the TWC, was selected to demonstrate a wider range of geomechanical applications that DEM can model. The phenomenon under investigation is erosion of an extremely soft unconsolidated sandstone, exposed to a fluid flow. The laminar flow hydraulics can be derived analytically to estimate the drag on flat surfaces. Turbulent flow, on the other hand, is time and space dependant with a random nature and large number of spatial degrees of freedom (Mathieu and Scott, 2000). The situation can be even more complicated when the problem involves drag calculation on a rough surface, similar to the internal wall of a wellbore. The drilled hole is often not smooth and the surface erosion changes the exposed surface topology, which in turn affects the drag force and erosion rate.

Commercial simulation packages are available, capable of estimating the drag force of laminar or turbulent flow regimes, that use the equations (laminar flow) or empirical correlations (turbulent flow) to calculate the force applied on each segment of the wall. All these packages use the continuum methods, which are perfect for the fluid phase. The rock phase, however, should ideally be simulated with the discrete model to efficiently capture all the existing discontinuities (variations in contact bond strengths, pre-existing cracks, faults etc).

The objective of this section is to explore whether it is possible to simulate both the rock and fluid phases - in an erosion modelling application - by the discrete element model. To the author's knowledge, this work has not been carried out before.

6.2.2 Experimental set up

The experimental equipment was designed during an ongoing research in the Petroleum Department of Curtin University at the time of carrying out the current research. The drilling fluid was stored in a large tank. A pump flows the fluid through especially designed clear tubes, equipped with pressure gauges and sand detectors. The fluid then passes through a pre-fabricated hole inside the synthetic sample, as shown in Figure 6-8. A pipeline is fitted inside the sample's inner hole to emulate the fluid flow through the wellbore's annulus. The exposed sandstone length was 400mm. The annulus had an outer diameter (Sample's ID) of 60mm and an inner diameter (pipeline OD) of 45mm.

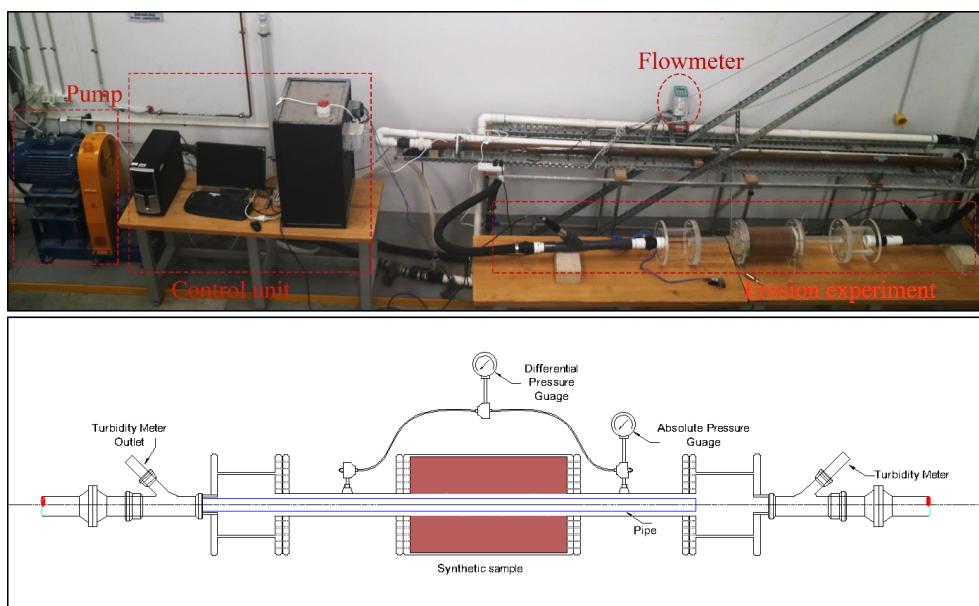


Figure 6-8 Erosion modelling experimental setup (Bayati, 2018)

The sample's strength (UCS) was measured by a rock scratch test using the Wombat equipment. Hydraulic properties of the drilling fluid were measured in the lab. The erosion test was performed by flowing the fluid at different rates and measuring the eroded sand grains' mass. An example of the recorded data during the experiment is shown in Figure 6-9.

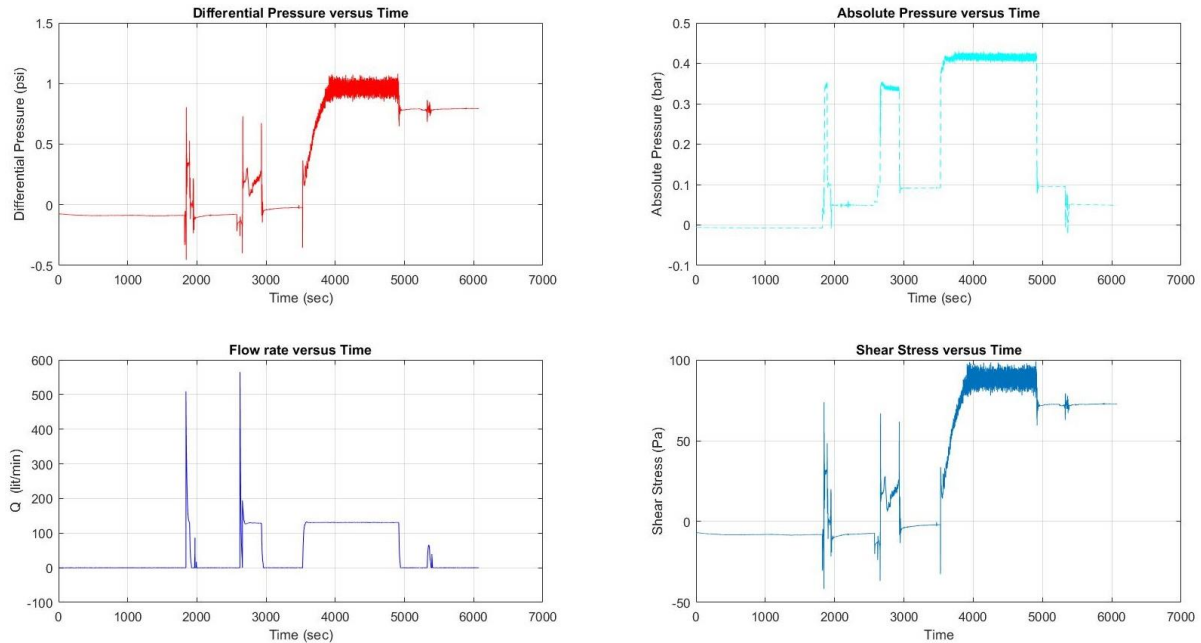


Figure 6-9 Example output during an erosion experiment

Table 6-3 shows a dataset provided by Bayati (2018), which was used for validation of the numerical model.

Table 6-3 Erosion experiment parameters

Rock strength (UCS)	1.5 MPa
Drilling fluid	Water
Erosion rate	50 gram/15min

6.2.3 Numerical Modelling

The erosion test was simulated using the discrete element method by honouring the geometrical set-up of the experimental equipment. The rock was modelled by simple parallel-bond contacts and the fluid by very small discrete particles “flowing” through the rock sample.

To properly simulate the sand-face erosion, one should accurately model the stresses applied to the sand grains as a result of the fluid flow. This is a dynamic calculation, as the magnitude of the stresses

depends on the rheological properties of the fluid, flow parameters and the geometry of the rock-fluid contact. Upon failure of each grain, the stress applied to the remaining intact rock particles can change due to the alteration of the sand-face topology. Analytical modelling of the applied stresses can be extremely complicated, especially in the case of turbulent flow. Numerical modelling can improve our understanding of the process. DEM appears to be one of the possible tools for erosion modelling, and in fact is recommended for this application in the literature: “*Failures in geomechanics often involve very large displacements or deformations. DEM models can therefore inform our understanding of important failure mechanisms. Examples of mechanisms that cannot be simulated using a continuum approach include internal erosion, scour and sand production in oil reservoirs.*” (O’Sullivan, 2011)

- **Rock Sample modelling**

An ultra-soft synthetic rock sample was used in the laboratory tests, with a UCS of 1.5MPa, as measured by scratch tests. No other mechanical properties were available from the physical sample. A simple parallel-bond model was built to match the UCS, with properties shown in Table 6-4.

Table 6-4 Numerical rock sample properties

Property	Value	Property	Value
Sample Size	R:19mm H:76mm	Contact Young's modulus (GPa)	2.0
Particle density (kg/m ³)	2500	Particle stiffness ratio	1.2
Minimum particle radius (mm)	0.6	Particle friction coefficient	0.57
Particle size ratio	1.66	Parallel bond normal strength (MPa)	3.1
Parallel bond friction angle (Degree)	0.5	Parallel bond cohesion (MPa)	8.0

- **Fluid Modelling**

The fluid phase was modelled as fine discrete particles *flowing* in the dominant flow direction. The damping ratio was set to zero to prevent any velocity loss as the particles collide with each other. The micro-properties were tuned to match the fluid behaviour observed in the experiments. The process is similar to tuning the micro-properties of a bonded sample to obtain the desired mechanical characteristics. The most critical fluid macro-property in this study is the viscosity, which affects the drag force on the sand grains.

The drag force was matched in two phases:

- Drag on a flat surface:
To match the fluid drag force on particles partially exposed to flow, as shown by the green highlight in Figure 6-10.
 - Drag on a sphere:
To tune the drag force on particles which are almost completely exposed to the flow, as shown in red in Figure 6-10.
- In each case, the micro-parameters of the fluid phase particles were changed until the drag force matched the analytical equations.

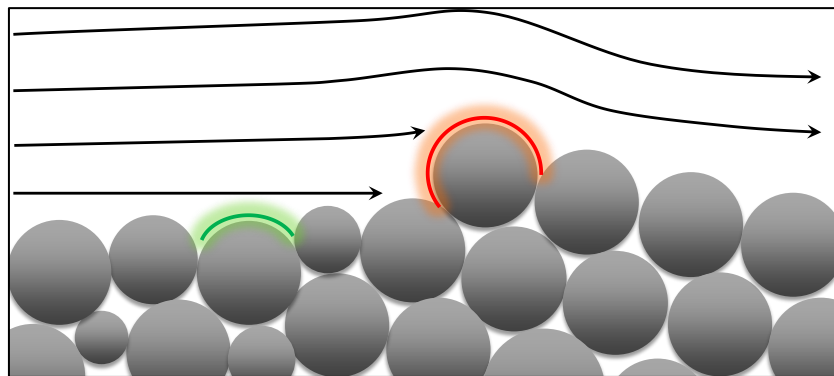


Figure 6-10 Level of particle exposure to fluid flow

- ***Drag on Flat Surface***

Figure 6-11 shows the model set up for matching the fluid drag on a flat surface. Fluid particles are generated in a regular pattern at one side of the constraining walls, called the “*Ball Assembly Area*”. The micro-properties of the particles are assigned, as well as their velocity components. Before contacting the measurement-plane placed in the middle of the constraining walls, the particles are allowed to “flow” to get a more random configuration. The model tracks the particle movements and new particles are generated when the fluid particles pass the ball assembly area. The plane dimensions are $R*(3R)$, where R is the average grain size of the rock sample.

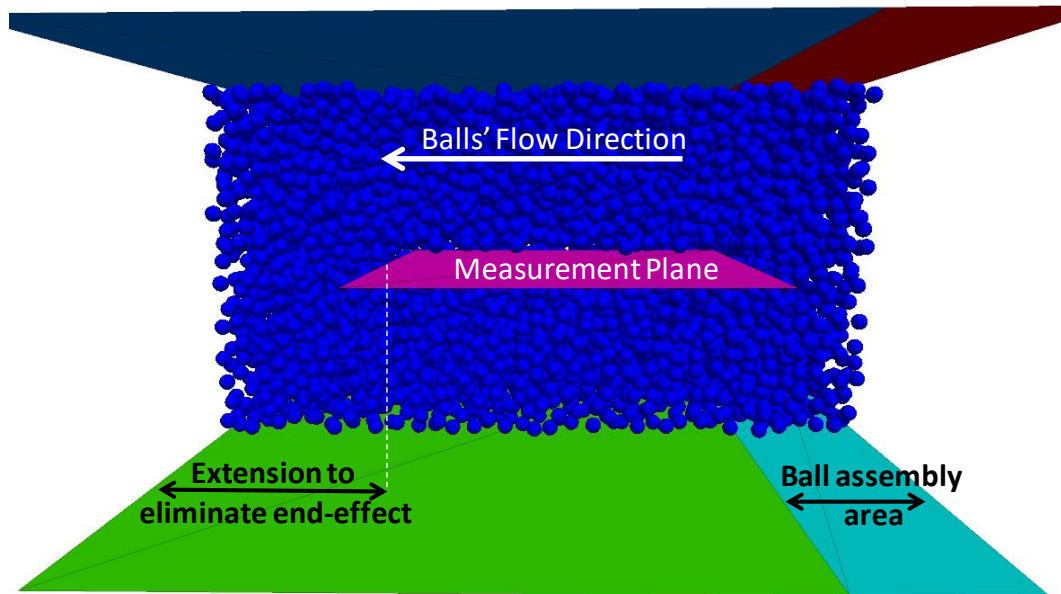


Figure 6-11 Model set-up for drag measurement in a flat plane

The particles' dominant velocity (in the direction of the flow) was assigned as a constant (flow rate / cross sectional area), while the lateral velocities were set with a random function, so that the particles were moving randomly in different lateral speeds. Then, the model was cycled and the particles “flowed” towards the measurement plane. It was observed that the drag was mainly determined by the lateral velocity of the particles and their friction coefficient. Finer particles generated a more uniform drag force, however they required a higher simulation time.

- ***Drag on sphere***

A spherical object, called “*Measurement Sphere*”, was set between the constraining walls. The sphere diameter was set to be equal to the average grain size. Fluid particles were generated in the assembly area and their properties and velocities were assigned. The model cycled to let the particles flow over the measurement sphere. The model set up is depicted in Figure 6-12.

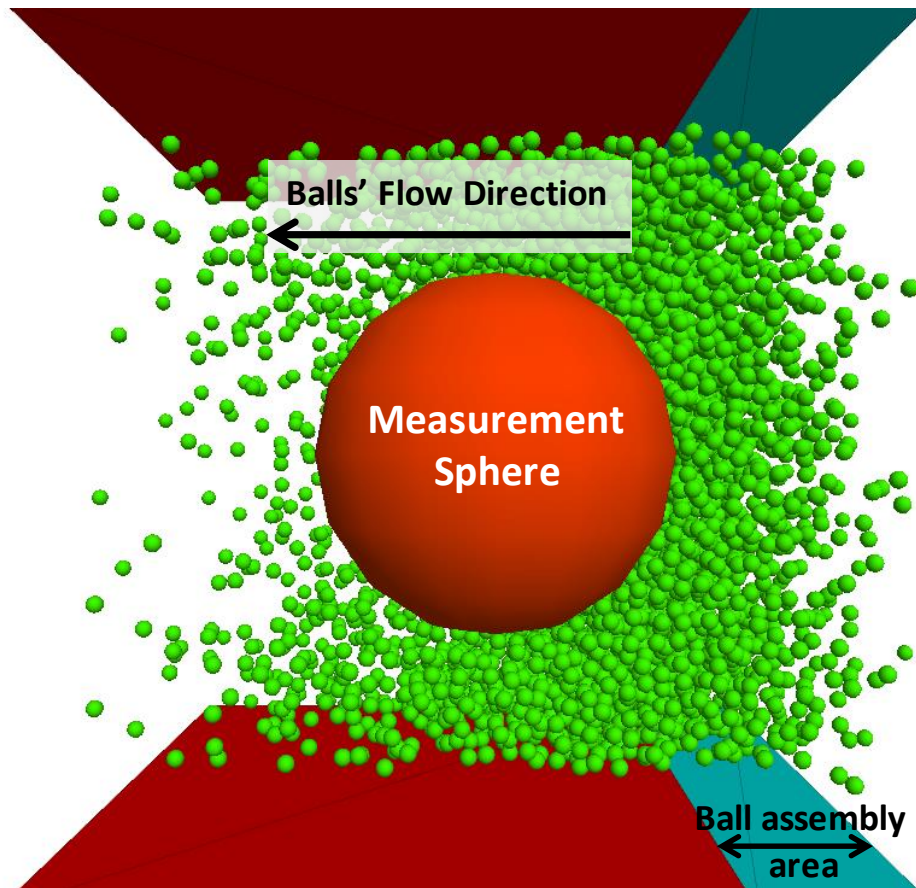


Figure 6-12 Model setup for measuring the drag on a spherical object. Fluid particles are filtered to make the measurement sphere visible.

The force applied from the fluid particles to the measurement sphere was recorded. The micro-properties of the fluid particles were calibrated to obtain the same drag as predicted by analytical equations. It should be noted that larger fluid particles reduced the simulation time, however the recorded force was too erratic. It was found that the mass ratio of the measurement sphere to fluid particles should be at least 120, to obtain a reasonable smooth force response. Figure 6-13 shows an example of the recorded forces.

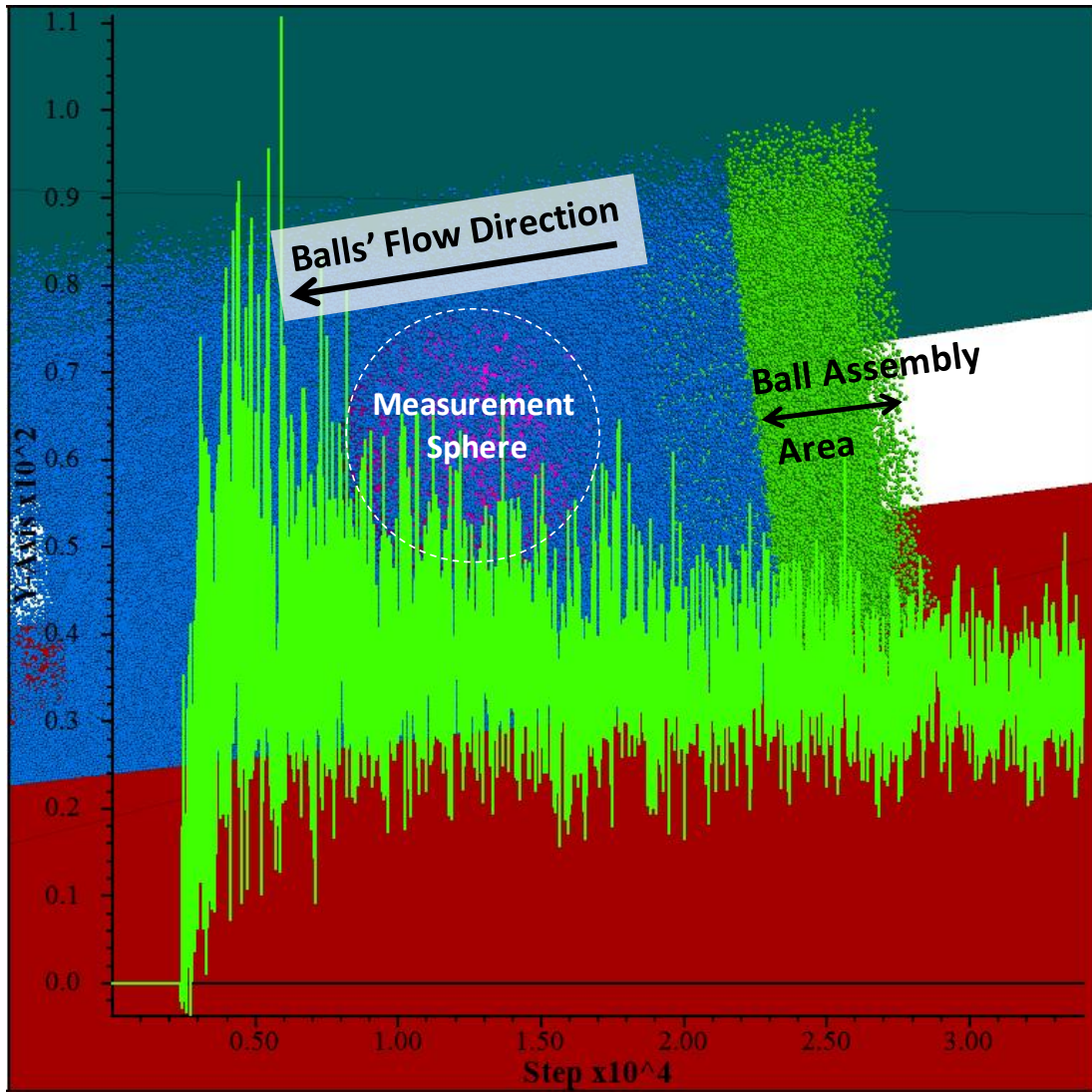


Figure 6-13 A typical response from the discrete fluid particles' flow over the spherical object. Green particles are freshly generated in the Ball Assembly Area. Blue particles were generated in previous batches. The green curve shows the recorded force.

- ***Erosion Numerical Model Set up***

The geometrical setting of the experimental design was modelled in PFC3D by creating a hole (D=60mm) inside the sample and generating a cylinder inside the hole (D=45mm). The fluid properties obtained from the flat surface and spherical object calibration were used for the fluid particles generated in the assembly area. As shown in Figure 6-14, because of the symmetry, only half of the sample was modelled.

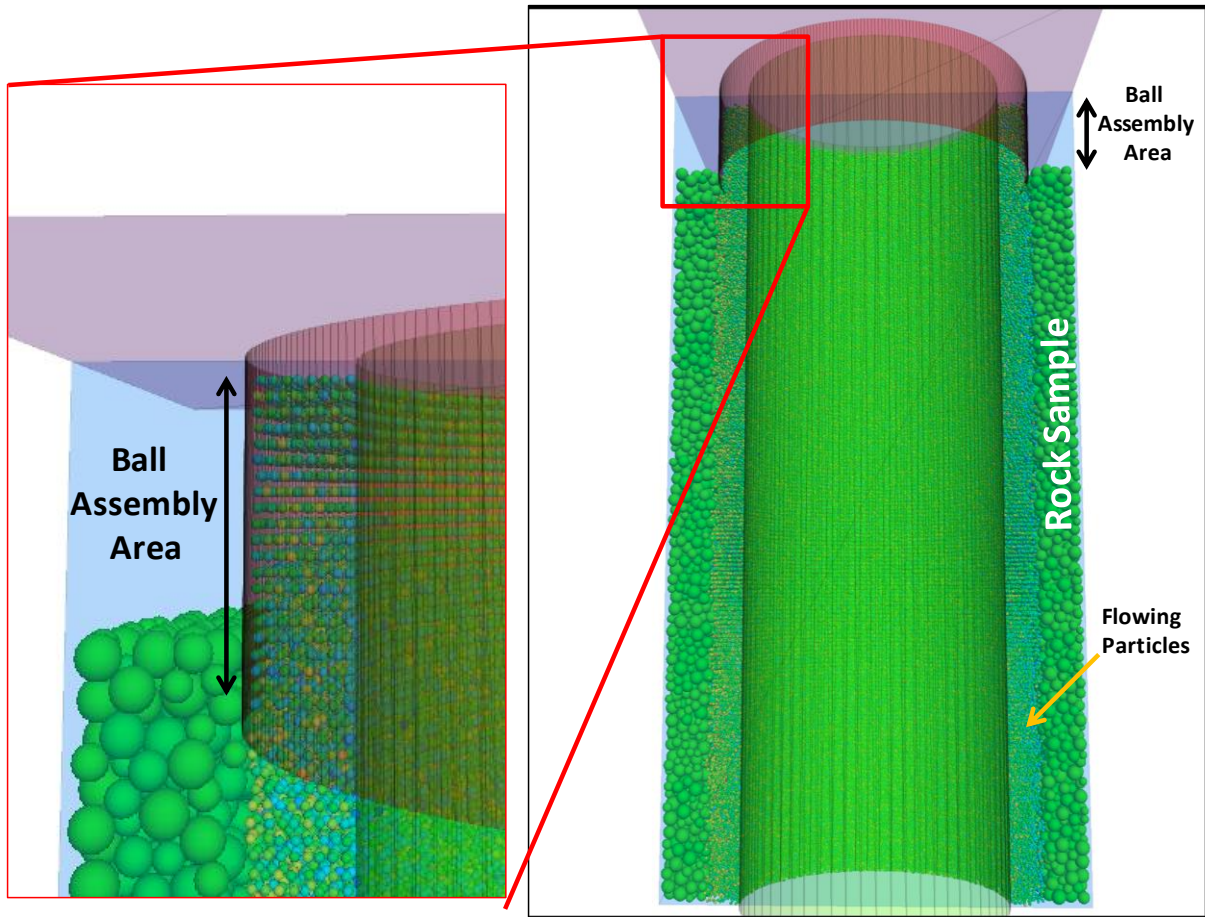


Figure 6-14 Model set up for simulation of erosion in a borehole

The model was run for several hours and the number of detached (eroded) particles was monitored. These are marked with a blue colour in Figure 6-15. The main limitation in modelling of this application was the software run time, which required more than 10 hours for simulating a small fraction of a second. To compare with the experimental observations, the numerical results extrapolated to estimate the erosion rate at 15 minutes, which is likely to introduce large errors.

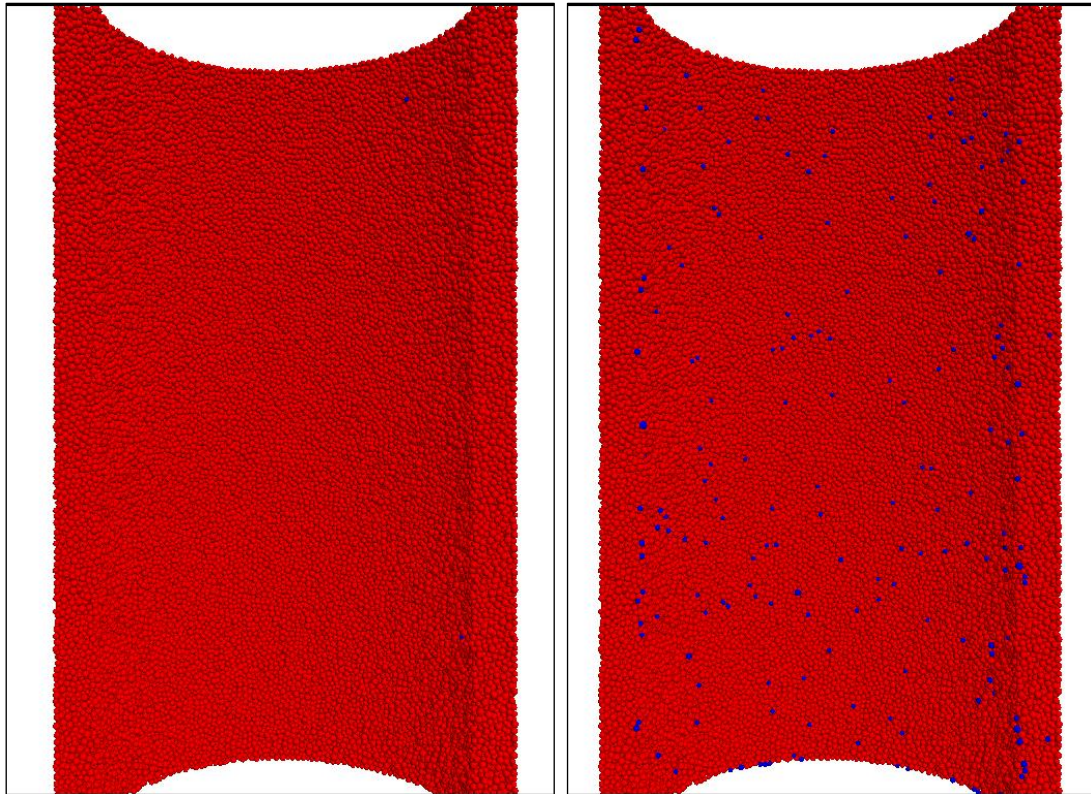


Figure 6-15 Left: Intact rock sample; Right: Eroded rock sample. Blue grains were detached from the sample as a result of the fluid particle interaction

The extrapolated model outcome, as shown in Table 6-5, was very promising and comparable to the laboratory experiments.

Table 6-5 Numerical results for erosion modelling

Simulated time	0.03 seconds
Eroded mass (equivalent of full 400mm cylinder)	0.00326 gr
Erosion rate	0.109 gr/s = 6.52 gr/min
Erosion in 15 minutes	6.5*15 =97.8 gr
Experimental erosion in 15 minutes	50 gr

The results could have been improved if more information was available from the synthetic sample in the calibration process. The fluid phase tuning could also be performed in more detail to cover other apparent rheological properties. The calibration process, for both the rock and fluid phases, is critical because a non-calibrated model can generate unpredicted results. An example is shown in Figure 6-16, where a combination of high particle density and velocity has completely eroded the rock sample.

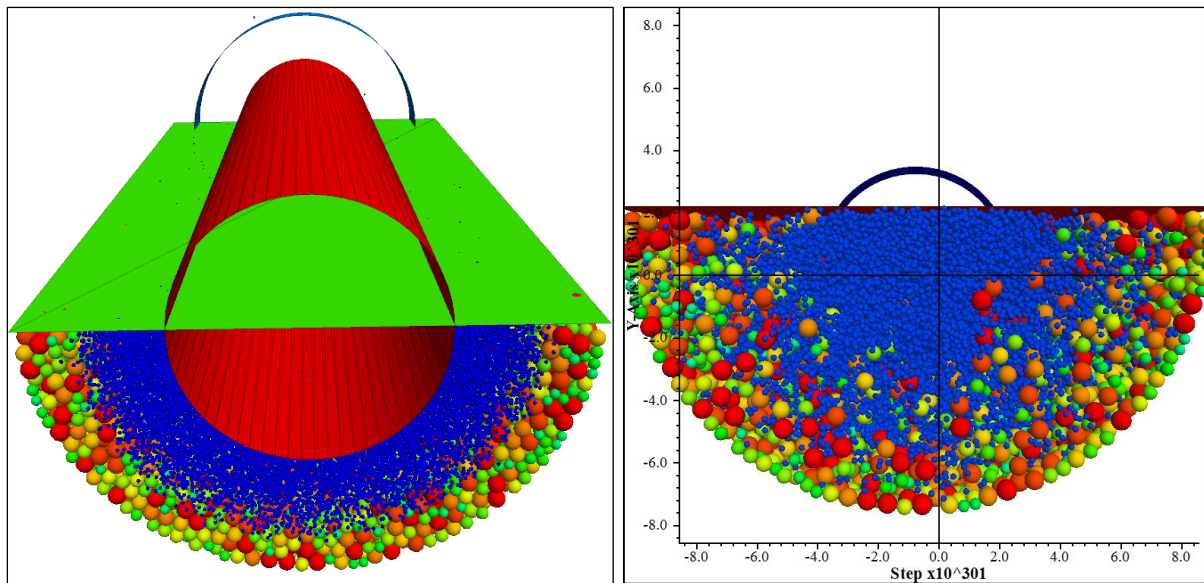


Figure 6-16 An extreme case, where the mass and velocity of the fluid particles were set too high. Left: model at initial state. Right: Rock grains eroded. Notice the eroded and lifted grains inside the fluid particles.

6.3) Chapter Conclusions

Two more applications were presented. TWC more static, Erosion more dynamic compared to the RST.

In both cases acceptable results obtained by simple model. Regretfully due to the lack of information from these experiments, it was not possible to refine the numerical simulations.

This chapter confirmed the conclusions of Chapter 5. DEM is capable of modelling geomechanical applications, however the main restriction is the severe computational expenses.

7 Conclusion and Recommendations

This study was initiated to demonstrate the application of the three-dimensional Discrete Element Method (3D DEM) in geomechanics. The literature review identified a near-exponential increase in the popularity, however several aspects of the method were identified as limiting, the most important of which was the simulation time. Throughout the research, practical methods were proposed to increase the efficiency and reduce the computer run time. Three example applications, with different kinematic settings, were simulated by 3D DEM, which demonstrated the method's capability and limitations. A specific focus was given to the calibration process, where a new method was proposed by refining the existing procedures. All the identified recommendations from the literature were utilised, and in most cases improved, to optimise sample generation, testing and calibration processes. Rock Scratch Testing (RST) was modelled in detail and rigorous sensitivity analyses were performed to study the effect of numerous rock and cutter properties. The literature review identified the most important shortfall of the RST simulations as the velocity dependency, while there were very limited references to it. A review of the extensive RST simulations performed in this research, using different combinations of parameters on diverse types of numerical samples, confirmed the velocity dependency and questioned the conclusion of most of the available literature. Practical methods have been proposed for increasing the efficiency of RST modelling. Furthermore, a method has been proposed to replace the time and resource demanding UCS simulation by a more efficient RST model. Thick-Walled Cylinder and Erosion modelling further proved the application of DEM in geomechanics, where simple models generated acceptable results. I have proposed a novel method to model the fluid phase as discrete particles to simulate the erosion of unconsolidated sands exposed to fluid flow. The following are the conclusions and recommendations based on this research.

7.1) Research Outcomes and Findings

- The sample generation procedure proposed and used in this study provides an integrated approach for building the numerical samples:
 - Sample particles were generated by honouring the Particle Size Distribution curve of the physical sample. The finest 5% of the particles were excluded as they increased the number of balls and reduced the critical time-step, both of which contributed to an increase in the simulation time.
 - Pre-existing cracks and the inhomogeneity of the contact strengths were tuned qualitatively from the microscopic images.

- Changing the particle sizes affects the sample's properties, however pre-calibrating the sample with a very coarse model, running in only a few minutes, significantly reduces the number of trials and errors.
- The test simulation methods and the property measurement are critical in sample calibration, as a poorly designed test can lead to erroneous results, affecting the calibration parameters. For this reason, I have proposed a new method for conducting the confined tests, including TWC modelling, where a layer of external balls was generated around the sample to apply the confining pressure. In contrast to using the rigid walls, the proposed method enables natural rock deformation, while avoiding local stress concentration.
- Where no changes in body mass, velocity or acceleration of particles is anticipated, the time-step calculation stage can be executed for the first few hundred steps, and the stable time-step value can be fixed for future steps, disabling the time-step calculation algorithm. This can speed up the simulation by 30%.
- The proposed calibration procedure for selecting the micro-properties was based on the available methods in the literature, with new steps and parameters added to increase the practicality and calibration quality.
- Extensive sensitivity analyses were conducted to identify the effect of the geometric settings of the Flat-Joint Model. Using a higher number of elements increased the sample brittleness.
- Selection of the contact model is a critical step in building the numerical sample. As a general rule, the models that better represent the sample particles and contacts tend to yield better results in final modelling. Of the different sample types prepared for RST modelling, only the samples built by FJM contacts generated acceptable results. FJM is known to approximate the behaviour of faced grains and is capable of transmitting rotational momentum, that occurs in natural rocks due to the grain shape and interlocking.
- The literature review revealed that almost all of the available literature for RST modelling suffers from a lack of proper sample calibration. Most importantly, they use simple models generated by the Parallel-Bond Model, which is known to over-estimate the UCS/Tensile ratio. This is identified as one of the possible reasons for the poor match of their simulations to the expected cutting force (or ISE) trend.
- Comprehensive sensitivity analyses were performed on the scale effect, both in sample generation and RST modelling. While it was shown that the normalised results of coarse models approximate those of the fine models, to isolate the scale effect and compare the model parameters to those in the literature and laboratory experiments, all the final runs were carried out without any coarsening. This significantly increased the simulation time, but deemed a necessary step to focus on DEM's capabilities and limitations.

- A complete set of Validation Criteria were established from the published RST experiments to cover both the ductile and brittle cutting modes:
 1. ISE/UCS ratio in the ductile region should be close to unity.
 2. A critical depth of cut should exist at approximately 1mm depth of cut, where a change of cutting mode occurs.
 3. The cutting mechanism in the ductile mode should be dominated by extensive crushing in front of the cutter, while in the brittle mode chipping should occur.
- Contrary to the general claim in the literature that the RST modelling results with DEM can be validated, it was shown that where the claim is made, the cutting velocity was in the 2-5m/s range. This is several orders of magnitude larger than the typical experimental range (a few mm/s).
- The rigorous sensitivity analyses on cutting speed showed that DEM results of RST modelling can only be conditionally validated. This was because of speed dependency of the cutting force, which means the model can only meet the first validation criterion in the 2-5m/s interval.
- The final calibrated sample produced acceptable results, matching the second and third validation criteria, i.e. change of cutting mode and failure type in front of the cutter. The first criteria (ISE = UCS) was also conditionally matched by finding the required cutting speed. I proposed a systematic method to find the cutting speed by normalising the results of a coarse model. In all the cases, the required cutting speed to generate ISE=UCS was much greater than the experimentally used values.
- By RST modelling on several differently-calibrated samples (2D samples, IINT3D A1, A2 and B1; FNL A, B, C and D) and comparing the results, I concluded that the interaction of the detached particles in the crushed zone is a critical factor in determining the cutting response. In fact, it is likely that it determines whether the model matches the validation criteria 2 and 3, while other micro-properties determine the magnitude of ISE/UCS at a specific cutting speed.
- Practical methods proposed to replace a UCS simulation by an RST model, where all the compressive test results (UCS, E and ν) are obtained in a single scratch test. This can reduce the simulation time by one order of magnitude.
- The proposed confined test method was used for TWC modelling, where the experimental trend was obtained by using a simple model and basic calibration.
- A novel method was proposed for modelling the fluid phase with fine discrete particles and a systematic approach was developed for tuning the apparent rheological properties. The model generated very encouraging results.
- The above conclusions demonstrate the capabilities and limitations of 3D DEM in geomechanical applications. While in some cases acceptable results were obtained by simple models (e.g. UCS test simulation and Erosion Modelling), others (e.g. Confined test simulation,

TWC and RST modelling) required further refinement. Some inconsistencies were also demonstrated between the experimental observations and the numerical results of this research, the most important of which are the cutting's speed dependency and a very low ISE/UCS ratio at typical experimental cutting speeds (few millimetres per second).

- The simulation time remains the most important limiting aspect of the 3D DEM, which forces the use of a smaller sample, simulation over a shorter time period followed by extrapolation to the required time length, a coarser sample or a combination of all.
- 3D DEM modelling is a valuable tool to study geomechanical applications at grain scale, however similar to any other modelling method, it is prone to errors if unsuitable assumptions are used for sample calibration or the final application modelling.

7.2) Recommendations

- The numerical samples of this study were built using spherical (balls) and non-spherical (clumps) particles. FJM was used in the case of spherical particles to emulate grain interlocking and enable moment transfer. It would be of interest to study the effect of grain shape on sample behaviour and cutting response by using different clump types.
- The cutting parameters which were studied here were limited to Back Rake Angle, Cutting Speed, Cutter Width and Depth of Cut. Other parameters such as Side Rake Angle, Cutter Shape and Cutter Bluntness are recommended to be included in the modelling.
- Investigation of the cutting response was mainly limited to the study of the vertical and horizontal cutting forces and cutting mode. Crack propagation was studied qualitatively by observing the level of crushing or chipping in front of the cutter. It is recommended to investigate the crack generation and propagation quantitatively by tracking their number in different zones below the cutter.
- Due to the lack of information from the mechanical properties of the samples used in TWC and Erosion, it was not possible to fine tune the micro-properties. Further research can be conducted by carrying out the laboratory tests on samples with known properties. This will reduce the numerical modelling uncertainties and is likely to improve the match quality between the experimental and numerical results.
- The Erosion simulation presented in Chapter 6, provides a new approach for fluid modelling. The apparent rheological properties were calibrated by matching the expected drag of a laminar flow on flat and spherical surfaces. An expansion of the calibration process to include the turbulent flow regime is recommended.

- Extending the simulation time for the erosion modelling will reduce the uncertainties related to extrapolating the results to compare with the laboratory data. This is recommended for future research.

References

1. Al-Yaseri, A. Z., M. Lebedev, S.J. Vogt, M. L. Johns, A. Barifcani and S. Iglauer. 2015. "Pore-scale analysis of formation damage in Bentheimer sandstone with in-situ NMR and micro-computed tomography experiments." *J. of Petroleum Science and Engineering*. 129: 48-57.
2. Massoud Bayati, Personal communication
3. Borba, A. M., F. H. Ferreira, E. S. R. Santos, V. M. D. Menezes and M. Strugale. 2014. "UCS Estimation through Uniaxial Compressive Test, Scratch Test and Based Log Empirical Correlation." Paper presented at *ISRM Conference on Rock Mechanics for Natural Resources and Infrastructure*, Goiania, Brazil, 9-13 September 2014.
4. Castro-Filgueira, U., L.r. Alejano, J. Arzúa, and D. Mas Ivars. 2017. "Sensitivity Analysis of the Micro-Parameters Used in a PFC Analysis Towards the Mechanical Properties of Rocks." *Procedia Engineering* 191: 488-95.
5. Castro-Filgueira, U., L. Alejano, J. Arzúa, and D. Mas. 2016. "Numerical Simulation of the Stress-strain Behavior of Intact Granite Specimens with Particle Flow Code." *Rock Mechanics and Rock Engineering: From the Past to the Future*, 2016.
6. Chang, Ching S., and Anil Misra. 1990. "Packing Structure and Mechanical Properties of Granulates." *Journal of Engineering Mechanics* 116(5): 1077-093
7. Cundall, P. A., & Strack, O. D. L. 1979. "A discrete numerical model for granular assemblies." *Geotechnique*, 29(1): 47-65.
8. Cundall PA. 1971. "A computer model for simulating progressive large scale movements in blocky rock systems." *In: Proceedings of the Symposium of the International Society of Rock Mechanics*, Nancy, France, 1971.
9. Cundall, P. A. 1987. "Distinct Element Models of Rock and Soil Structure." *Analytical and Computational Methods in Engineering Rock Mechanics*, Chapter 4, pp. 129-163.
10. Detournay, E., Drescher, A., and Hultman, D.A., 1997. "Portable rock strength evaluation device." United States Patent 5670711.
11. Ding, X. 2013. "Development Of A Rock Expert System (Res) For Evaluating Rock Property Values And Utilization Of Three Dimensional Particle Flow Code (PFC3D) To Investigate Rock Behavior." PhD diss, The University Of Arizona.

12. EVANS, I. A. 1962. "Theory of the Basic Mechanics of Coal Ploughing", *Proceedings of the International Symposium on Mining Research 2*: 761-798, Pergamon Press, Oxford.
13. Folkerts, M. et al., 2018, Britannica Encyclopaedia; Online version, <https://www.britannica.com/science/mathematics>
14. Fakhimi, A., Villegas, T. 2007. "Application of Dimensional Analysis in Calibration of a Discrete Element Model for Rock Deformation and Fracture." *Rock Mechanics and Rock Engineering*, 40(2):193-211.
15. Glowka, D. 1989. "Use of Single-Cutter Data in the Analysis of PDC Bit Designs: Part 1 - Development of a PDC Cutting Force Model." *Journal of Petroleum Technology*, 41(08):797-849.
16. He, X., Xu, C., Peng, K. et al. 2017. "Simultaneous Identification of Rock Strength and Fracture Properties Via Scratch Test." *Rock Mech Rock Eng*, 50: 2227.
17. R.L.J. Helmons, S.A. Miedema, M. Alvarez Grima, C. van Rhee. 2016. "Modeling fluid pressure effects when cutting saturated rock", *Engineering Geology*, 211:50-60.
18. Huang, H.Y. 1999. "Discrete element modeling of tool-rock interaction", PhD diss, University of Minnesota, Minneapolis, MN.
19. ITASCA. 2017. "details-and-system-requirements." <http://www.itascacg.com/pfc2d/overview.php>
20. ITASCA. 2017. PFC3D Manual.
21. Jing L., J.A. Hudson. 2002. "Numerical methods in rock mechanics." *International Journal of Rock Mechanics and Mining Sciences* 39(4):409-427.
22. Jonak J, Podgoński J. 2001. "Mathematical model and results of rock cutting modelling." *Journal of Mining Science* 37: 615–8.
23. Joodi, B., M. Sarmadivaleh, V. Rasouli & A. Nabipour. 2012. "Simulation Of The Cutting Action Of A Single PDC Cutter Using DEM". *WIT Transactions on Engineering Sciences* 81:143-150.
24. Joodi, B. 2016. "Using Scratch Tests for Rock Strength Determination in Discrete Element Method." Paper presented at *50th U.S. Rock Mechanics/Geomechanics Symposium*, Houston, USA, 26-29 June 2016.

25. Khan, M. 2010. "Investigation of Discontinuous Deformation Analysis for Application in Jointed Rock Masses." Ph.D diss, University of Toronto.
26. Klein, E., P. Baud, T. Reuschlé, T-f. Wong. 2001. "Mechanical behaviour and failure mode of bentheim sandstone under triaxial compression." *Physics and Chemistry of the Earth, Part A: Solid Earth and Geodesy* 26(1–2): 21-25.
27. Korinets AR, Alehossein H, Chen L, Lim W, Baker G. DIANA. 1996. "Modeling of a rolling disc cutter and rock indentation." *Rock Mechanics, Tools and Techniques* 1996:647–654.
28. Kou SQ, Lindqvist PA, Tang CA, Xu XH. 1999. "Numerical simulation of the cutting of inhomogeneous rocks." *International Journal of Rock Mechanics and Mining Sciences* 36:711–7.
29. Koyama T, Jing L. 2007. "Effects of model scale and particle size on micro-mechanical properties and failure processes of rocks – A particle mechanics approach." *Eng Anal Boundary Elem* 31(5):458-472.
30. Lazzari E. 2013. "Analysis of shear strength of rock joints with PFC2D." Master's Thesis, KTH Royal Institute of Technology.
31. Manne A. and N. Satyam. 2015. "A Review on the Discrete Element Modeling of Dynamic Laboratory Tests for Liquefaction Assessment." *Electronic Journal of Geotechnical Engineering* 20: 21-46.
32. Mathieu, J., & Scott, J. 2000. "An Introduction to Turbulent Flow." Cambridge: Cambridge University Press.
33. Mendoza, J.A., Gamwo, I.K., Zhang, W. and Lin, J.-S. 2011. "Considerations for Discrete Modeling of Rock Cutting." Paper presented at *45th US Rock Mechanics / Geomechanics Symposium*, San Francisco, California, 2011.
34. Naeimipour, A., J. Rostami, E. Keller, O.Frough and S. Wang. 2015. "Estimation of Rock Strength by Means of Scratch Probe." Paper presented at *49th US Rock Mechanics / Geomechanics Symposium*, San Francisco, CA, USA, 2015.
35. Nishimatsu Y. 1972. "The mechanics of rock cutting." *International Journal of Rock Mechanics and Mining Sciences & Geomechanics Abstracts*, 9(2):261-270.
36. O'Sullivan, C. 2014. "Advancing Geomechanics using DEM." *Geomechanics from Micro to Macro Proceedings of IS-Cambridge*, Vol. 1.

37. O’Sullivan, C. 2011. *Particulate Discrete Element Modelling, A Geomechanics Perspective*, London: CRC Press.
38. O’Sullivan, C., Bray J. 2003. “Selecting a suitable time-step for discrete element simulations that use the central difference time integration scheme.” *Engineering Computations* 21:2-4.
39. O’Sullivan C. 2014. “Advancing geomechanics using DEM”, keynote talks, IS-Cambridge. Cambridge, UK. 1-3 September 2014.
40. Peksa Anna E., Karl-Heinz A.A. Wolf, Pacelli L.J. Zitha, “Bentheimer sandstone revisited for experimental purposes.” *Marine and Petroleum Geology* 67:701-719.
41. Potyondy D. 2016. Memorandum, Material modeling support in PFC Documentation.
42. Potyondy, D.O. and Cundall, P.A. 2004. “A Bonded-Particle Model for Rock.” *International Journal of Rock Mechanics & Mining Sciences* 41:1329-1364
43. Potyondy D. 2014. “The bonded-particle model as a tool for rock mechanics research and application: current trends and future directions.” PFC Documentation.
44. Potyondy D. 2015. “Material-Modeling Support in PFC via PFC 5.0 FISHTank (fistPkg).” PFC Documentation.
45. Reyer, D. and S.L. Philipp. 2014. “Empirical relations of rock properties of outcrop and core samples from the Northwest German Basin for geothermal drilling.” *J. Geothermal Energy Science* 2: 21-37.
46. Richard, T., F. Dagrain, E. Poyol, and E. Detournay. 2012. “Rock strength determination from scratch tests.” *J. Engineering Geology* 147-148: 91-100.
47. Richard, T., E. Detournay, A. Drescher, P. Nicodeme, and D. Fourmaintraux. 1998. “The Scratch Test As A Means To Measure Strength of Sedimentary Rocks.” Paper presented at *SPE/ISRM Rock Mechanics in Petroleum Engineering*, Trondheim, Norway, 8-10 July 1998.
48. Rizo, J. A. M. 2013. “Considerations for Discrete Element Modeling Of Rock Cutting” PhD diss, University of Pittsburgh.
49. Rojek, J. and O’neate, E. 2008. “Coupled discrete/finite element modelling of geotechnical problems.” Paper presented at *8th. World Congress on Computational Mechanics*, Venice, Italy, 2008.

50. Rojek J., E. Oñate, C. Labra, and H. Kargl. 2011. "Discrete element simulation of rock cutting." *International Journal of Rock Mechanics & Mining Sciences* 48: 996–1010.
51. Sallam, A.M., A.K. Ashmawy, and B.D. Runkles. 2004. "Experimental validation of modelling irregular particle shapes using DEM." *In Proceedings of the Second International PFC Symposium*, Kyoto, Japan, 363-372.
52. Schei, G., Fjær, E., Detournay, E., Kenter, C. J., Fuh, G. F., & Zausa, F. 2000. "The Scratch Test: An Attractive Technique for Determining Strength and Elastic Properties of Sedimentary Rocks." Paper presented at *SPE Annual Technical Conference and Exhibition*, Dallas, USA, 1-4 October 2000.
53. Starfield A.M., P.A. Cundall. 1988. "Towards a methodology for rock mechanics modelling." *International Journal of Rock Mechanics and Mining Sciences & Geomechanics* 25(3): 99-106.
54. Strack, O. D. L., and P. A. Cundall. 1978. *The distinct element method as a tool for research in granular media*. Minneapolis. Minnesota: University of Minnesota.
55. Su O., Nuri Ali Akcin. 2011. "Numerical simulation of rock cutting using the discrete element method." *International Journal of Rock Mechanics and Mining Sciences* 48(3):434-442.
56. Tehrani, S., Joodi, B., Nourifard, N., Sarmadivaleh, M. and Younessi, A. 2017. "Experimental and numerical investigation of the effect of inner and outer boundary dimensions on collapse of the sample in thick-walled cylinder test." Paper presented at *51st U.S. Rock Mechanics/Geomechanics Symposium*, San Francisco, USA 25-28 June 2017.
57. Traska M. 2014. "Water transport properties in building materials: traditional methods versus CT-based pore network analysis." Master's thesis, Gent University.
58. Tulu, I. B. and Heasley, K. A. 2009. "Calibration of 3D Cutter-Rock Model with Single Cutter Tests." Paper presented at *The 43rd US Rock Mechanics Symposium and 4th U.S.-Canada Rock Mechanics Symposium*, Asheville, USA. 28 June - 1 July 2009.
59. Vallejos Javier A., Kimie Suzuki, Andrés Brzovic, Diego Mas Ivars. 2016. "Application of Synthetic Rock Mass modeling to veined core-size samples." *International Journal of Rock Mechanics & Mining Sciences* 81:47-61.
60. Veeken, C., et al., 1991. "Sand production prediction review: developing an integrated approach." Paper presented at *SPE Annual Technical Conference and Exhibition*, Dallas, USA, 6-9 October 1991.

61. Wang Yuannian, Fulvio Tonon. 2009. "Modeling Lac du Bonnet granite using a discrete element model." *International Journal of Rock Mechanics and Mining Sciences* 46(7):1124-1135.
62. Wang, Yuannian, Tonon, Fulvio. 2010. "Calibration of a discrete element model for intact rock up to its peak strength" *International Journal for Numerical and Analytical Methods in Geomechanics* 34(5):447-469.
63. Wu S., X. Xu. 2016. "A Study of Three Intrinsic Problems of the Classic Discrete Element Method Using Flat-Joint Model" *Rock Mech. & Rock Eng* 49:1813–1830.
64. Wyk G. van, D.N.J. Els, G. Akdogan, S.M. Bradshaw, N. Sacks. 2014. "Discrete element simulation of tribological interactions in rock cutting." *International Journal of Rock Mechanics and Mining Sciences* 65:8-19.
65. Yang, B.D. and Lei, S. 2004. "Distinct element simulation of conventional and laser assisted machining of silicon nitride ceramics: material removal mechanism." *International Journal of Manufacturing Research* 4(1):74-94.
66. Yang B.D., Yue Jiao and Shuting Lei. 2006. "A study on the effects of microparameters on macroproperties for specimens created by bonded particles." *Engineering Computations* 23(6):607-631.
67. Zhu, H., Z. Zhou, R. Yang, & A. Yu. 2007. "Discrete particle simulation of particulate systems: Theoretical developments." *Chemical Engineering Science* 62(13): 3378–3396.

Every reasonable effort has been made to acknowledge the owners of copyright material. I would be pleased to hear from any copyright owner who has been omitted or incorrectly acknowledged.

Appendix-1

Table A-1 Micro-properties of the 2D Exploratory model (Joodi et. al., 2012)

Property	Value	Property	Value
Sample size (cm)	12×6	Contact Young's modulus (GPa)	12.1
Particle density (kg/m ³)	2050	Particle stiffness ratio	3.08
Minimum particle radius (mm)	0.2	Particle friction coefficient	0.5
Particle size ratio	1.66	Parallel bond normal strength (MPa)	51.9
Number of particles	30,000	Parallel bond cohesion (MPa)	32.0
Parallel bond friction angle (Degree)	35.0		

Table A-2 Micro-properties of sample FNL3D-A

Linear Group	emod (e9)	15	Results	UCS (MPa)	39.3
	krat	2.5		E (GPa)	15
	fric	0.5		v	0.211
emod	15	C (MPa)		8.58	
krat	2.5	φ (°)		42.81	
fj_ten	2.08	Tensile (MPa)		2.34	
fj_coh	24.1	UCS/T		16.8	
fj_fa	0				
FJ_Fric	0.1				
dp_nratio	0.7				
FJM Group	Bonded Frac	1			
	Gapped Frac	0			
	FJM_Nr	1			
	FJM_Nal	3			
	Gap	0.035*CF			

Table A-3 Micro-properties of sample FNL3D-B

Linear Group	emod (e9)	15.7	Results	UCS (MPa)	40.62
	krat	2.5		E (GPa)	13.97
	fric	0.5		v	0.235
FJM Group	emod	15.7		C (MPa)	8.72
	krat	2.5		φ (°)	40.9
	fj_ten	2.97		Tensile (MPa)	2.24
	fj_coh	34.46		UCS/T	18.1
	fj_fa	0			
	FJ_Fric	0.1			
	dp_nratio	0.7			
	Bonded Frac	0.8			
	Gapped Frac	0			
	FJM_Nr	1			
	FJM_Nal	3			
Gap	0.035*CF				

Table A-4 Micro-properties of sample FNL3D-C

Linear Group	emod (e9)	15.7	Results	UCS (MPa)	36
	krat	2.5		E (GPa)	15.9
	fric	0.5		v	0.21
FJM Group	emod	15.7		C (MPa)	8.72
	krat	2.5		φ (°)	40.9
	fj_ten	2.97- +20%		Tensile (MPa)	2.178
	fj_coh	34.46- +20%		UCS/T	16.5
	fj_fa	0			
	FJ_Fric	0.1			
	dp_nratio	0.7			
	Bonded Frac	0.8			
	Gapped Frac	0			
	FJM_Nr	1			
	FJM_Nal	3			
Gap	0.035*CF				

Table A-5 Micro-properties of sample FNL3D-D

Default FJM Group	emod (e9)	15	Results	UCS (MPa)	38.1
	krat	2.1		E (GPa)	17.4
	fric	0.2		ν	0.175
FJM Group	emod	15		C (MPa)	9.30
	krat	2.1		ϕ (°)	42.1
	fj_ten	3-+20%		Tensile (MPa)	2.105
	fj_coh	20-+20%		UCS/T	18.1
	fj_fa	0			
	FJ_Fric	0.2			
	dp_nratio	0.7			
	Bonded Frac	0.8			
	Gapped Frac	0			
	FJM_Nr	5			
FJM_Nal	10				
Gap	0.035*CF				

Table A-6 Micro-properties of the fluid phase in Erosion Modelling

emod	3.2e9
kratio	3.5
dp_nratio	0
fric	0.1
Tangential Velocity	Q / A
LatToTanVel	-2 to +2

Permissions and Co-author Attribution Statements

PERMISSION TO USE COPYRIGHT MATERIAL AS SPECIFIED BELOW:

Simulation Results published in papers ARMA 16-0624 and ARMA 17-274

I hereby give permission for **Bahman Joodi** to include the abovementioned material(s) in his/her higher degree thesis for Curtin University, and to communicate this material via the espace institutional repository. This permission is granted on a non-exclusive basis and for an indefinite period.

I confirm that I am the copyright owner of the specified material.

Signed:

Name: Peter Smeallie

Position: Executive Director

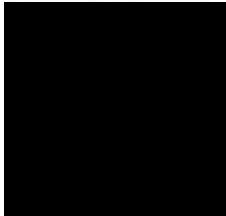
Date: 6 December 2018

Please return signed form to


Bahman Joodi

Bahman.Joodi@PostGrad.Curtin.edu.au


Paper "Simulation Of The Cutting Action Of A Single PDC Cutter Using DEM". WIT Transactions on Engineering Sciences 81:143-150.

	Conception and Design	Acquisition of data & method	Data condition & manipulation	Analyses & statistical method	Interpretation & discussion	Final approval
Dr Vamegh Rasouli					X	X
I acknowledge that these represent my contribution to the above research output Signed: 						


Paper "Simulation Of The Cutting Action Of A Single PDC Cutter Using DEM". WIT Transactions on Engineering Sciences 81:143-150.

	Conception and Design	Acquisition of data & method	Data condition & manipulation	Analyses & statistical method	Interpretation & discussion	Final approval
Dr Mohammad Sarmadivaleh			X		X	X
I acknowledge that these represent my contribution to the above research output Signed:  Digitally signed by Mohammad Sarmadivaleh Date: 2020.11.25 13:40:44 +08'00'						

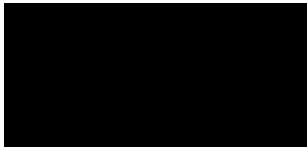
Paper "Simulation Of The Cutting Action Of A Single PDC Cutter Using DEM". WIT Transactions on Engineering Sciences 81:143-150.

	Conception and Design	Acquisition of data & method	Data condition & manipulation	Analyses & statistical method	Interpretation & discussion	Final approval
Dr Amin Nabipour			X		X	
I acknowledge that these represent my contribution to the above research output Signed:  25, 11, 2020						


Paper “Experimental and numerical investigation of the effect of inner and outer boundary dimensions on collapse of the sample in thick-walled cylinder test.” Paper presented at 51st U.S. Rock Mechanics/Geomechanics Symposium, San Francisco, USA 25-28 June 2017.

	Conception and Design	Acquisition of data & method	Data condition & manipulation	Analyses & statistical method	Interpretation & discussion	Final approval
Soroush Tehrani	X	X	X	X	X	X
I acknowledge that these represent my contribution to the above research output Signed:  25/11/2020						

Paper “Experimental and numerical investigation of the effect of inner and outer boundary dimensions on collapse of the sample in thick-walled cylinder test.” Paper presented at 51st U.S. Rock Mechanics/Geomechanics Symposium, San Francisco, USA 25-28 June 2017.

	Conception and Design	Acquisition of data & method	Data condition & manipulation	Analyses & statistical method	Interpretation & discussion	Final approval
Nourifard, N.			X		X	X
I acknowledge that these represent my contribution to the above research output Signed: 						

Paper “Experimental and numerical investigation of the effect of inner and outer boundary dimensions on collapse of the sample in thick-walled cylinder test.” Paper presented at 51st U.S. Rock Mechanics/Geomechanics Symposium, San Francisco, USA 25-28 June 2017.

	Conception and Design	Acquisition of data & method	Data condition & manipulation	Analyses & statistical method	Interpretation & discussion	Final approval
Dr Mohammad Sarmadivaleh			X		X	X
I acknowledge that these represent my contribution to the above research output Signed:  Digitally signed by Mohammad Sarmadivaleh Date: 2020.11.25 13:41:03 +0800						